Toughness Enhancement of High Strength Low Alloy Strip Steels

By

Rachel Bridget Punch

A thesis
submitted to The University of Birmingham
for the degree of DOCTOR OF PHILOSOPHY

School of Metallurgy and Materials
College of Engineering and Physical Sciences
University of Birmingham
September 2013

Abstract

High strength strip steels with a yield strength of ~700 MPa are used in the yellow goods industry, with recent trends requiring thicker strips with an improved toughness. Strip steel was produced to thicknesses of 10 – 17 mm, with thinner strips showing improved Charpy impact toughness compared to the thicker strip. It was found that all samples (different thicknesses and test orientations) showed splits on the fracture surfaces in the upper transition region.

The hot rolled strip steels showed a predominantly fine-grained (~4 µm ECD) ferrite microstructure, with some coarse grain patches (grains ≥5 µm grouped together). No significant differences were noted for the grain size, yield stress, tensile strength, hardness and texture for the different compositions. Splits were characterised and produced successfully by low blow Charpy testing with acoustic emission (AE) sensors indicating the presence of splits which occurred in the upper transition region predominantly without main crack propagation. Analysis by x-ray tomography and sectioning was carried out showing splits propagate by transgranular cleavage, preferentially following coarse-grained regions, with the 10 mm strip producing deeper splits which was related to elongated grains (high aspect ratio).

Therefore the presence of deep splits improved toughness through a reduction of the impact transition temperature, which was achieved by ensuring the presence of a bimodal grain structure, containing coarse elongated grain patches.

Publications

- R. Punch, M.Strangwood and C.L Davis, “Split formation during low blow Charpy testing of high strength strip steels”, Metallurgical and Materials Transactions A, December 2012, Volume 43, Issue 12, pp 4622-4632

- R. Punch, A.G. Kostryzhev, M.Strangwood and C. L. Davis “The effect of microstructure on the origin and propagation of splits in high strength strip steel” EuroMat, Sept 2011 (Poster)

- R. Punch, A.G. Kostryzhev, M.Strangwood and C. L. Davis “Investigation into the initiation and propagation of splits in high strength strip steel” ATCOM 2011, Ranchi, India, July 5-7th, 2011

- A.G. Kostryzhev, R. B. Punch, C. L. Davis, and M. Strangwood Acoustic emission monitoring of split formation during Charpy impact testing of high strength steel, Material Science and Technology, 2012,(2), 28,pp 240-242

Acknowledgements

There are many people to who I owe a lot for their help during my time as a PhD student. Firstly I need to thank my supervisors Professor Claire Davis and Dr Martin Strangwood, for their constant support and encouragement. I have learnt a great deal from both of them and could not have asked for better supervisors. Thank you to my industry supervisor, Dr Dave Crowther from Tata Steel, for his support and advice throughout the project, along with the Materials and Metallurgy department, in particular Dr Carl Slater, who was always on hand to discuss latest test results or just grab a morning coffee.

I could not have carried out this project if it wasn't for the financial support of the Engineering and Physical Sciences Research Council (EPSERC) and Tata Steel. Thank you for giving me the opportunity.

Finally, and most importantly to my family. To my parents, for always supporting my decisions, and being there for me. To my family and friends for the fun times and words of encouragement, and last but not least to Simon Holland. Thank you for your support, I couldn't have done it without you.

CONTENTS

LIST OF FIGURES

LIST OF TABLES

1. INTRODUCTION

1.1. **High strength low alloy (HSLA) steel strip**

There are a variety of factors that influence the continued development of HSLA steels, such as product cost reduction, reduction in product weight through increases in yield strength (the most dominant factor for HSLA steel) and increase in weldability (1). HSLA steels are produced not only in strip form but also plate, pipe and bar (which can act as reinforcement in concrete structures). HSLA steels are defined by the use of microalloying additions, such as niobium, titanium, vanadium and aluminium, to achieve a high yield stress with less than 0.1 wt % total addition of these alloying elements (2).

The use of steels at low temperatures has increased since the 1960s with, for example, steel pipelines being used in the Arctic for liquid gas transport. HSLA steels were initially developed in the 1940s (see Figure 1.1) and are mainly characterised by their fine grain size and precipitation strengthening effects (3-7). They achieve their high strength, low transition temperatures and high fracture toughness through a fine grain size and small microalloying additions. A small amount of carbon is also present (<0.10 wt%) resulting in a small volume fraction of a carbide phase; instead of coarse cementite particles or lamellae in pearlite, a fine dispersion of alloy carbides are formed (which is also key for weldability of these grades) (8). Substitutional alloying elements are also used to lower the ductile-brittle transition temperature, such as manganese and nickel. A defining point for the production of a fine grain sized product was the introduction of controlled rolling around 1963-1967 (2).

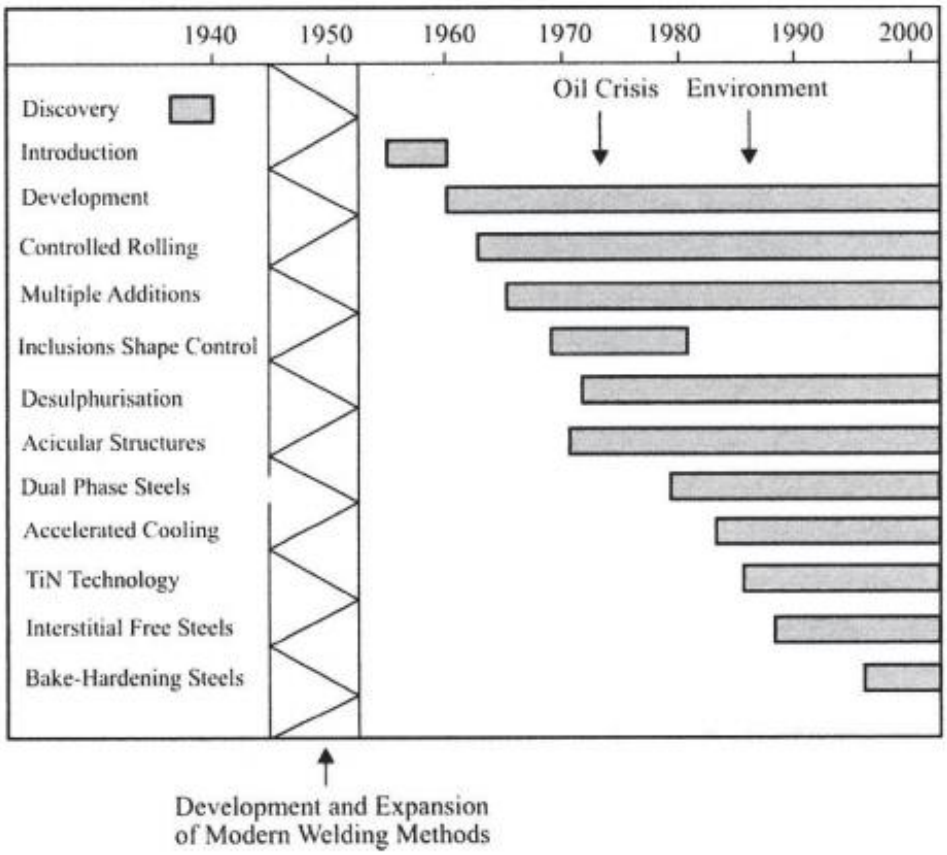

Figure 1.1. Development of HSLA steels (1).

When selecting a material, the important mechanical characteristics must be defined for the particular application, anything from car wheels to masts for wind power generators. The mechanical characteristics are usually yield stress, tensile strength, elongation, low temperature impact toughness, work hardening, fatigue performance and weldability (6). These are achieved by a variety of microstructures with a typical HSLA strip showing a fine grained ferrite grain size with a small amount of second phase and precipitation hardening, see Figure 1.2 for general relationships between yield stress and microstructure.

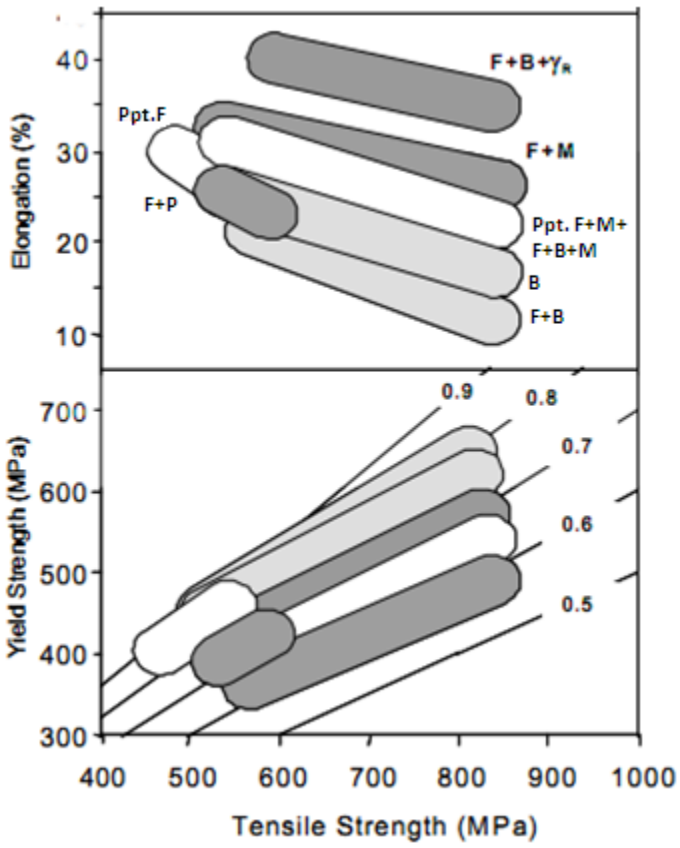

Figure 1.2. The relationships between microstructure and properties for strip steels. F= ferrite, P= pearlite, B= bainite, M= martensite, γ_R= retained austenite and Ppt= precipitates, 0.5- 0.9 indicates YS:TS (9).

1.2. **Processing of HSLA steels**

It is known that micro-segregation of niobium (and other alloying elements) occurs during continuous casting (10). Niobium is the most effective microalloying element in grain refinement in HSLA steels (11), but also partitions between solute-rich and solute-poor regions by micro-segregation with these regions being separated by the secondary dendrite arm spacing (SDAS) (11, 12).

The tendency for an element to segregate depends on its equilibrium partition ratio, 'k_p' value which is the ratio of composition in solid / composition in liquid; example values are given in Table 1.1. Elements with a low k_p value have a high tendency to segregate to the liquid phase. The spacing of the dendrite arms also affects the extent of micro-segregation, especially the secondary dendritic arm spacing (SDAS) (3). The SDAS increases with an increasing distance from the chill surface, due to a decreasing cooling rate, although for the majority of continuous casting processes similar cooling rates are used with little variations in the SDAS from surface to bulk.

Table 1.1. Equilibrium partition ratio for alloying elements in a steel (3, 13-15).

Element	Equilibrium partition ratio, 'k_p'
S	0.02
O	0.02
P	0.13
C	0.13
Nb	0.23
N	0.28
Ti	0.61
Si	0.66
Ni	0.80
Mn	0.84
V	0.90
Al	0.92

The niobium segregation ratio (Nb in dendrite region : interdendritic region) has been predicted (using Thermo-Calc software) in literature reports as 1:10 (16) and 1:7 (12) in similar low carbon niobium steels. When the segregation was measured experimentally by Chakrabarti et al. (10) for cast low carbon niobium steels, it was found that the partition coefficients were 1:3.8 - 1:5. Figure 1.3 (3) contains the predicted partition coefficients for some microalloying elements, which show niobium segregating most strongly (for elements shown), but going through an abrupt change when the solidification phase changes from δ

ferrite to a mixture of δ ferrite and austenite, which indicates a greater solubility of niobium in austenite.

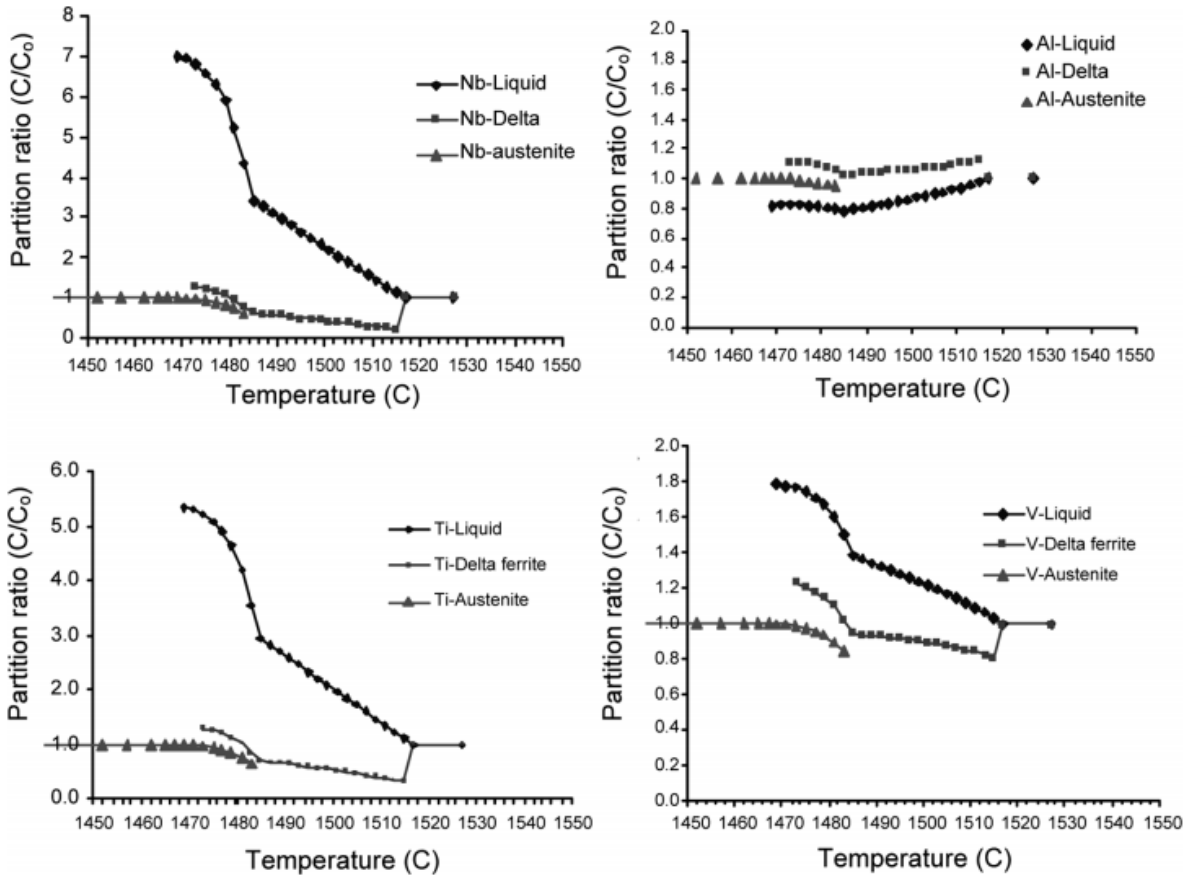

Figure 1.3. Microalloying elements partitioning ratios predicting using Thermo-Calc (3).

1.2.1. **Reheating**

The slabs need to be reheated to a temperature high enough to dissolve any existing precipitates formed during slow cooling after casting, but low enough not to cause excessive grain growth (17). Sufficient time at the reheating temperature is required so that the precipitates dissolve and the microalloying elements are taken into solution ready to precipitate out during/ after the rolling process. During reheating dissolution can be complete or partially complete, depending on overall composition, reheat temperature, time and degree of segregation (amplitude and distance). The austenite grains will grow during reheat as

precipitates which inhibit grain growth dissolve. Figure 1.4 shows the coarsening of austenite grains as a function of reheat temperature for various microalloying additions. The hatched areas seen in Figure 1.4 represent the temperatures at which austenite coarsening starts for the microalloyed steels containing the elements given. At temperatures below this, the pinning force exerted by the particles is large enough to stop grain coarsening. Titanium is a valuable addition to resist austenite grain coarsening due to the high thermal stability of TiN and it is used for grain size control during welding in the heat affected zone (2).

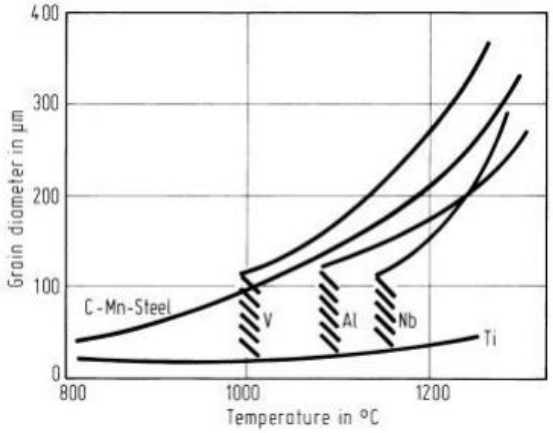

Figure 1.4. Austenite grain growth characteristics in steels containing various microalloying additions (18).

The segregation of niobium and its role in pinning grain boundaries, as Nb(C, N) means that there will be a difference in the pinning potential between the dendritic and interdentritic regions (3,12). Differences in precipitate populations will develop on solidification, but when reheating is carried out at a high enough temperature, complete dissolution of precipitates in both regions can take place. Removing all particle pinning results in a coarse austenite grain size (3). Chakrabarti (3) carried out work on a Nb-containing steel using two different reheating temperatures (Figure 1.5), and showed that with a reheating temperature of 1225 ^{0}C a coarse unimodal austenite grain size is observed with an average grain size of 120 µm. However, reheating to 1150 ^{0}C resulted in precipitate dissolution in the solute poor areas only

and achieved a bimodal grain distribution with an average grain size of ~220 µm in the coarse region and ~41 µm in the finer region. Kundu et al. (12) investigated the equilibrium precipitation / dissolution behaviour using Thermo-Calc thermodynamic software, and it was revealed that reheating to above ~1210 °C would cause complete dissolution in the same Nb content steel, producing a coarse grain structure agreeing well with Chakrabarti's (3) data.

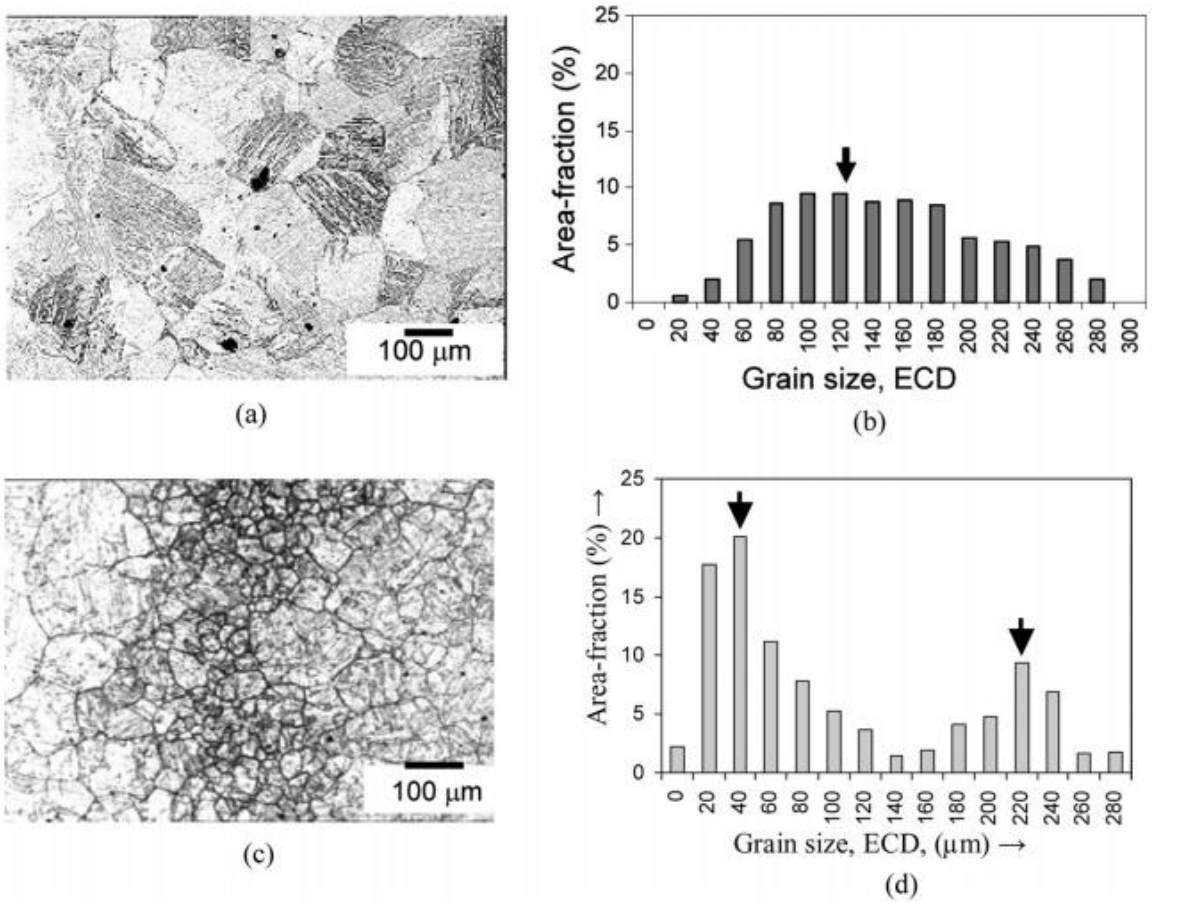

Figure 1.5. Example of two reheated temperatures a) and b) 1225 ^{0}C, and c) and d) 1150 ^{0}C. The temperature of 1150 ^{0}C shows a bimodal grain size (3).

Davis and Strangwood (11) state that a duplex grain size structure can form as a result of segregation. Since on reheating, within a critical temperature range, there can be inhomogeneous grain boundary pinning with the solute-poor regions undergoing precipitate dissolution. This leads to grain growth, whilst pinning precipitates remain in the solute-rich regions.

1.2.2. **Hot Deformation**

The production of high strength strip steels involves a variety of rolling methods, seen in Figure 1.6 with a representative rolling schedule in Figure 1.7. Figure 1.6 schematically shows conventional hot rolling (CHR), normalised hot rolling (NHR) and thermo-mechanical hot rolling (THR).

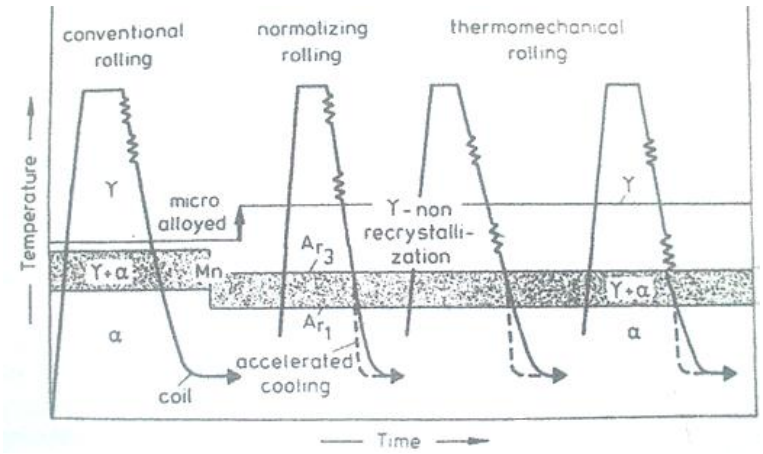

Figure 1.6. Hot rolling techniques involving thermo mechanical treatment, from left to right- CHR, NHR and THR (19).

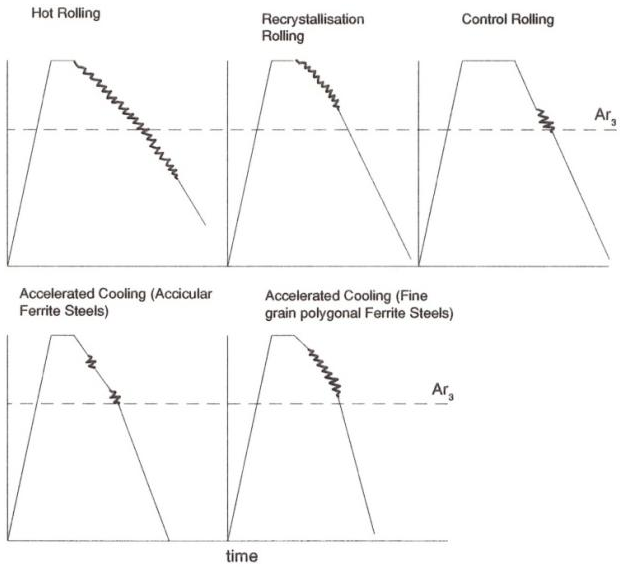

Figure 1.7. Rolling schedule for controlled microstructure, showing the different rolling schedules being carried out for different rolling schedules. Irregular line indicates the rolling process (20).

Thermo-mechanical controlled processing (TMCP), as seen in Figure 1.8, is a form of controlled rolling (CR) and is used to produce a fine grain size. Accelerated cooling (AC) can also be used after the final rolling pass to achieve a fine grain size (6, 21). Controlled rolling's main target is to produce a deformed austenite grain structure in the non-recrystallised region providing a large number density of nucleation sites for subsequent transformation to ferrite.

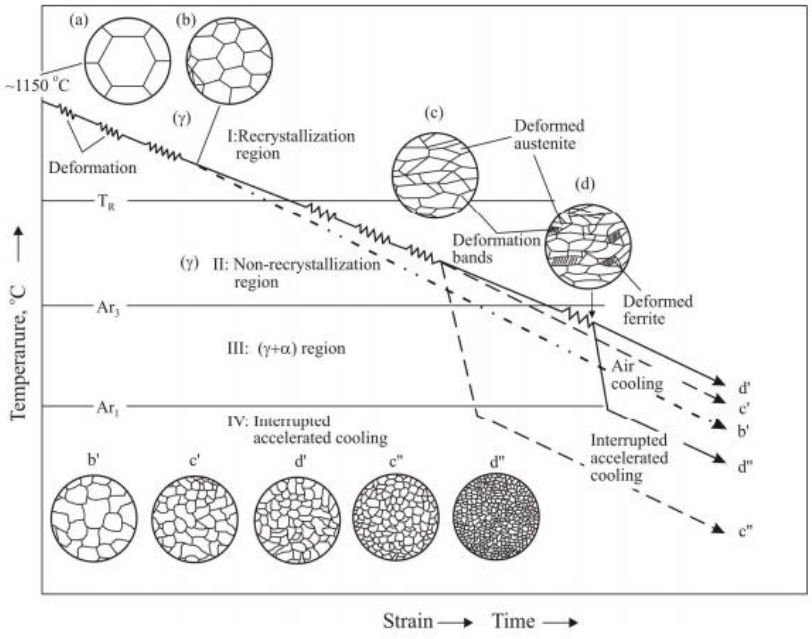

Figure 1.8. Schematic diagram of the four stages of a thermo-mechanical controlled process and the changes in the microstructure at each stage (22).

The hot rolling strip process is shown in Figure 1.9, where a continuous cast steel slab or part rolled plate is reheated before entering the rolling process. HSLA strip steels are hot rolled, and go through a roughing rolling mill (typical processing may involve reverse rolling), then a finishing rolling mill. Depending on final thickness it could go through a different number of rolling stands, although the speed of the rolling stands cannot be altered independently of each other. After the finishing rolling, the strip is water sprayed and coiled at a specific temperature. The strip is then stored and sold as a coil; the customer may then flatten and

section the coil as required. TMCR can be used to produce predominantly ferritic structures or martensite/ bainite structures which are produced by lower coiling temperatures.

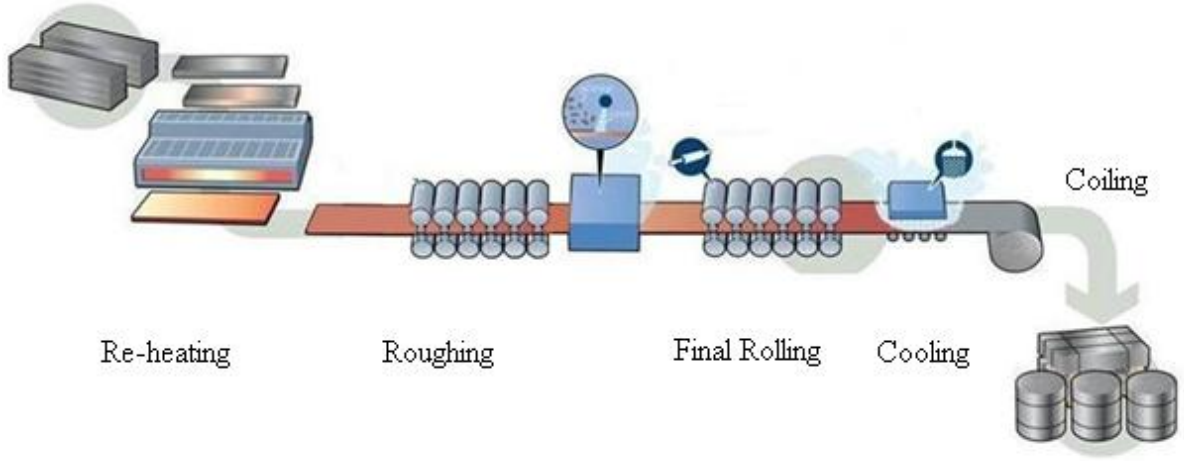

Figure 1.9. Illustration showing the hot strip rolling process (23).

1.3. **Recrystallisation**

Recrystallisation occurs when the deformed lattice is replaced by a new unstrained one through nucleation and growth of strain-free grains, which occurs during hot rolling of the strip. The orientation of the new grains will not be the same as the deformed grains they consume, producing high angle boundaries between them. The rate of recrystallisation depends on several factors, with the most dominant being the amount of deformation i.e. strain, deformation temperature and solute content (most particularly Nb content) (24). Figure 1.10 shows a schematic diagram illustrating the temperature range over which recrystallisation will take place during hot rolling. It shows a minimum temperature for complete recrystallisation and a minimum temperature for recrystallisation to start, i.e. 95% and 5% recrystallisation respectively. Between these values there is partial recrystallisation.

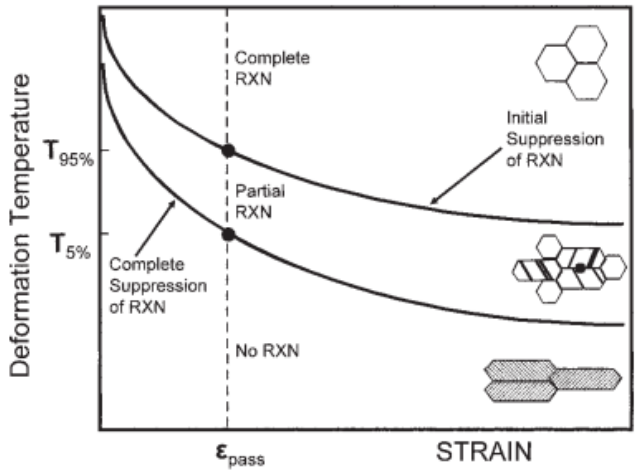

Figure 1.10. Schematic diagram showing the austenite microstructures resulting from various deformation conditions (deformation temperature and strain). Dashed line represents the effect of various deformation temperatures at a constant level of strain (ε_{pass}). $T_{95\%}$ and $T_{5\%}$ are the temperatures for recrystallisation. RXN- Recrystallisation (25).

During hot rolling (for example the roughing rolling during strip production) recovery; recrystallisation and grain growth can occur due to static recrystallisation (see Figure 1.11), Although generally the times involved between rolling stages are short enough to prevent grain growth occurring so that the recrystallised austenite grain size is refined, static recrystallisation occurs when a deformed structure is held at temperature for a set amount of time. For a C-Mn steel the critical strain required to initiate static recrystallisation is 7 % for the temperature range 900-1000 ^{0}C (1). Recovery is known to be slow during deformation, and the sub-grain boundaries are ill formed (which can be developed more by large amounts of deformation) (26). Dynamic recrystallisation is when recrystallisation occurs at the same time as deformation, it differs from static recrystallisation as larger strains are required, which are not generally possible during a single roll pass. To initiate dynamic recrystallisation a critical strain of 50-60% is required for a temperature range of 900-1000 ^{0}C (27). For microalloyed steels roughing rolling is carried out to refine the austenite grain size by static recrystallisation, with the finishing rolling passes being carried out below

the recrystallisation stop temperature to produce pancaked austenite grains. These provide a large number density of nucleation sites for subsequent transformation to ferrite.

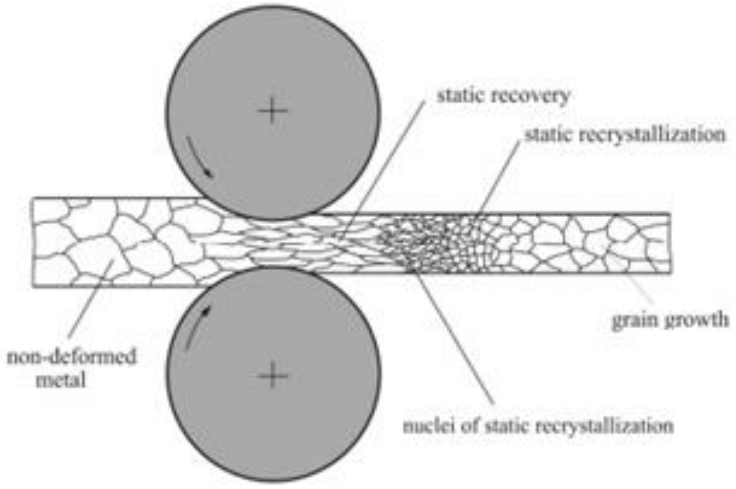

Figure 1.11. Schematic diagram showing the grain size changes during and after rolling (7).

Dutta and Sellers (28) developed equations to predict the recrystallisation behaviour of niobium bearing cast slab steels, which can be used to produce a recrystallisation - precipitation diagram (Figure 1.12). Equation 1.1 (P_s) predicts the strain induced Nb(C,N) precipitation start time (5 % precipitation), and Equation 1.2 (R_s) predicts the static recrystallisation start time (5% recrystallisation).

$$P_s = 3 \times 10^{-6}[Nb]^{-1}\varepsilon^{-1}Z^{-0.5} \times \exp\left(\frac{270{,}000}{RT}\right) \times \exp\left(\frac{2.5 \times 10^{10}}{T^3(\ln K_S)^2}\right) \quad \text{Equation 1.1}$$

$$R_s = 6.75 \times 10^{-20}D_0^2\varepsilon^{-4} \times \exp\left(\frac{300{,}000}{RT}\right) \times \exp\left(\frac{2.75 \times 10^5}{T - 185}[Nb]\right), \quad \text{Equation 1.2}$$

Where [Nb] is the amount of Nb in solution in austenite, in wt %; ε is the applied strain; T (in Kelvin) is the isothermal holding temperature where precipitation or recrystallisation is taking place; K_s is the super saturation ratio following the solubility, D_0 (in µm) is the average austenite grain size after reheating; and Z is the Zener-Hollomon parameter. Typical

values for these factors for low carbon cast Nb containing steels which had been reheated used by Kundu et al., (16) are: $\varepsilon = 0.3$, $\dot{\varepsilon} = 10s^{-1}$, $Q_{def} = 400$ kJ/mol and $D_0 = 120$ μm, with Kundu et al. establishing that the Dutta-Sellars equations did work well for a narrow band of composition, strain and grain size, but give under or over-predictions outside that range.

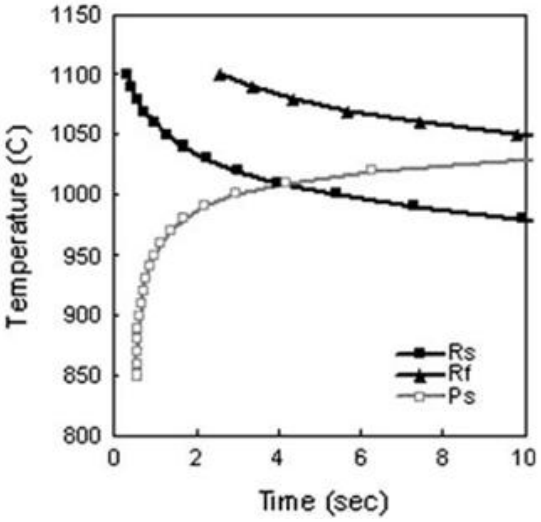

Figure 1.12. Precipitation- recrystallisation diagram for a homogenised 0.046 wt% Nb steel (mode grain size of 280 μm, reheated to 1225 °C for full Nb solubility). Rs= recrystallisation start time, Rf= recrystallisation finish (85% recrystallisation) time and Ps= precipitation start time (16).

If partial recrystallisation occurs, new smaller strain-free recrystallised grains will nucleate in-between strained grains which have become elongated during rolling. The sample will then contain smaller strain-free grains and elongated strained grains giving a bimodal structure (29). Figure 1.12 can be used to calculate the partial recrystallisation temperature range for a steel; this partial recrystallisation range will be increased in steels with Nb micro-segregation (26). Figure 1.13 shows the effect of microalloying additions on the recrystallisation stop temperature. Recrystallisation start and stop changes with composition, so different values will be linked to different areas of a microstructure, such as solute rich and solute poor regions. Figure 1.14 shows the difference associated with solute-rich and solute-poor regions for a steel with Nb segregation (12).

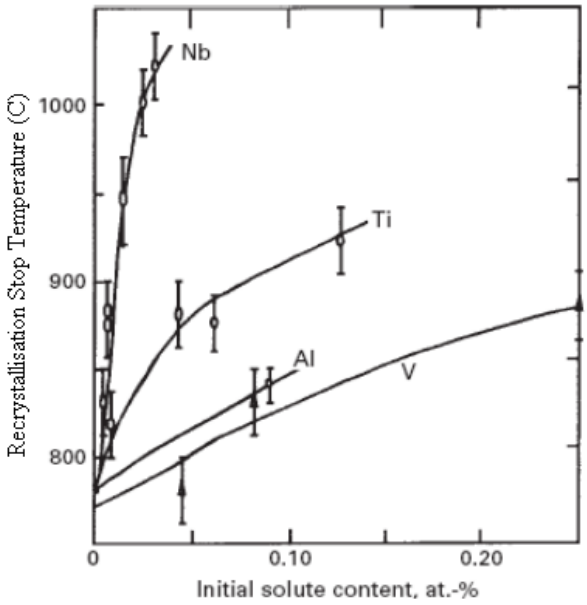

Figure 1.13. Graph showing the increase in recrystallisation stop temperature with increasing microalloying element in a 0.07 C, 1.40 Mn, 0.025 Si (all wt%) steel (30).

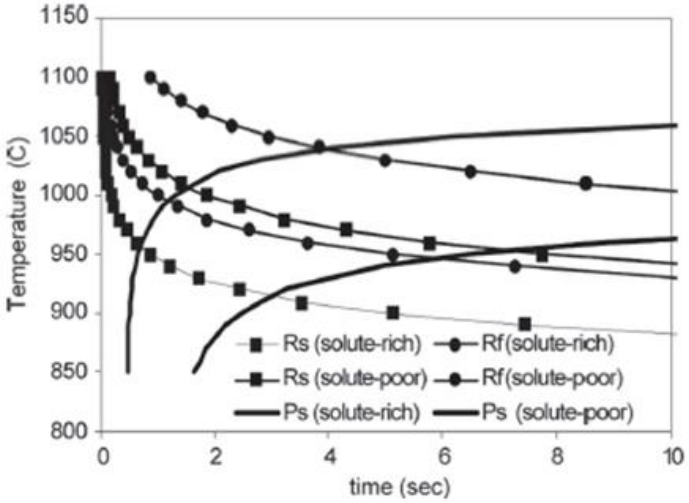

Figure 1.14. Recrystallisation- precipitation diagram for a sample reheated to 1150 °C, which accounts for segregated composition and a bimodal grain size (12).

1.3.1. **Cooling and Coiling Temperature**

Accelerated cooling (AC) can be applied after hot rolling, and has been successfully used for strip products and more recently plates (31). AC is added as it can produce a finer grained microstructure and greater precipitation strengthening (by producing finer and more effective

microalloying precipitates) (32). The amount of AC needed depends on the steel chemistry and if too much is used then it can result in the formation of metastable products (martensite and / or bainite) too little or too late then some degree of recovery will occur in the austenite, with no recrystallisation, which will produce coarser grains. Figure 1.15 illustrates the difference in nucleation sites of ferrite grains for three different processes: normalised, CR and AC. It can be seen that the AC steel produced more nucleation sites.

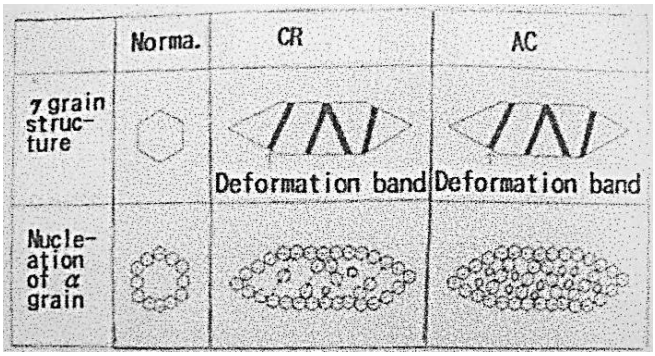

Figure 1.15. Nucleation sites for ferrite in normalised, controlled rolled and accelerated cooled steels (22).

An important influencing factor on the strengthening of a 700 MPa hot rolled high strength steel found by Yi et al. (33) when studying the fine precipitates of Nb-V-Ti microalloyed strip steel, was the coiling temperature, with the optimum conditions being a finishing rolling temperature around 800 ^{0}C and a coiling temperature between 400 and 500 ^{0}C. Figure 1.16 compares the difference in strength with different finishing rolling temperature (FRT) and coiling temperatures (CT), with the highest yield strength being that for a FRT of 800 ^{0}C and a CT of 475 ^{0}C. Yi et al. (33) stated that the ferrite grain size changed little with the change of FRT and CT, for specimens containing a fine ferrite grain size. The difference in precipitation strengthening among the specimens was concluded to be the factor causing the difference in mechanical properties.

Sha et al. (34) worked on a complex commercial Nb-V-Ti steel, investigating the effects of coiling temperature on precipitation (with the precipitates being very close to NbC in composition), at 650 ^{0}C, 600 ^{0}C and 550 ^{0}C with a cooling rate of 20 ^{0}C/s after hot rolling. Sha et al. (34) concluded that fine precipitation (under 10 nm) increased in volume fraction and there was a decrease in average precipitate size as the coiling temperature decreased.

Specimens No.	FRT / C	CT / C
1	850	480
2	800	475
3	800	350
4	750	560

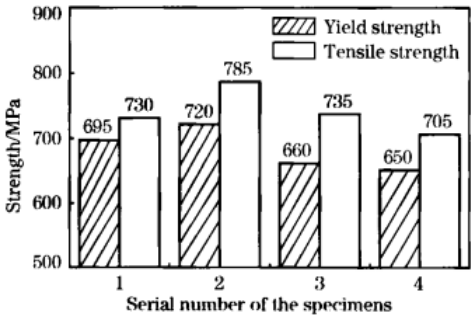

Figure 1.16. Strength of samples with different finishing rolling temperatures and coiling temperatures (33).

1.4. **Toughness**

Key properties for high strength strip steels include a high yield stress with good ductility and toughness - toughness is the ability of a material to resist failure caused by crack development. The toughness requirement for these steels set by Tata Steel is 27 J at -40 °C during Charpy testing. Charpy testing is a commonly used method as it is fast, economical and is used as a comparative test to measure the resistance to failure of a material to a load applied suddenly. It is not a direct measure of fracture toughness, but of impact toughness, impact transition temperature (ITT). Charpy tests are carried out on BCC structures to understand when a material behaves in a ductile or brittle manner; this is discussed further in section 1.8. As scatter in results in seen in Charpy testing tests are repeated at the same temperatures over a range of temperatures to achieve good data.

1.5. **Strengthening mechanisms**

There are five strengthening mechanisms used in steels: grain size refinement, solid solution, phase balance, precipitation and work hardening. The main mechanism in reducing the impact toughness transition temperature (see section 1.8), and increasing the yield stress is grain size refinement (35, 36).

1.5.1. **Grain size**

Grain size is known to have a dramatic effect on strength and toughness. The Hall-Petch relationship, Equation 1.3 indicates the dependence of yield stress on grain size (37).

$$\sigma_y = \sigma_0 + k_y d^{-\frac{1}{2}}$$ Equation 1.3

σ_y is the yield stress, σ_0 is the lattice friction stress, k_y is a constant and d is the grain size. σ_0 is the stress required to move a dislocation along slip planes in a BCC single crystal (38), regarded as the yield stress for a single crystal (8), which is sensitive to temperature and the chemical composition of the steel (39). The k_y value represents the slope in Figure 1.17 and is not sensitive to temperature, composition or strain rate.

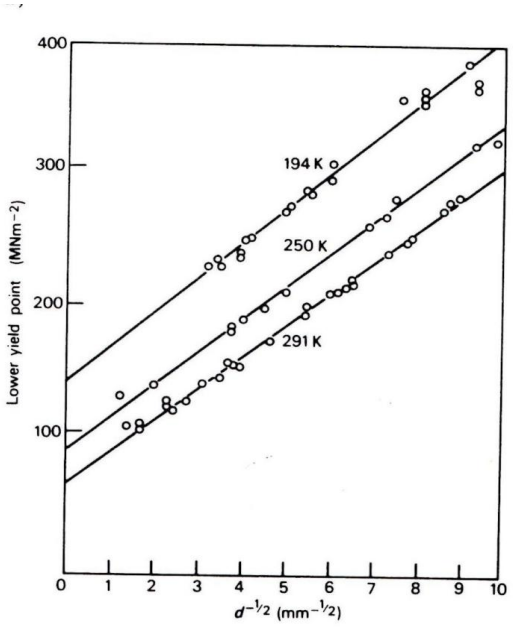

Figure 1.17. Dependence of the lower yield stress of mild steel on grain size (8).

Equation 1.3 (1) was derived for high angle grain boundaries (misorientation > 10 - 15°), an effect of low angle grain boundaries is that of mesotexture. Mesotexture causes groups of closely orientated grains separated by low rather than high angle boundaries to act as single large 'effective' grain which affects toughness (40). It is difficult to separate low and high angle boundaries using optical metallography, however, electron back scattered diffraction patterns (EBSD) can be used to determine the 'effective' grain size.

A refined grain size should increase toughness due to the need for greater crack deviation as grain size decreases. This is true for high angle boundaries, but less so for low angle boundaries where the deviation and energy penalty for crack propagation is much less. This is due to the symmetry of the cubic crystal, the maximum angle by which a cleavage crack has to deviate to find another cleavage plane is 45°, as the interplanar angles between the {100} cleavage planes are 90° (41, 20). Bhattacharjee and Davis (41) reported that grain boundary misorientation below about 12° did not significantly affect the cleavage crack path and therefore toughness. They proposed that when predicting the Charpy toughness of thermo-mechanically controlled rolled (TMCR) steels, low angle (<12 °) boundaries should be neglected when determining the effective grain size. Yi et al. (33) carried out work on hot rolled high strength steel which had a yield strength of 700 MPa and an entirely ferritic microstructure. It was established that the fine ferrite grain size and the precipitation strengthening were the dominant strengthening mechanisms and that good elongation and toughness were predominantly due to the fine ferrite grain size.

1.5.2. **Solid Solution Strengthening**

Solid solution strengthening increases the lattice resistance to deformation. In steels with a BCC iron structure there are interstitial and substitutional alloying elements, with the atoms having similar sizes to that of the host iron atoms going into substitutional sites. Dislocations interact with these solute atoms in different ways, with dislocations characterised as edge and screw dislocations. Edge dislocations have shear and hydrostatic components, while a screw dislocation only has a shear component. Substitutional atoms give rise to hydrostatic distortion and so will only interact with edge dislocations, whereas interstitial atoms interact with both hydrostatic and shear (asymmetrical distortions) components and so can interact with both screw and edge dislocations (1). The contribution of alloying elements in solid solution in ferrite to yield stress, σ_{ss}, is given by Equation 1.4 (37), where each element's composition is given in wt. %, with *Nf*- free nitrogen in solution.

$$\sigma_{ss} = 5544(C) + 5544(Nf) + 678(P) + 83(Si) + 39(Cu) + 32(Mn) + 11(Mo) - 31(Cr) \qquad \text{Equation 1.4.}$$

For low carbon, microalloyed steels the levels of carbon and nitrogen in solution are typically negligible (due to the formation of microalloy carbo-nitride precipitates) (39). The strengthening due to atoms in solid solution (Equation 1.4) can be removed from the friction stress (Equation 1.3) to reveal the contribution to overall strength from work hardening (σ_d) and precipitation (σ_{ppt}), Equation 1.5. Elements such as manganese, silicon and phosphorus exert significant strengthening effects in ferrite, Figure 1.18.

$$\sigma_0 = \sigma_{ss} + (\sigma_d + \sigma_{ppt}) \qquad \text{Equation 1.5.}$$

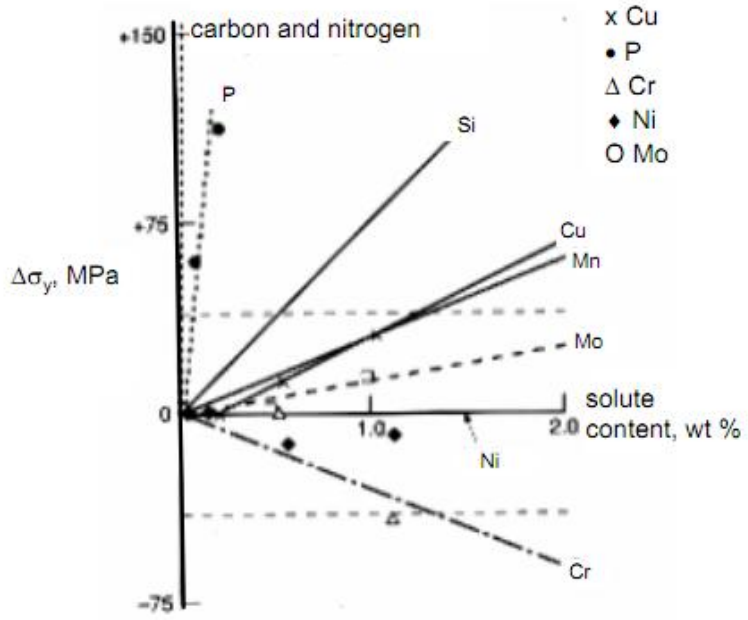

Figure 1.18. Strengthening effects of substitution solute atoms in iron (1).

1.5.3. **Phase Balance Strengthening**

In most steels a variety of phases can form, such as ferrite, pearlite, bainite, and martensite, each with different strength and toughness properties for the same composition. A predominantly ferritic microstructure can be strengthened by the presence of a second phase. Figure 1.19 shows the effect of pearlite on the tensile strength of a C-Mn steel, indicating that the more pearlite that is present the higher the tensile strength of the steel.

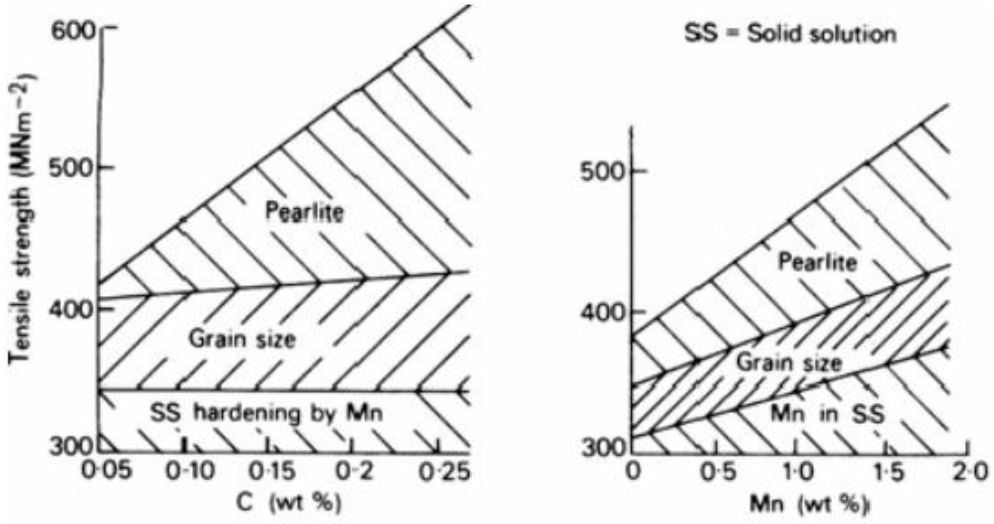

Figure 1.19. Factors contributing to the strength of C-Mn steel (42).

Dual phase (DP) steels are part of the advanced high strength steels (AHSS) class, and can be characterised by their improved formability, strength and crash worthiness, along with transformation induced plasticity (TRIP), complex phase (CP) and martensitic (MART) steels. DP steels contain a soft ferrite matrix and around 10-40 % hard martensite or martensite/austenite particles; see Figure 1.20 and Table 1.2 for effect of alloying elements on dual phase steels. The strength of the DP steel microstructure is controlled by the amount of martensite and ductility by the size and distribution of this phase.

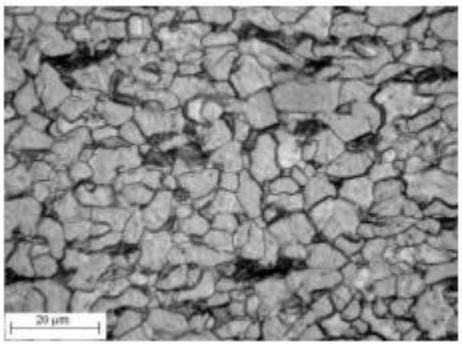

Figure 1.20. Micrograph of a dual phase steel (43).

Table 1.2. Effect of alloying elements in DP steel (43).

Alloying element	Effect and reason of adding
C (0.06–0.15%)	▪ Austenite stabilizer ▪ Strengthens martensite ▪ Determines the phase distribution
Mn (1.5–2.5%)	▪ Austenite stabilizer ▪ Solid solution strengtheners of ferrite ▪ Retards ferrite formation
Si	▪ Promotes ferritic transformation
Cr, Mo (up to 0.4%)	▪ Austenite stabilizers ▪ Retards pearlite and bainite formation
V (up to 0.06%)	▪ Austenite stabilizer ▪ Precipitation strengtheners ▪ Refines microstructure
Nb (up to 0.04%)	▪ Austenite stabiliser ▪ Reduces M_s temperature ▪ Refines microstructure and promotes ferrite transformation from non-recrystallized austenite

Figure 1.21 shows the separate effects of different strengthening mechanisms in two HSLA steels. It shows that the effect of elements in solid solution is similar for both and the important strengthening effect of precipitation strengthening in Nb-V specimens.

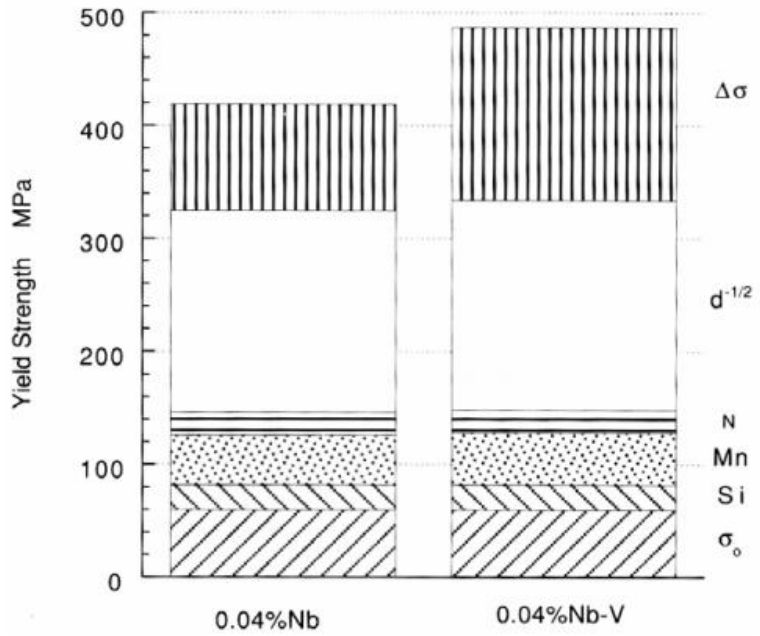

Figure 1.21. Strengthening contributions of different parameters on yield strength of hot-rolled 0.1% C-0.2% Si-1.4% Mn steel containing either 0.04% Nb or 0.04% Nb-0.07% V: Δσ – is the precipitate strengthening contribution (1).

Figure 1.22 shows the effect of cooling rate from the austenite phase. The faster the cooling occurs, the less readily carbon is able to diffuse reducing transformation temperatures resulting in metastable phases such as bainite and martensite. High strength strip steels of yield strength ≥ 700 MPa, are produced with a variety of microstructures; they can contain a predominant ferrite grain size with precipitates or they can contain a full bainitic microstructure, see Figure 1.23.

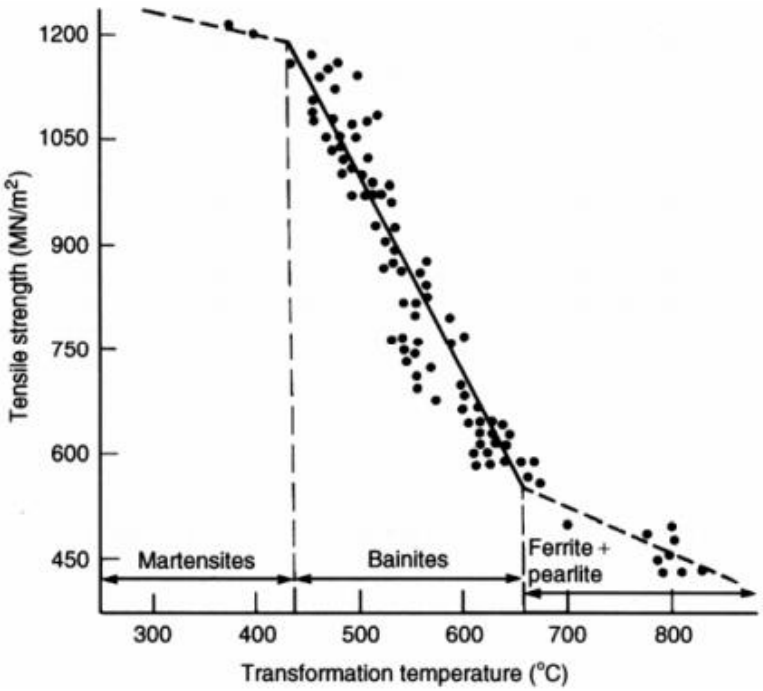

Figure 1.22. Influence of 50% transformation temperature on tensile strength via formation of different steel structures (37).

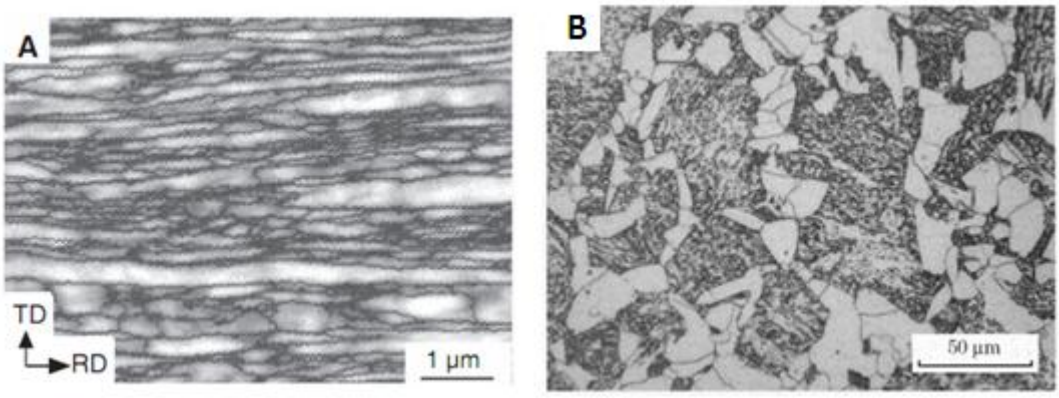

Figure 1.23. Micrographs of high strength strip steels, A) fine ferrite (44) and B) a low carbon air cooled bainitic steel containing 0.02 % Nb, yield strength 650 MPa (45).

1.5.4. **Precipitation Strengthening**

Precipitation strengthening works by inhibiting the movement of dislocations, with the particles interacting with the dislocations requiring a higher stress for continued dislocation movement, increasing the yield strength. In HSLA steels titanium, niobium and / or vanadium carbo-nitride precipitates are typically formed. The Orowan equation (Equation 1.6 (1)) is used to predict the strength for precipitation strengthening through the dislocation - particle interactions during slip. Figure 1.24 compares strength predication by the Orowan and the Ashby-Orowan formulae, and it shows that a larger number of finer precipitates provided a better strengthening effect.

$$\Delta\tau_y = \frac{Gb}{L},$$

Equation 1.6

Where G is shear modulus, b is Burgers vector and L is the spacing between the particle centres. L is related to the particle volume fraction (f) and particle diameter (X).

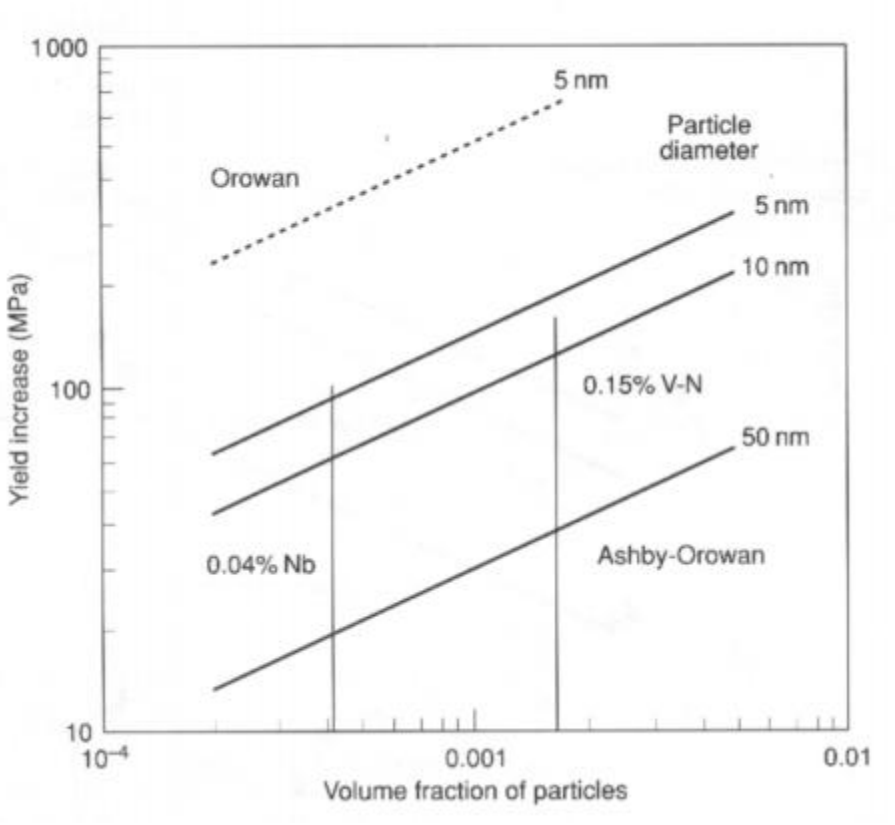

Figure 1.24. Addition to strength predicted by Orowan and Ashby-Orowan equations compared with the observed increments of yield strength in microalloyed steels (vertical lines are experimental data) (1).

1.5.5. **Work Hardening**

Work hardening is caused by a build-up of dislocations, including the formation of dislocation tangles and locks, making it more difficult to further deform the structure (1). Work hardening can occur in strip steels during cold rolling, rolling below the ferrite transformation temperature (warm rolling) and during subsequent forming operations (e.g. press forming / deep drawing).

1.6. **Alloying Elements**

The dominant elements in this study are the microalloying elements, which are known to be beneficial to strength up to certain quantity levels and under controlled processing conditions, forming a dispersion of fine strengthening precipitates. However when added at too high a

level, or the processing is not sufficiently controlled they can form coarse (>0.5 μm) particles or extensive dispersions which do not provide any strengthening benefit and can then reduce the toughness i.e. increase the ITT (46). In the sections below the main elements added to high strength strip steels are considered in more depth, and Table 1.3 provides an overview of the role of different elements on toughness.

Table 1.3. Qualitative effect of elements on the ITT (46).

Element or ratio	Effect on ITT	Comments
C	Increasing carbon strongly increases ITT	Pearlite%/C and = ~150
Si	Detrimental to Charpy performance	Benefits strength
Mn	Complex/ variable effect but generally beneficial	Can be beneficial to ITT but depends on ratio with C. High Mn moves the start of transformation to longer times and lower temperatures, giving a finer grain structure, finer pearlite interlamellar spacing, so reducing ITT.
P	Residuals: always detrimental	
S	Residuals: usually detrimental	Some evidence suggests increase in S reduces ITT for certain S levels
Cr	Probably deleterious	Controversial whether increases or decreases strength
Mo	Probably detrimental	Depends on steel type – usually improves hardenability, added to linepipe steels.
Ni	Generally reduces ITT	Typical levels in TMCR steels are <0.5%
Al total		
Al sol	Nominally improves	All steels Al killed, synergistic effect with nitrogen, aim ratio 8:1 Al:N
B	Strongly detrimental	Not added to TMCR steels
Cu	Possibly detrimental	Notable addition (with P) to weathering steels
Nb	Strongly reduces due to grain refinement effect	
O	Residuals: always detrimental	
Sn	Deleterious	Increasing amounts in scrap as increased recycling of refuse, (EU Directives)
Ti	Generally reduces ITT but can increase it if not processed carefully	Ti (CN) can restrict austenite grain growth and give finer grain structure but coarse particles (cuboids) can act as fracture initiators, reducing toughness
V		Dual benefit of grain refinement and nitrogen fixing is offset by embrittlement from fine-precipitate dispersion
N	Free N particularly detrimental (~Al and Ti levels)	N will also combine with Ti, V and Nb. To reduce free N it must be tied up in precipitates: AlN, TiN or Nb(C,N). AlN precipitates only slowly during cooling (coil cooling or after normalising usually sufficient). Fast cooling does not promote AlN formation. Ti is strong nitride former and will fix all available N provided Ti/N>3.4. V also forms nitrides but not as strong a former as Ti. Nb forms Nb(C,N) and takes only a small amount of N out of solution
REMs (Zr, Ce), Ca	Modifies Sulphide shape	Only really affects upper shelf energy, only usually used in linepipe. Zr now replaced by Ca
CEV	Generally ITT increases with increasing CEV	Individual elements in CEV formula have varying effect but generally the effect is to raise ITT. In the CEV formula only Ni is generally advantageous for ITT (CEV= C + Mn/6 + (Cr+Mo+V)/5 + (Ni + Cu)/15
Pcm	Generally ITT increases with increasing Pcm	(Pcm= C + Si/30 + (Mn+Cu+Cr)/20 + Ni/60 + Mo/15 + V/10 + 5B)
C:Mn	Low C/Mn ratio improves toughness	
Al:N		Affects free N level, strongly dependent on cooling rate
Mn:S		Affects volume of MnS, main effect is on upper shelf
(Nb,Ti, V):N	Ti beneficial if not a too high a level to form Ti(CN) cuboids	Ti very strong N former and will reduce free N level if Ti/N>3.4
Total Residuals (S,P,O,N)	Increasing residuals level Increases ITT	P particularly deleterious. S effect closely linked to segregation and orientation

1.6.1. **Effects of Chromium**

Chromium is a ferrite former, and gives significant strengthening effects in small additions but is expensive. It is generally added to steels to increase the corrosion and oxidisation resistance. Chromium increases hardenability, but reduces toughness on its own so that it is frequently used with toughening elements (i.e. nickel) to enhance the mechanical properties (47).

1.6.2. **Effects of Nickel**

Nickel is a substitutional alloying element and it is widely known to improve notch toughness, at lower temperatures (47). Grain size depends on mechanical and heat treatments used but it can also be affected by alloying elements. Nickel improves strength and toughness as it lowers the γ/α transformation temperature, which encourages the formation of finer ferrite grains. Nickel also reduces the grain boundary mobility (36). Petch (36) carried out an investigation into the effect of nickel on the cleavage of ferritic steels and found that it acts predominantly through alloy softening which gives protection against cleavage, and lowering of the k_y value (Equation 1.3).

1.6.3. **Effects of Molybdenum**

Molybdenum increases strength by substitutional solid solution hardening, whilst also stabilising alloy carbides and increasing high temperature strength. Molybdenum influences notch toughness through its effect on microstructure (47). Bhole et al. (48) noted that the addition of Mo is beneficial in a weld metal as it forms an acicular ferrite and bainite microstructure in place of ferrite with second phases and grain boundary ferrite. It is also believed to retard ferrite formation from the parent austenite, depressing the bainite start temperature in a HSLA Nb-Ti with a yield strength of 770 MPa (5).

1.6.4. **Effects of Titanium**

Titanium combines with nitrogen and carbon to form inclusions and precipitates; the precipitates aid in producing a fine grain size by grain boundary pinning at high temperatures, for example during slab reheating prior to rolling. Linaza et al. (49) classified TiN into two size regions, those which precipitate in the solid state are typically between 10 and 100 nm in size and can pin austenite grain boundaries, and those between 0.5 and 1 μm in size that form in the liquid steel and are ineffective at pinning grain boundaries. TiN particles in the size range 10 – 100 nm do not provide a large precipitate strengthening contribution as the number density is relatively low, the strengthening contribution is through their role on grain size. The large TiN particles can be detrimental to the toughness of steel by acting as cleavage crack initiation sites; this will be considered further in section 4. TiN tends to be the most soluble of the microalloy carbo-nitride precipitates (50). Figure 1.25 summarises the effects of titanium additions in HSLA steels.

Patel et al. (6) stated that, when strengths greater than 420 MPa are required, additions of vanadium are necessary to provide strength via secondary precipitation in the ferrite matrix along with precipitation of TiC. The use of titanium is normally required in small amounts <0.020 wt %, which precipitates as fine TiN that are useful in grain size control in heat affected zones (HAZ). The titanium will combine with nitrogen which will make the niobium in the steel more effective as it will avoid the formation of Nb(C,N), and promote NbC, which increases strength.

TiC precipitates with a plate-like shape at the austenite - ferrite interface with a size range of 2 - 200 nm in length. TiC provides grain refinement if formed in the austenite phase and

precipitation strengthening if formed in the ferrite phase (TiC can form on pre-existing TiN (51) or give strain induced precipitation on dislocations (39, 52)).

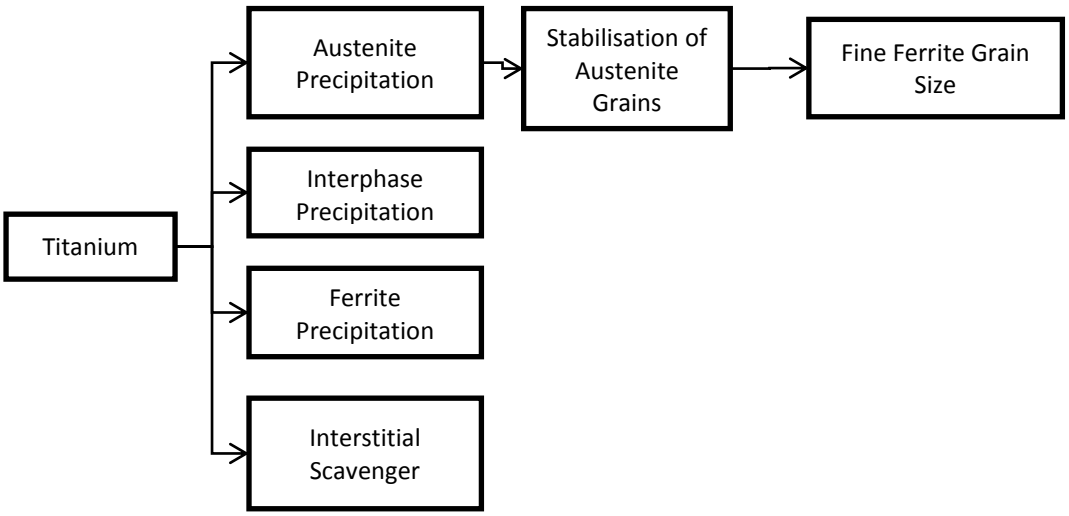

Figure 1.25. Effects of titanium on transformation and structure of HSLA steel (20).

The amount of titanium used for optimum benefit is an important factor with many authors reporting on the effective amount required. Zhang (50) carried out work noting that the optimum Ti content depends on the N content as Ti/N ratio also affects the TiN stability.

1.6.5. **Effects of Vanadium**

Vanadium is used as a precipitation strengthening element. V(C,N) forms at lower temperatures compared to titanium and niobium carbo-nitrides and so is smaller following TMCR but not as stable at higher temperatures. They are the last of the microalloying carbo-nitrides to form, and do so either at the γ/α interface or in ferrite. They are typically < 10 nm in diameter (39) (although can range from 10 - 500 nm (53)), compared to Nb(C,N) at around 3 - 15 nm and Ti(C,N) precipitates in the range 10 - 100 nm for the fine particles (39). The

effects of vanadium in HSLA steel are summarised in Figure 1.26. Vanadium is more soluble in austenite than in ferrite and it precipitates on transformation in a characteristic row formation.

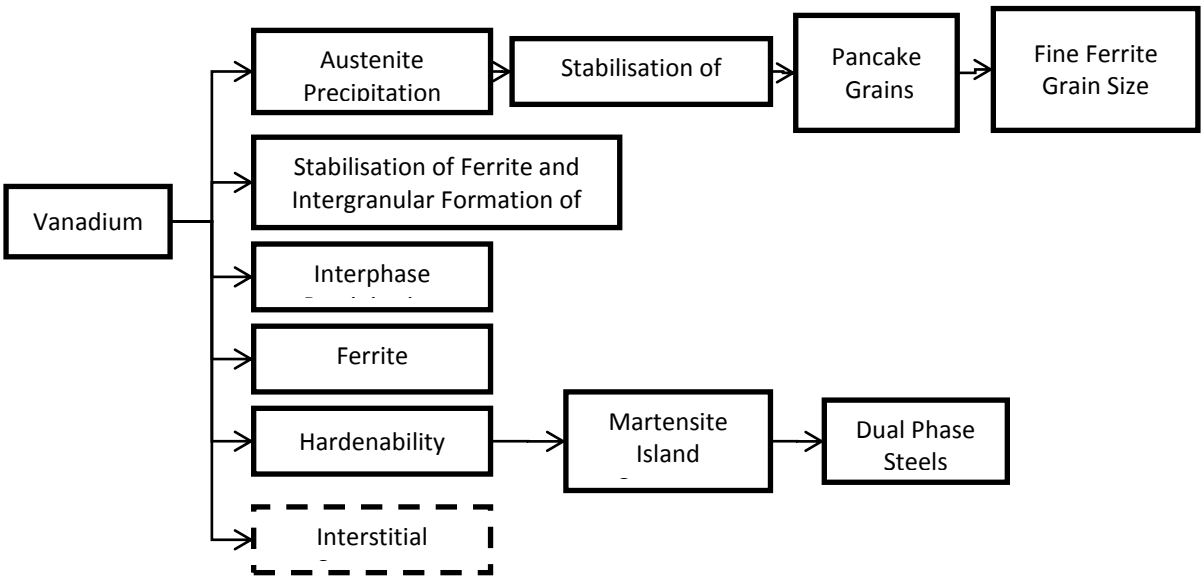

Figure 1.26. Effects of vanadium on transformation and structure of HSLA steel (20).

The strengthening increase seen from vanadium addition is between 5 and 15 MPa per 0.01 wt%, depending on carbon content and rate of cooling from hot rolling (section thickness). The cooling rate and the thickness of the strip will affect the precipitation strengthening, which is shown in Figure 1.27 for a 0.15 wt % V steel. In Figure 1.27 it is shown that optimum precipitation is at 170 °C/min. Lower than this and the precipitates will coarsen becoming less effective, higher than this and more V, C and N will stay in solution, providing a smaller fraction of precipitates decreasing the strengthening contribution (53).

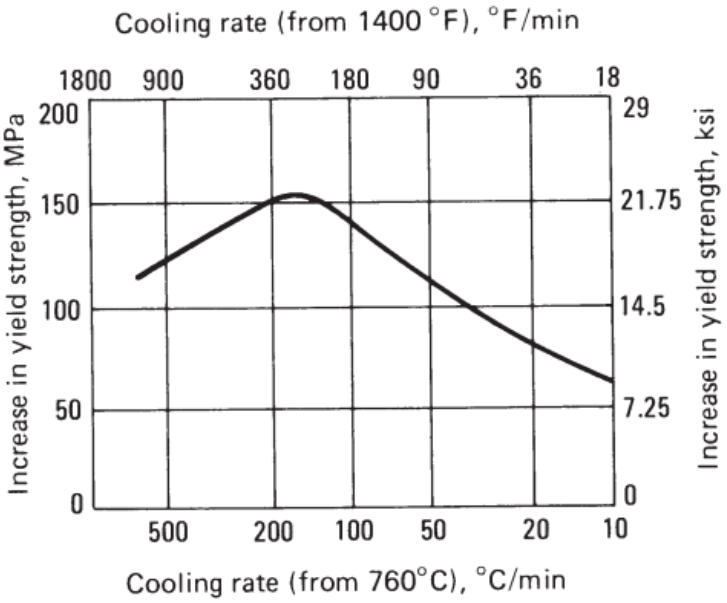

Figure 1.27. Effect of cooling rate on the increase in yield strength due to precipitation strengthening in a 0.15% V steel (53).

Klassen et al. (54) studied the effects of small additions of Ti (0.08 wt%), Nb (0.10 wt%) and V (0.085 wt%) on the fracture toughness of HSLA steels using J_{Ic} fracture tests and microstructural analysis. Nb and Ti significantly refined the grain size, which led to an increase in fracture toughness; V did not significantly refine grain size which resulted in no improvement in fracture toughness. Nb and Ti also decreased the size and volume fraction of inclusions, containing Ti, Al, S and Mn, which were circular in shape, resulting in an increase in fracture toughness due to fewer possible sites for void initiation. V had no effect on inclusion size and volume fraction, which also led to no improvement in the fracture toughness.

1.6.6. **Effects of Niobium**

Niobium affects steel strength and toughness through its role on grain size development during the hot rolling process. Nb affects the recrystallisation limit temperature and the recrystallisation stop temperature (6, 16), by solute drag and strain-induced precipitation

processes. This has been discussed earlier in section 1.3. For Nb to be effective it needs to be in solution after the reheat stage of processing. The effect of Nb is summarised in Figure 1.28.

Chakrabarti (3) and Kundu et al. (16) examined the effect of niobium segregation in similar as-cast slab, on the development of a bimodal grain structure during reheating and rolling. Although a bimodal grain structure does not affect strength greatly, it is known to have a detrimental effect on toughness (3). Figure 1.29 shows the effect of micro-alloyed additions (Ti, V and Nb) in mild strip steel, with Nb having the dominant effect.

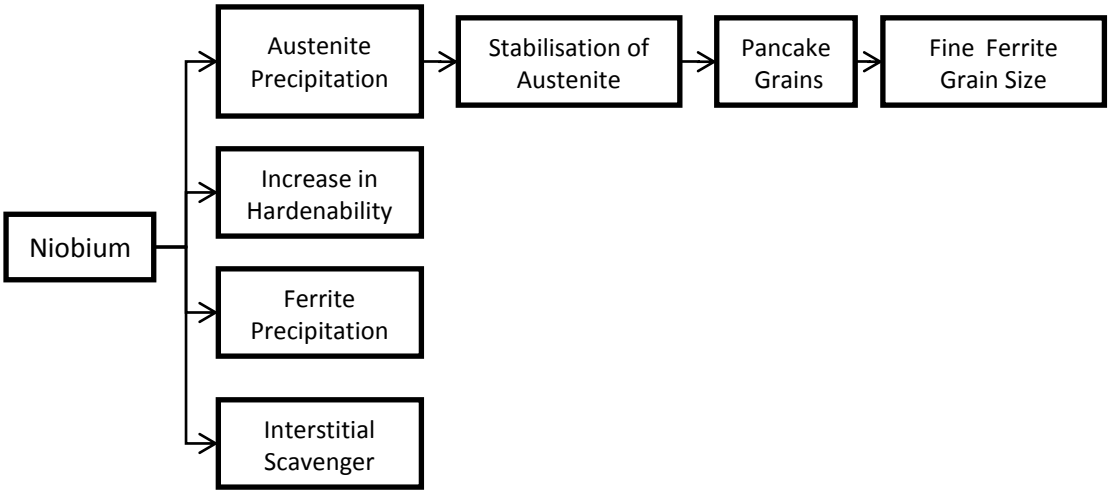

Figure 1.28. Effects of niobium on transformation and structure of HSLA steel (20).

Niobium is the main micro alloying element used in HSLA steels, normally at levels of 0.06-0.07 wt% generating a general yield of ~500 MPa (6). In thicker strips (>6 mm) vanadium is also added to guarantee a 500 MPa yield strength (6). Niobium is used due to its action as a grain refiner. This is due to its ability to raise the temperature at which austenite recrystallisation ceases. Nb also provides secondary precipitation hardening as Nb (C,N).

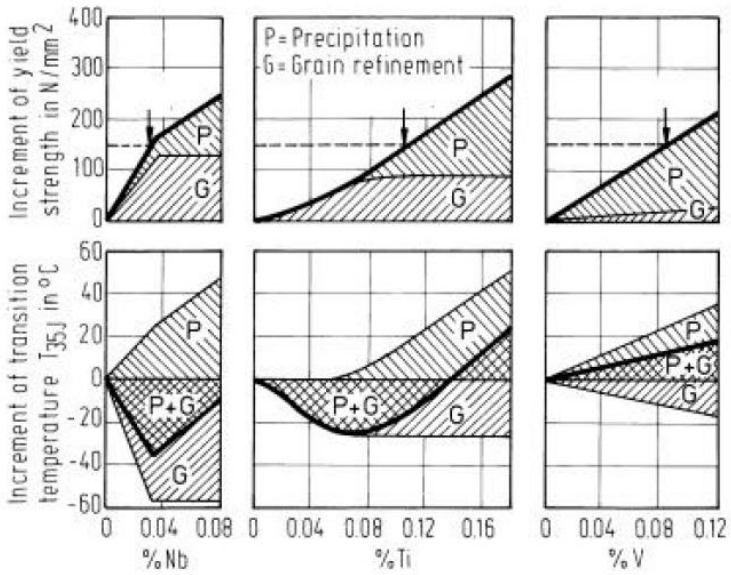

Figure 1.29. Effect of microalloy additions to the properties of a mild hot strip steel (6).

1.7. **Inclusions**

Typical inclusions present in steel include MnS, silicates; nitrides and oxides (55). MnS are typically elongated with a 'cigar-like' shape in the longitudinal orientation after rolling or forging, (Figure 1.30) and oval in the transverse orientation. The colour of MnS under an optical microscope is light grey. Silicate inclusions are also grey in colour but are typically more angular than MnS after hot rolling. Aluminium oxide inclusions are small, dark grey and angular; in rolled / forged steel the larger oxides tend to break up into smaller ones, which will be aligned in the rolling / forging direction (Figure 1.31). TiN inclusions are golden in colour (under optical microscopy) and normally angular/cuboidal in shape, (Figure 1.32). Multi-component inclusions can also be present; these can occur as, depending on the composition, with aluminium oxides forming first, then TiN inclusions can form on the alumina particles, with MnS nucleating on the sides of the TiN.

Titanium reacts with nitrogen to form TiN, which can occur as coarse inclusions (ranging from 0.5 – 12 μm in side length) when forming in liquid steel, and fine inclusions (ranging from a predicted 10 - 500 nm) when forming after solidification. Coarse TiN is ineffective at

pinning grain boundaries and may initiate cracking during toughness testing (see discussion in section 4.1).

MnS inclusions are present in steel as manganese is added to combine with sulphur, which is detrimental to the toughness. Al_2O_3 and SiO_2 form during deoxidisation and are hard particles. Al_2O_3 are typically angular which is detrimental to fatigue properties.

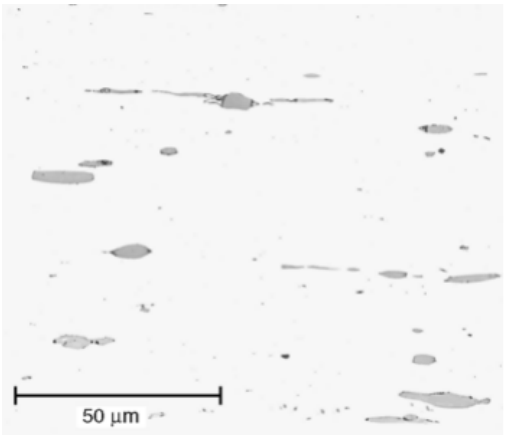

Figure 1.30. Micrograph of manganese sulphide (MnS) inclusions in an un-etched sample (55).

Figure 1.31. Micrograph of aluminium oxide (Al_2O_3) inclusions in an un-etched sample (55).

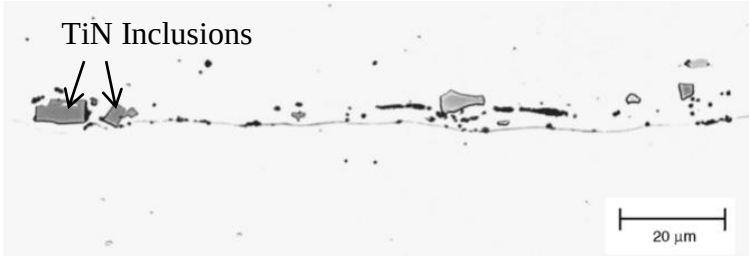

Figure 1.32. Micrograph of titanium nitride (TiN) inclusions in an un-etched sample, along with other inclusions (55).

1.8. **Ductile to Brittle Transition Temperature during Charpy testing**

Figure 1.33 shows a typical Charpy impact ductile to brittle transition temperature graph (DBTT) for a ferritic steel. Upper shelf fracture occurs by nucleation and coalescence of micro voids which produces ductile tearing (factors that affect upper shelf are in Table 1.4), whereas the lower shelf is characterised by cleavage failure (56). There are a variety of expressions used to define the Charpy impact transition temperature (ITT), the most common are 27, 40 or 54 J impact energy transition temperatures, the 50% fracture appearance transition temperature (FATT) - measured from a fractograph where the fracture surface shows 50% ductile and 50% brittle behaviour, and the 50% ITT, or DBTT (taken as the temperature on the curve corresponding to the energy midpoint between the upper and lower shelf energies).

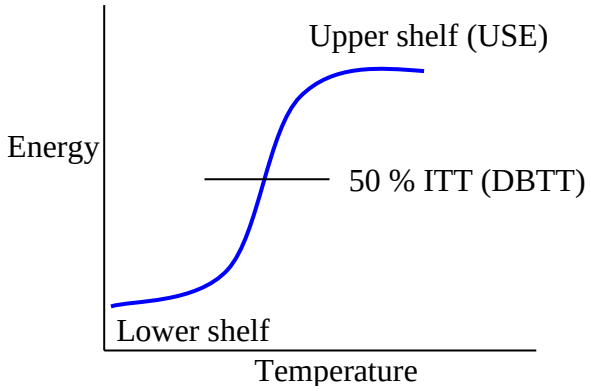

Figure 1.33. Typical Charpy impact energy temperature graph for a ferritic steel.

Table 1.4. Factors affecting Charpy upper shelf energy (46).

Factor	Effect on upper shelf energy (USE) of increasing level of factor	Comments
% Sulphur	Increasing S very strongly reduces USE	S is a main factor influencing USE. All other factors (RR, orientation, segregation etc) have limited effect on USE if S is low. Ultra-low steels show no effect of orientation
Mn/S ratio		
Manganese Sulphide type	Type II sulphides (stringers) strongly reduce USE	Type I= globules. Type II= rods (commonest form). Type III= equiaxed particles. Orientation effects are related
% Carbon	Increasing C strongly reduces USE	Together with %S, probably the strongest effect
REMs (Zr, Ce) or Ca	Modifies Sulphide shape to make them more equiaxed. When added correctly can increase USE	These elements act by modifying type II sulphides into type III Only really affects upper shelf energy, only usually used in linepipe. Ca treatment now tends to be used rather than Zr.
Residuals (S,P,O,N)	Always strongly detrimental to USE	
Segregation intensity	Increasing intensity of segregation tends to improve USE for the case of mid-thickness Charpies	Segregation is not affected by any rolling parameters
RRt	Increasing RRt reduces USE	The high RRt gives more elongated sulphides, which have lower Charpy energy. Orientation is linked with this.
Longitudinal vs transverse	Longitudinal gives higher USE	Ultra lower sulphur steels show no directionality
Starting slab thickness	Minimal effect	Slower cooling rate and higher resultant RRt may give slightly reduced USE but effect is not strong
Sub-surface v mid-thickness test position	Mid-thickness USE is lower than sub-surface	
Segregation	Mainly affects only mid-thickness Charpy	High casting temperatures give concentrated segregation: Mid-thickness Charpy energy reduced but sub-surface increased compared to diffuse seg.
Splits on fracture surface	Occurrence of splits reduces USE	Splits occur with strong texture due to severe final RR: also, splits are only likely if FRT<750°C.
$d^{-1/2}$	As $d^{-1/2}$ increases USE weakly decreases: however, the benefit of fine grain size on reducing ITT overrides this effect and grain refinement always preferred.	Grain refinement reduces upper shelf energy due to reduction in work hardening
Casting conditions (casting temperature, slab cooling rate)	High casting temp gives concentrated seg and reduces USE at mid-t, less effect at sub-surface.	Slab width, slab thickness, casting temperature, casting speed and cooling pattern all affect segregation pattern which affects upper shelf energy: main effect is for mid-thickness Charpies rather than sub-surface position.
Notch quality issues	Would expect little effect	On upper shelf ductility/plasticity probably overrides notch acuity effects

USE- Upper shelf energy
RRt- Final reduction ratio temperature
FRT- Finishing Rolling temperature

The yield stress affects the ductile to brittle fracture transition, therefore factors that affect the yield stress will also affect the ductile to brittle transition (24).

Figure 1.34 shows the general trend for the variation in fracture strength for ferrite, the yield stress and particle strength as well as the peak stress in the plastic zone around the crack tip. At low temperatures the particle cleavage strength and ferrite grain strength are lower than the yield and peak stress, therefore once the stress exceeds the particle cleavage strength, a crack will initiate in a particle and propagate. As the temperature increases the ferrite grain strength will exceed both the particle cleavage and yield stress but is lower than the peak stress, which means that the crack which initiated in the particle will not propagate across the first grain boundary unless the criterion for propagation from matrix to matrix is satisfied. At the highest temperatures, the ferrite grain strength and particle cleavage strength both exceed the peak stress, which results in no cleavage cracks forming in the particle or matrix, so the failure will be ductile.

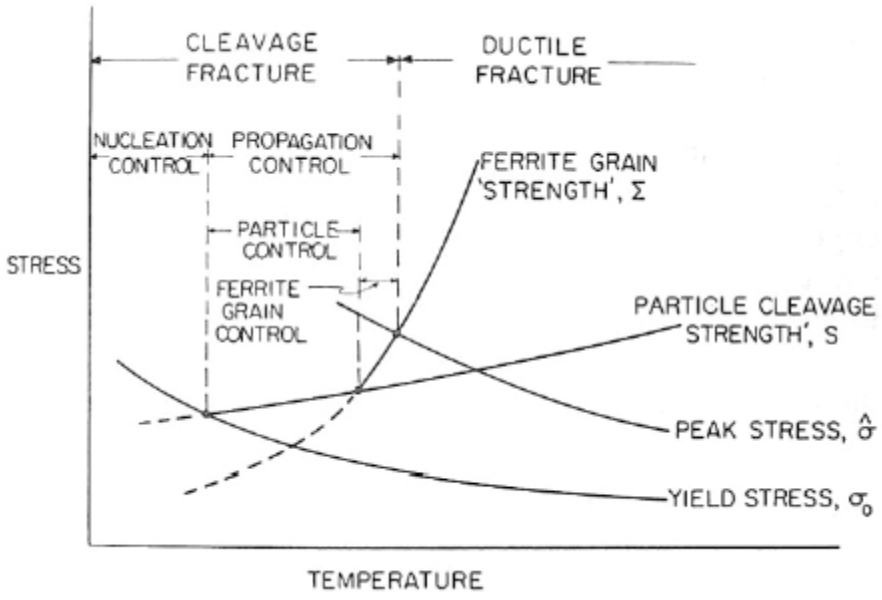

Figure 1.34. Variation of cleavage fracture strengths at different temperatures (57).

1.8.1. **Predicting ITT**

A variety of authors have looked at predicting the ITT for steel with Gladman - Pickering calculating the importance of grain size on ITT, Equation 1.7(1), (where N_f is free nitrogen). The Mintz et al. calculation is shown in Equation 1.8 (58) showing the importance of carbide thickness (t) as well as the grain size and the precipitation-hardening component of yield stress on the 50% ITT for a ferrite - pearlite steel. ΔY is the precipitation- hardening component (this will also contain some dislocation strengthening, for steels with a low finish roll temperature), which is calculated by Equation 1.9 (58).

$$50\ \%\ ITT = 19 + 44\ (\%Si) + 700(N_f)^{1/2} + 2.2(\%pearlite) - 11.5d^{-1/2} \qquad \text{Equation 1.7}$$

$$50\ \%\ ITT = 112(t)^{0.5} - 13.7\ (d)^{-0.5} + 15(\%\ pearlite)^{0.33} + 0.43\Delta Y + 20 \qquad \text{Equation 1.8}$$

$$\sigma_{np\_YS} = 43.1\ \%\ Mn + 83\ \%\ Si + 15.4(d)^{-0.5} + 1540\ \%\ N_f + 105 \qquad \text{Equation 1.9}$$

Bhattacharjee et al. (59) carried out a study on thermo-mechanically controlled rolled microalloyed steels, rolled to five TMCR schedules that contained varying amounts of mesotexture (groups of grains which contain low angle boundaries which could act as a single grain). For Equation 1.7 Bhattacharjee et al. (59) found it predicted the ITT well for heat treated steel (C-Mn steel which was heat treated at 1150 °C for two hours and then air cooled) using a metallographic 2D grain size. This is expected as the equation was developed for normalised ferrite/pearlite steel, containing a uniform microstructure. For the TMCR steels in this study (6 varying TMCR processes) the equation performed poorly with an average error of ~ 60 %, indicating that other factors are of importance other than grain size.

Equation 1.8, shows the importance of grain boundary carbides on the ITT, which gave a better prediction of the 50 % ITT than Equation 1.7, for the TMCR steels, but the accuracy was still poor indicating that other microstructural features may be having a influence (59). Bhattacharjee et al. (59) noted that a single facet can contain multiple grains which have a grain boundary misorientation of 12° or less in the TMCR steels, indicating that crack fronts may be treating groups of grains separated by low angle boundaries as a single grain. This would be at the mesotexture scale. If this factor is taken into account it will increase the ECD. Using this new ECD value increased the accuracy of the ITT equations in Bhattacharjee et al.'s (59) work, decreasing the difference between measured and experimental data from 60 to 20 °C for Equation 1.8. The ITT was also better predicted when using the mesotexture grain size values in Equation 1.7.

1.9. **Effect of coarse TiN particles on toughness**

Carbides and nitrides are known, along with inclusions and hard phases such as pearlite, to trigger fracture initiation (60). The controlling factors for cleavage failure in steel are the propagation of a crack across the particle / matrix interface (for brittle particles that crack readily), and the propagation of the crack across a matrix-matrix (i.e. grain) boundary. Petch (35) proposed that the fracture stress depends on particle size and grain size, whereas Curry and Knott (61) found that fracture is particle size-dependent. Echeveria and Rodriguez-Ibabe (60) found that, in steels containing TiN particles, the combination of a brittle particle and a large grain size caused cleavage fracture.

Fairchild et al. (62) carried out an investigation on the mechanism of brittle fracture in a microalloyed steel containing TiN inclusions. It was found that TiN inclusions were brittle and well bonded to the matrix. Within the plastic zone of a crack/notch tip, the strong martix-

inclusion bond allows matrix stresses to be transferred to the inclusion. Once a crack initiated in the TiN the strong bond permitted transfer of the crack through to the ferrite grain. Large TiN particles broke at lower stresses than smaller particles consistent with a Weibull volume effect. If cracks initiated in a large TiN particle at stress values too low to promote propagation of the crack arcoss the particle into the matrix, then the cracks were blunted and did not cause cleavage failure. This behaviour, and the low probability of finding large particles in the zone corrosponding to the maximum tensile strength ahead of the notch, explained the low probabilty of large particles (larger than 6 μm in the work carried out by Linaza et al. (63) being observed as cleavage initiators.

Zhang (50) found that the toughness of heat affected zone (HAZ) microstructures in Ti-containing HSLA steels depended on a complex interplay of matrix microstructures (grain size, carbonitride precipitates and alloy composition) and the presence of large TiN particles, but the importance of each of these factors was unclear. Du et al. (64) summarised the previous work on the role of TiN particles (Table 1.5) and concluded that there was no clear relationship between TiN particle size and grain size, for the different steels examined, when determining if TiN particles act as cleavage initiation sites. Du et al. (64) examined the Charpy ITT in HSLA steels which contained several Ti levels (0.006, 0.027 and 0.045 wt%) that had been heat treated to generate different ferrite grain sizes. It was found that when no coarse TiN particles were present the effect of grain size on the ITT was predicted well by the Mintz et al. equation (Equation 1.8). When coarse TiN particles were present, they were seen to initiate cleavage when the grain size was 9.5 - 27.3 μm, but not for a finer grain size (5 μm). However, it was concluded that although TiN did act as cleavage initiation sites in steels with the coarser grain sizes, there was no significant effect on the Charpy ITT, with the values also being predicted well by the Mintz et al. equation (Equation 1.8).

Therefore, whilst it has been reported that coarse TiN particles can act as cleavage initiation sites in steels, there is some uncertainity about whether they have any significant effect on the Charpy impact transition temperature. It is therefore likely that the magnitude of any effect of TiN particles on toughness is related to the TiN size, grain size and matrix strength.

Table 1.5. Summary of the role of TiN particles on fracture in steels (64). CTOD- crack tip opening displacement, PA- prior austenite.

Composition (all wt%)	**Microstructure**	**Grain size/µm**	**Cleavage initiating TiN particle size/µm**	**TiN acts as initiation site or not**	**Test method**	**DBTT/°C**	**Reference**
0.37%C, 0.0162%N, 0.015%Ti	ferrite + pearlite	5.5 (ferrite)	3.3	Yes	Charpy V notch (CVN) Impact test	65	(49)
0.23%C, 0.0075%N, 0.044%Ti	ferrite + pearlite	19.8 (ferrite)	3.2	Yes	4 point pending (4PB) test	N/A	(63)
0.052%C, 0.0062%N, 0.026%Ti	ferrite + bainite	50 (PA)	5	Yes	CVN Impact test	>15	(65, 66)
0.093%C, 0.0045%N, 0.045%Ti	upper bainite	100 (PA)	4	Yes	CTOD	>RT	(67)
0.089%C, 0.0048%N, 0.1%Ti	ferrite + bainite	110 (PA)	6.5	Yes	CTOD	20	(50)
		32 (PA)	5.5	Yes		-50	

1.10. **Effect of Texture**

The effects of texture on fracture can be considered in two parts; that at low temperature and that at high temperature. Fracture at low temperature occurs by brittle failure; with the most important factor being the number of {100} planes favourably aligned with the crack propagation direction. In the higher temperature range the fracture mode is a mixture of ductile and brittle, which then leads to full ductile fracture with the nucleation and

coalescence of micro-voids. Voiding is produced mainly through glide and pile-ups on slip planes, with the majority of slip planes being on the {110}<111> slip system for a BCC crystal (1,24).

It is known that the {100} planes are the preferred cleavage planes in ferrite, (68). But the major texture component parallel to the rolling direction expected in steel hot rolled as austenite is {110} (69). Ju et al. (68) implied that an increase in {110} plane alignment with the rolling plane could lead to an increase in plastic deformation during impact for longitudinal specimens, improving fracture toughness at room temperature in the upper shelf region. It has been reported that longitudinal specimens achieve a lower ITT, with the orientation of the notch also an important factor, Figure 1.35 (70).

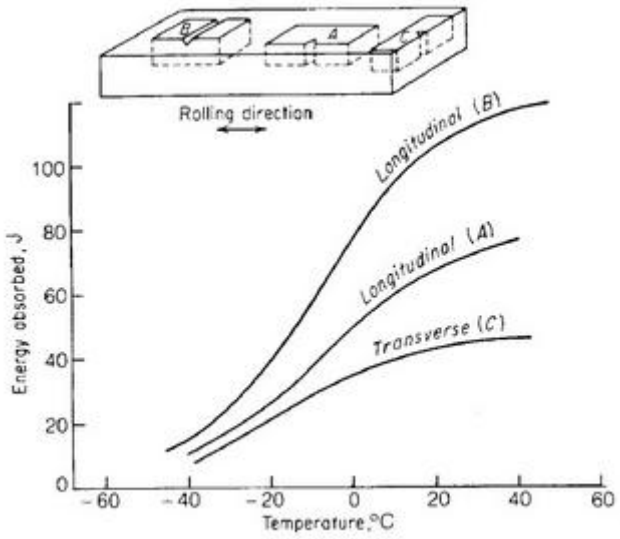

Figure 1.35. Effect of specimen orientation on the impact transition temperature for a HSLA steel (70).

1.11. **Splits (laminations, fissures)**

Splits, as shown schematically in Figure 1.36, will be described in the following section.

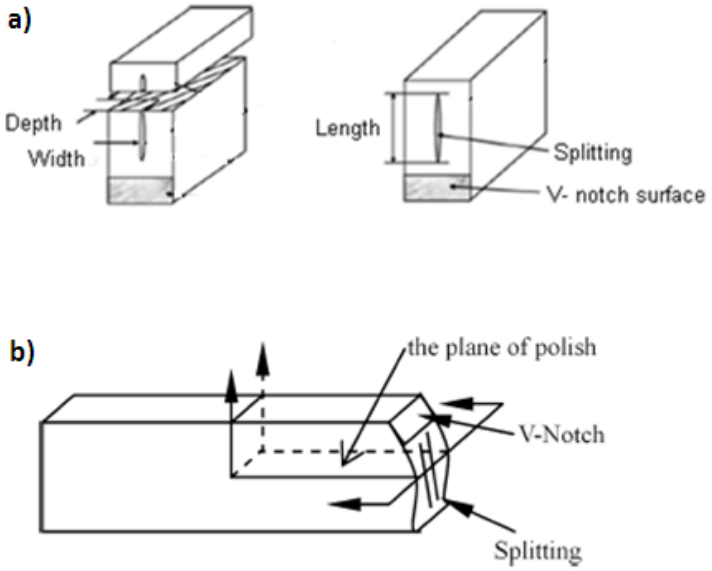

Figure 1.36. Split characterisation definition, a) characterisation of splits (71) b) measuring the depth (72).

It has been reported by a variety of authors that splits can be present on the fracture surfaces of Charpy specimens made from hot rolled strips, such as line-pipe grade steels; examples of splits are shown in Figure 1.37 and Figure 1.38. Splits have been found to run parallel with the rolling direction in HSLA steels, and are often described as a characteristic of these steels (73-77). Splits have been associated with delamination toughening, which improves toughness in a variety of materials such as ceramics, laminates and fine-grained steels (78).

Figure 1.37. Example of splits on the Charpy fracture surface of a low carbon steel which was controlled rolled with a finish roll temperatures below 760 °C (79).

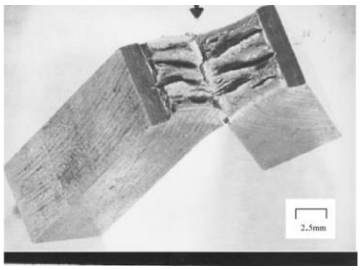

Figure 1.38. Example of splits on the fracture surface of a heavily control rolled steel (X65 grade linepipe) (75).

Splits have been found to lower the DBTT, which is desirable (71,73,75-77,79,80), but also to lower the upper shelf energy, which is undesirable (71,73,75,77,80). The net effects of splits are normally beneficial as the lowering of the upper shelf energy is not sufficiently marked and does not generally prevent the steel meeting specifications (often based on the DBTT or ITT) (75).

1.11.1. **Effect of splits on the tensile tri-axiality ahead of the Charpy notch**

Tri-axial tension occurs in tensile samples when there is a notch present, and in the area under the notch of a Charpy specimen. Tri-axial tension occurs when two tensile stresses act at right angles to one other (σ_x and σ_y), and can be resolved into equivalent shear stresses (τ_{xy} and τ_{yx}), as shown in Figure 1.39. The shear stresses are equal and opposite, reducing the effective shear stresses to the value determined by the stresses acting in the two directions (81). Shear stresses occur as, once the material under the notch begins to yield, this region

will try to shrink in the z plane, Figure 1.40, but due to the surrounding material which has not yielded, the material will not be able to do so, resulting in tensile stresses in the plane of the notch.

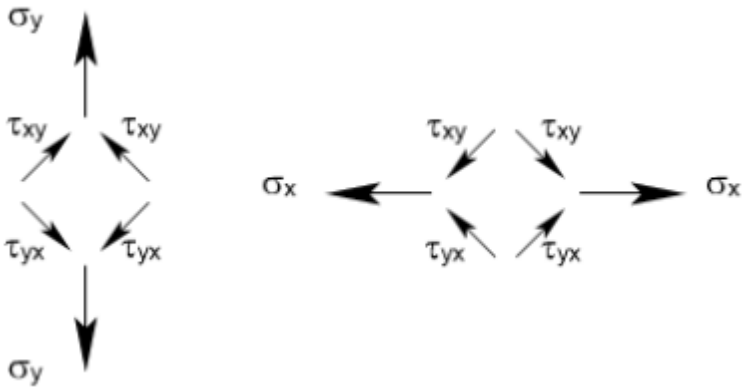

Figure 1.39. Tri-axial tension (81).

It is well documented that splits lower the Charpy impact DBTT due to the effect that they have on the tensile triaxiality ahead of the Charpy notch. The stress state at the crack tip influences the fracture energy and toughness of the material, which tends to increase as the tensile triaxiality decreases (24, 56, 80, 82). Tensile triaxiality can be reduced by relaxing the σ_{zz} stress component by the formation of splits that are perpendicular to the thickness direction, (parallel with the rolling direction), Figure 1.40. As splits occur, the thickness of the sample is effectively reduced, which decreases the σ_{zz} value to 0, at the surface of each split. The sample will then act as a group of thinner samples (74, 76), producing a lower ductile-brittle transition temperature (DBTT) - the closer the stress state approaches plane stress, the lower the DBTT (71, 80). As the stress becomes more relaxed and approaches plane stress, cleavage fracture will become less likely, reducing the DBTT. However, as the specimen is effectively split into smaller sections, the energy absorbed in ductile fracture is reduced, which is why the upper shelf energy tends to reduce when splits occur (83).

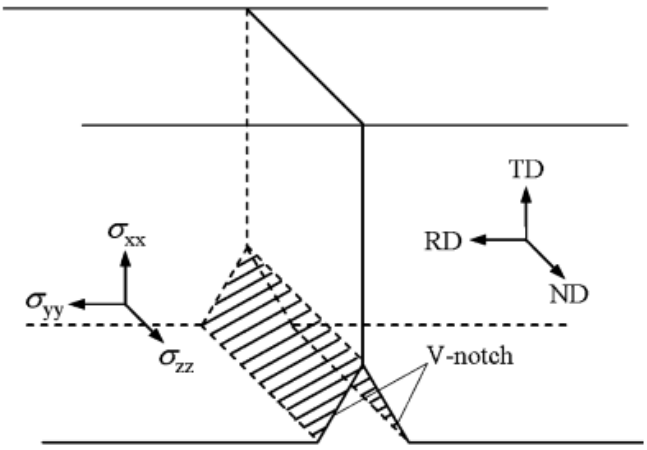

Figure 1.40. Geometry of a notch and directions of the stresses. σ_{xx}, σ_{yy} and σ_{zz}: normal stresses in the x, y and z-directions. The direction of σ_{zz} is parallel to the notch front. The biaxial stress state at the free surface is plane stress ($\sigma_{zz} = 0$) (80).

Bourell (84) and Mintz and Morrison (76) developed models to predict the conditions (e.g. impact test temperature) under which splits form, with Mintz and Morrison's work carrying on from Bourell's. It has been widely reported that splits do not occur at low impact temperatures when the sample is on the lower shelf, with main crack propagation via cleavage being favoured over the formation of split cracks. Splits are also absent on testing at higher temperatures, equivalent to the upper shelf position, when ductile fracture dominates (76). Bourell's (84) model was created to semi-quantitatively predict the fracture appearance using a rolling plane weakening model, Figure 1.41, and is described below.

The DBTT can be predicted from a plot of the temperature dependent uniaxial yield stress (σ_y) and transgranular fracture strength (σ_{CL}) as a function of test temperature Figure 1.41. Where the σ_Y and σ_{CL} curves intersect marks the uniaxial DBTT. Both the yield stress and fracture strength are sensitive to changes in microstructure and strain rate, and both values increase as the temperature is decreased. σ_{100} can also be seen in Figure 1.41 which is the stress required for cleavage fracture in iron single crystals when the test axis is parallel to the <100> direction (84).

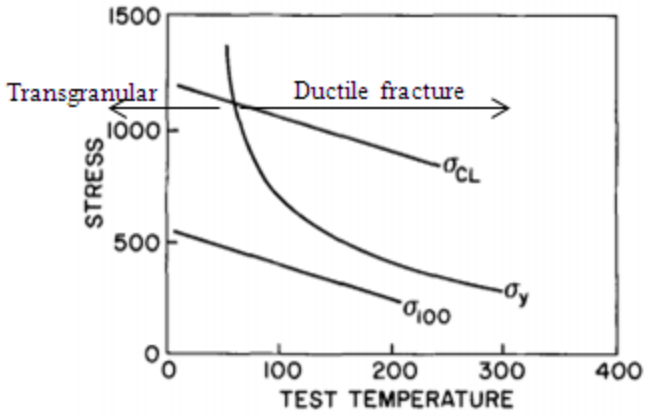

Figure 1.41 A schematic diagram of yield strength (σ_y) and transgranular fracture strength (σ_{CL}) for ferrous metals. σ_{100} is the stress required for cleavage fracture of iron for a single crystal orientated with the test axis parallel to the <100> direction (84).

Considering the stress state below a Charpy notch, when yielding occurs the stress acting in the short transverse direction (z) will be less than the stress acting in the x direction, 1.68 σ_y and 2.18 σ_y respectively (84) (2.18 was derived as the triaxial state of stress adjacent to a Charpy notch which is loaded in plane strain increases the tensile stress by as much as 2.18 times in the longitudinal orientation. Therefore the main fracture mode of plane strain is described by a plot of 2.18 σ_y and σ_{CL}, Figure 1.42).

When a specimen is loaded in plane strain the fracture mode can be described by plotting 2.18 σ_y and σ_{CL} and the intersection of these will be the plane strain DBTT. Bourell (84) states that when an isotropic material is loaded at low temperatures, as the fracture stresses are the same in the short transverse and longitudinal orientations, cleavage fracture will always initiate transgranularly on the main crack plane where the applied stress is greater during loading. For warm rolled steels the tendency for transgranular fracture will be higher in the rolling plane than in the crack plane, with Bourell claiming that this is due to the strong texture seen in steels in that study. The analysis in that paper indicates that if the short transverse transgranular fracture stress is less the 1.68/2.18 (77 %) of the longitudinal

transgranular fracture stress, at temperatures near the DBTT, transgranular cleavage will occur in the rolling direction before fracture on the main crack plane, resulting in splits. The triaxial stress at the notch will be relieved to a biaxial stress as the splits create internal traction-free surfaces. The longitudinal stress will drop from $2.18\,\sigma_y$ to σ_y depressing the DBTT to the intersection of these two curves. Bourell (84) makes the assumption that the weakness in the rolling plane is due to an alignment of {100} planes; this means that the transgranular fracture stress will always be lower in the short transverse than the longitudinal orientation. It is known that the stress required to initiate cleavage in a single crystal orientated with {100} parallel to the crack path, will be less than the stress required for transgranular fracture in the short transverse orientation, and as can be seen in Figure 1.41 the σ_{100} and σ_{CL} curves run parallel to one another, just at different stresses. Bourell (84) therefore assumed that the short transverse transgranular fracture stress would be in between σ_{100} and σ_{CL}. The departure of the short transverse transgranular fracture stress from the longitudinal transgranular fracture stress can be defined by Equation 1.10 (84).

$$\alpha \equiv \frac{\sigma_{CL}\ (\text{longitudinal}) - \sigma_{CL}\ (\text{short transverse})}{\sigma_{CL}\ (\text{longitudinal}) - \sigma_{100}}$$

Equation 1.10

Figure 1.42 shows a stress-test temperature plot for a steel where $\alpha = 0.35$ (if the longitudinal and short transverse fracture stresses are equal $\alpha = 0$, and values between 0 and 1 correspond to increasing amounts of texture e.g. from increased total rolling strain, a lower finish rolling temperature and reduced amount of recrystallisation). Indicated on the graph are three temperatures at intersections between the fracture stress and (scaled) yield stress values, as discussed below-

T_1- longitudinal and short transverse tensile stresses at yielding are lower than the transgranular fracture stresses when comparing the same directions, and becomes near bi-axis.

T_2- the short transverse transgranular cleavage stress is reached before general yielding, therefore splits are produced which will lower the longitudinal yield stress to σ_y. At this stage there is cleavage along the main fracture plane and splits.

T_3- due to the increase in the stress triaxiality, the longitudinal transgranular fracture stress is reached before the short transverse transgranular fracture so the specimen fractures by transgranular cleavage with no splitting.

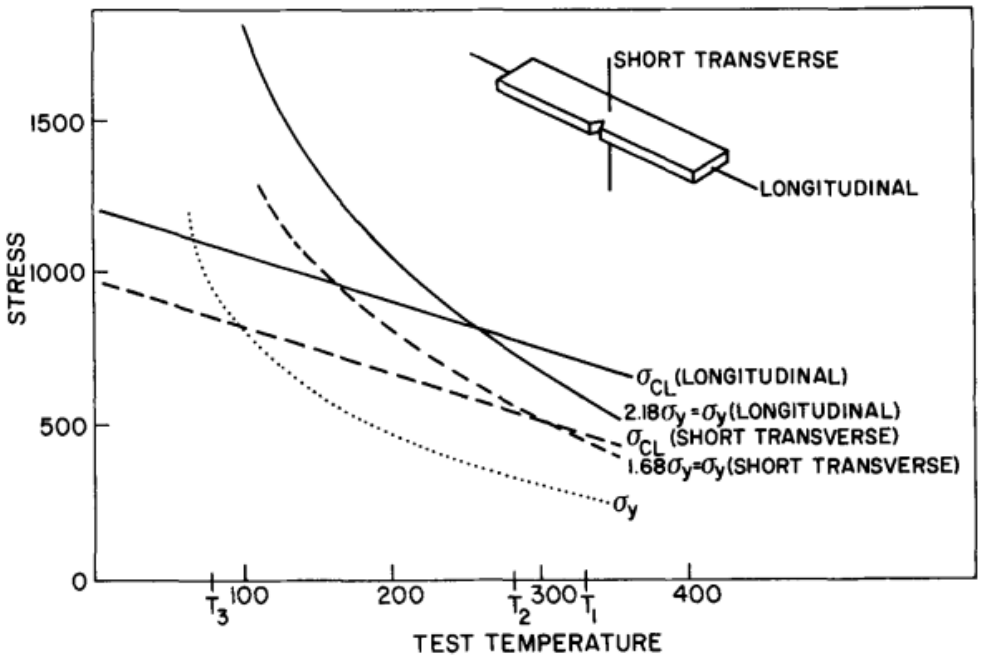

Figure 1.42 Yield stresses and transgranular fracture stresses (arbitrary units to maintain generality) for a steel with a given amount of rolling texture in the longitudinal (solid line) and short transverse directions (dashed line), with the uniaxial yield shown by a dotted line (84).

Mintz and Morrison (76) carried on the work by Bourell (84) and made modifications to the model as shown in Figure 1.43. They found through experimental measurements that splits did not form at temperatures below -80 °C (main brittle fracture planes weaker then split fracture planes) and >20 °C (weakness in the split plane is eliminated), for a HSLA steel. Mintz and Morrison worked on two types of steel - one that was heavily fissured (two or more splits) and one that was weakly fissured (one or no splits) termed h and w respectively. Considering Figure 1.43, when curves A and D cross over this should be the DBTT. The diagram was found to agree reasonably with the experimental data for the weakly fissured specimens; it was only when splitting was observed that the diagram become more complicated and further critical temperatures were identified:

T_2- Curve F cuts curve D; at temperatures below this cleavage occurs on the main fracture plane not on the rolling plane but at temperatures above this splits can form as the fracture strength is less on curve F than D. Splits being present on the fracture surfaces, cause the sample to act as an effective group of samples, which leads to a reduced temperature at which brittle failure occurs i.e. T_2 - T_4. T_4 represents the temperature at which tensile triaxiality is completely removed for brittle fracture (curve B intersects curve D). Between T_2 and T_1 Figure 1.43 shows that splits form and that fracture on the main fracture plane should be brittle not ductile. From the experimental results it was found that the main fracture showed ductile fracture surfaces for all cases. This could arise from the splits relieving the triaxial stress state, meaning that the stress state changes from a triaxial system (A) to a biaxial system (B). To achieve this change in stress state splits must occur before cleavage on the main fracture plane.

As high temperatures are approached splits start to disappear and above T_3 no splits are present (experimentally observed >20 °C), again meaning curve F cannot just be a straight

line like D. As the temperature increases the stress which creates the splits is reduced, and once T_3 is reached normal yielding will take place. At this point the fracture stress acting on the split plane (F), becomes greater than the stress acting on the split plane at yielding (C), meaning that there is not a great enough tensile stress to initiate the splits and so the overall fracture is ductile. The model agrees fairly well with the experimental results - although the model predicted splits at temperatures as low as -140 °C whereas experimentally they were only seen at temperatures down to -80 °C for the heavily fissured steels.

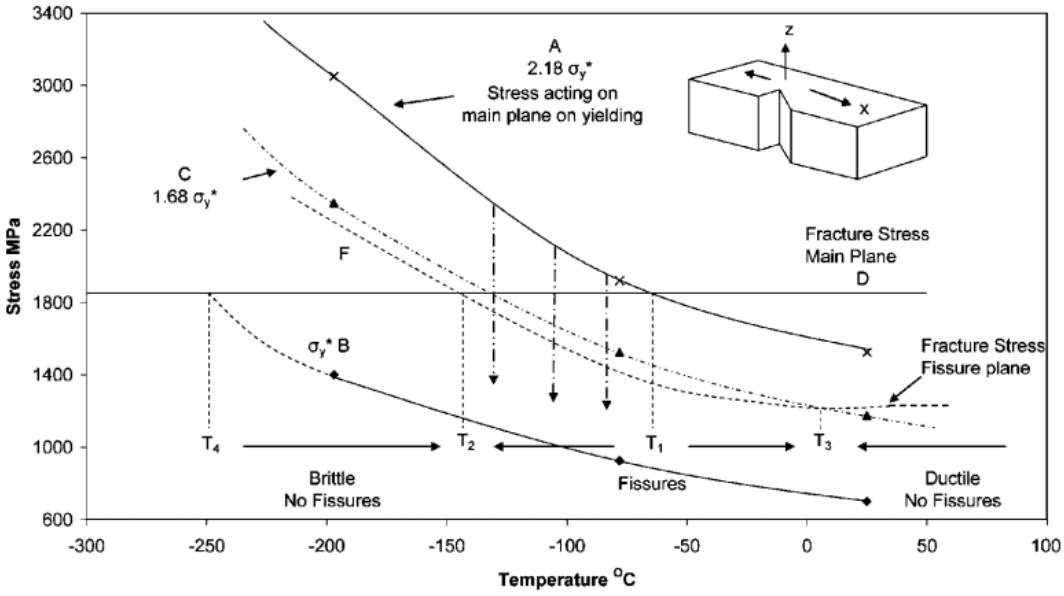

Figure 1.43 Schematic diagram showing how splits form over temperature(76). **Split plane-** Curve C- relates to the stress acting on a split plane during yielding (1.68 σ_y), Curve F- Fracture stress plane for the split plane- cannot be represented by a straight line as the brittle failure for the main fracture plane (D), due to failure of the split plane having a strong ductile element. **Main Fracture Plane-** Curve A- relates to the stress acting on the main fracture plane during yielding (2.18 σ_y), Curve D- Fracture stress plane for the main fracture plane. **Other** Curve B- relates to the stress acting for a biaxial stress state.

1.11.2. **Effect of Charpy specimen thickness on split formation**

Splits will form where the maximum constrained stresses occur. Schofield et al. (85) investigated the shape of 'arrowhead' fractures seen on drop weight tear test (DWTT) samples. As the maximum constrained stresses occur in the middle of the plate, the first and

most extensive split will occur there. This split effectively halves the specimen and reduces the constrained stresses. The presence of splits on the fracture surface means that the sample effectively acts as a group of thinner samples. Towers (86) and Wallin et al. (87) both came up with expressions for the shift in transition temperature (ΔT) due to changes in the Charpy specimen thickness (t in mm). Towers' relationship, reported by Bannister (88), applies to situations that do not involve the formation of splits (i.e. simply changes in sample thickness) and the change in the transition temperature (ΔT) is given by Equation 1.11. Towers equation applies to ferritic steels with room temperature tensile strengths in the range 334 - 688 N/mm^2 (88), and the transition temperature being defined at a constant absorbed energy per section.

Wallin et al.'s expression is based on sub-sized samples with a yield stress in the range of 200 to 1000 MPa, with a thickness range 1.25 to 10 mm and is given in Equation 1.12. Wallin et al.'s equation was derived for a normalised energy of 0.35 J/mm^2 which corresponds to 28 J in a full size Charpy specimen. It can be seen from the equations that a sub-sized specimen is predicted to have a lower transition temperature than a full-sized sample; it is also known that it will have a lower impact energy value (e.g. upper shelf value). BS 7910 Annex J (89), recommends the use of Wallin et al.'s equation. From Wallin et al.'s equation, a shift of -45 °C is expected in the ITT, if a specimen contains 3 equally spaced splits (e.g. effectively a set of 2.5 mm thick specimens).

$$\Delta T_2 = -0.7\,(10-t)^2 \qquad \text{Equation 1.11}$$

$$\Delta T_1 = 51.4\,\ln\left(2(t/10)^{0.25} - 1\right) \qquad \text{Equation 1.12}$$

A Charpy specimen will act as a group of thinner samples when splits are present. This in turn will decrease the DBTT (77, 79, 90). Embury et al. (90) found that the upper shelf energy decreased as the Charpy thickness decreases, which is consistent with the work by Wallin et al. (87, 91) and Towers (86) mentioned previously (Figure 1.44).

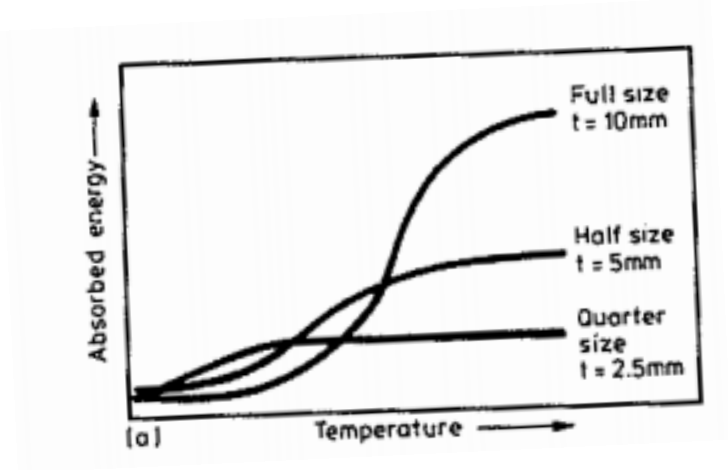

Figure 1.44. Plot showing absorbed energy against temperature for sub-sized Charpy specimens (86).

1.12. **Formation of split cracks**

Many authors have investigated the origin of splits, with texture (80), elongated MnS inclusions (44), microstructural banding (74), carbides on grain boundaries (75) and elongated grains (75) all being reported to play a role. These are discussed in detail below.

1.12.1. **Role of texture**

The presence of a strong crystallographic texture in an ultrafine grained steel (texture giving <111> and <001> directions parallel to the normal direction, ND), has been found to favour split cracks, with cracks being observed to propagate between grains separated by high angle grain boundaries. The texture was suggested to have been produced by large strain deformation below the A_1 temperature, and results in a lower DBTT (80).

Mintz et al. (75, 76) carried out work on heavily fissured (split) and weakly fissured HSLA samples (caused by differences in the rolling schedules) and found that steels which have a greater rolling texture (with a <200> component parallel to the rolling direction – this is equivalent to the <001> texture seen by Song et al. (80)) have a lower ITT and a lower upper shelf energy, due to the formation of splits. They investigated the misorientation angle of the grains by measuring the angle that the grain surfaces make to the plane of fracture. Misorientation angles were measured for samples with no or weak splits (normalised or controlled rolled samples), as well as samples with deep splits (only controlled rolled samples). Steels that had been normalised or had small splits had an average angle that the grain surface makes with the fracture path (in BCC structures cleavage tends to happen on {100} planes) of around ± 25 to 30°. Samples with deeper splits were more highly textured and had a reduced angle of ± 10 - 12°. Baldi and Buzzichelli (73) carried out work on HSLA steels which were finish rolled at low temperatures (approximately 700 °C); it was noted that long and sharp splits formed over a range of temperatures via transgranular cleavage due to the presence of a high density of {100} textured fracture planes (24). A characteristic of the splits shown in all steels investigated by Baldi and Buzzichelli (73) was that they propagated in a brittle manner, parallel to the rolling plane.

Joo et al. (78) carried out work on API-X80 steel to determine the role of splits and crystallography on the anisotropy of Charpy toughness, and found that splits and the preferred alignment of {100} cleavage planes contributed to the anisotropy in Charpy properties. When the Charpy samples were machined at 45° to the rolling direction the toughness was found to be worse (higher ITT), see Figure 1.45 as there was a reduction in the number of splits present. It was also noted that for Charpy samples with a 45° orientation that the rolling and transformation textures led to a large amount of {100} ferrite planes parallel

to the fracture surface, having a negative effect on toughness, due to brittle behaviour being favoured.

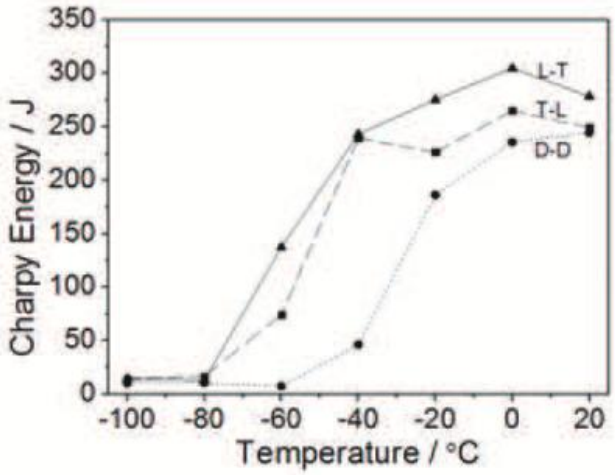

Figure 1.45. Charpy impact test results, fracture path orientations are L-T- longitudinal orientation, T-L- transverse orientation and D-D- Through thickness orientation (78).

1.12.2. **Role of inclusions**

Several authors have reported that splits initiate at inclusions, especially elongated inclusions from rolling. Mintz et al. (75) investigated inclusion banding in an X65 steel, which had been normalised and controlled rolled, with the controlled rolled specimens containing elongated MnS inclusions. Low blow Charpy impact tests were carried out incrementally by increasing the impact energy until a crack could be detected. The specimen was then ground to below the notch, and the surface examined to determine the cause of the splits. As with most normalised steels, splits were not present but crevices were observed, Figure 1.46 (75). The crevices were not deep enough to relieve the tri-axial stress, although occasionally a deep split (>0.8 mm) was observed when centreline segregation was present, but on average the crevices were between 0.3 and 0.4 mm deep. Also in the study normalised steels which had been controlled rolled showed splits present, which were associated with banded MnS inclusions and oxide inclusions, as shown in Figure 1.47.

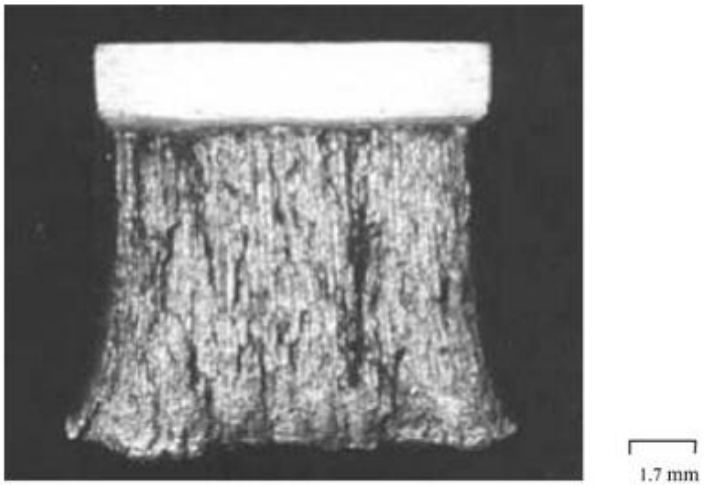

Figure 1.46. Fracture surface of a normalised steel X65, containing shallow marking (crevices), which could be related to pearlite banding, with the main fracture being ductile (75).

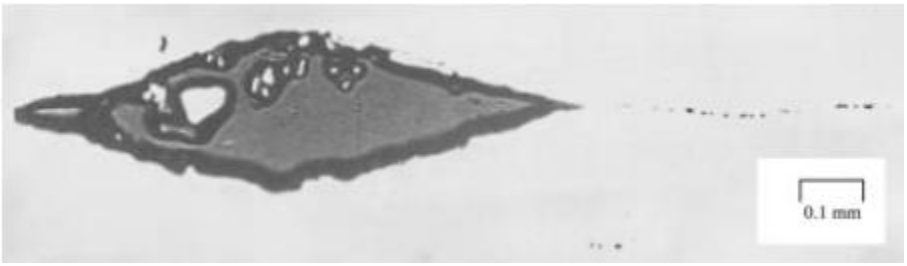

Figure 1.47. Mixed MnS and oxide inclusion present in the normalised steel tested at -60°C which contained a split of 0.8 mm depth; the split was observed to propagate along an inclusion band.(75)

Mintz et al.(75) also investigated the effect of MnS inclusions on the formation of splits in two X52 steels, both of which had been normalised to give a similar equiaxed grain size, but containing different sulphur levels, see Figure 1.48. The steel containing the higher amount of sulphur (0.030 wt.%) contained elongated inclusions, whereas the steel with the smaller amount of sulphur (0.012 wt.%) contained shorter more rounded inclusions. It was observed that the steel containing the short inclusions only occasionally produced splits whereas the steel with the elongated MnS inclusions produced deep splits although these tended not to

propagate for the full length of the sample. It can also be seen from Figure 1.48, that the samples which contained the elongated MnS inclusions, also contained pearlite banding, which could also be significant to the formation of split cracks. The author did not comment on this, so it is difficult to say if the pearlite banding played a role in split formation.

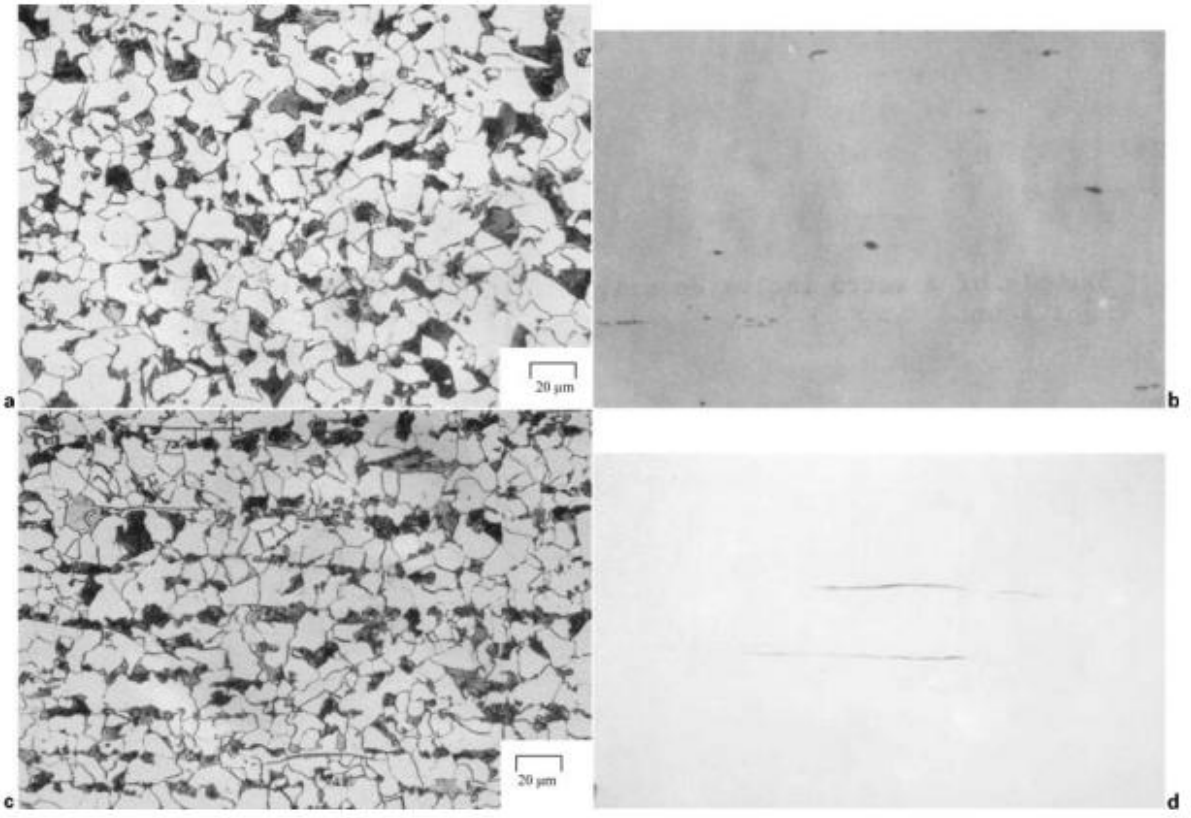

Figure 1.48. Steel X52, a) and b) show the microstructure and inclusions for the short inclusions and c) and d) show the microstructure and inclusions for the steel with elongated MnS (75).

Schofield et al.(85) examined the fracture behaviour for controlled-rolled pipeline steels and came to the conclusion that non-metallic inclusions may provide a large initiation site for brittle fracture in a certain plane, but to produce ‘arrow head’ marks (seen on DWTT samples) an absence of planar weakness (non-metallic inclusions) is required to allow the development of concentrated stresses. Although elongated inclusions have been found to initiate and / or influence the propagation of split cracks, steels not containing elongated inclusions can also show splits (73).

Work carried out by Morrison (83) and Mintz et al. (75), termed splits associated with inclusions as ‘woody’, as they are not comprised of a single dominant split crack. The crack associated with the inclusions effectively divided the material into small units (crevices), with shear failure connecting these cracks and resulting in a lower ITT, Figure 1.49.

Work was carried out on cleaner steels where splits occurred in the Morrison study, see Figure 1.50. The formation of these splits was ascribed to the fact that the steel has an elongated microstructure and is textured due to being rolled in the ferritic region. The difference between inclusion-orientated woody fracture and splits is that, although they both form in the ductile region, woody fracture disappears as the test temperature increases to that of the upper shelf, Figure 1.50.

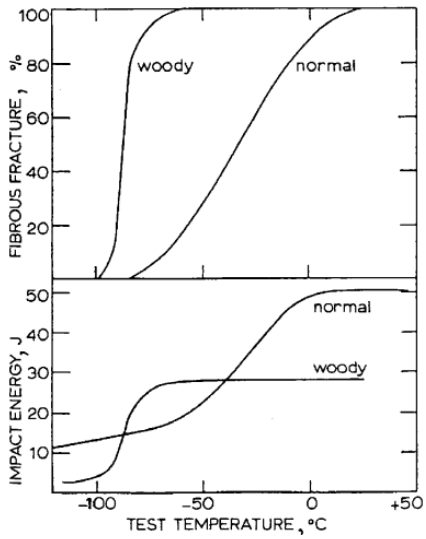

Figure 1.49. Charpy curves for steels showing normal and ‘woody’ fracture; the steels had a similar composition but the steel showing ‘woody’ split behaviour contained elongated sulphides (83).

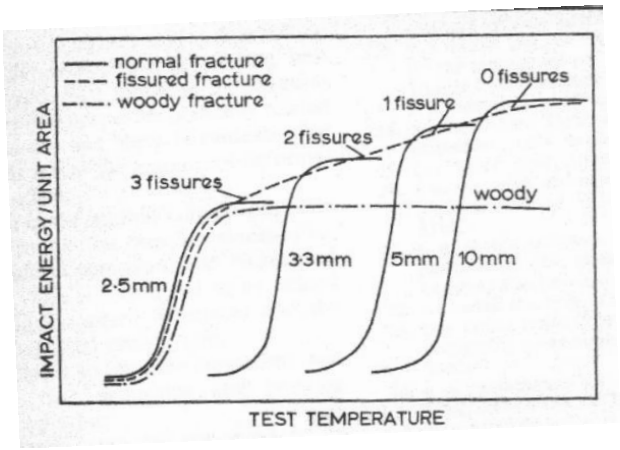

Figure 1.50.Schematic relationship between the impact properties of samples of various thicknesses and various fracture types (83).

1.12.3. **Role of cementite particles and carbides on grain boundaries**

Song et al. (80) found that, for an ultrafine grained 0.2%C–Mn steel (composition 0.22 C, 0.21 Si, 0.74 Mn, 0.004 P, 0.003 S, 0.001 N and 0.029 Al, wt%), the greater the alignment of cementite particles in the material and crystallographic texture in the rolling direction (caused by processing/ heat treatment conditions) then the greater the number of weak planes, which led to an increased tendency to form splits. When cohesion between the cementite particles and the matrix is weak these can act as an initiation site for cracks. Work has also been carried out on mild steel containing discrete carbides, which were found to cause micro cracks leading to cleavage fracture (92), however splits were not observed since the carbides were not aligned. Mintz et al. (77) found that splits were always initiated by second phase particles such as carbides or inclusions but that the propagation of these splits then became intergranular, due to the presence of elongated grains in the steels tested. The steels used in that study were an X65 grade, 4 types of plain C-Mn steel and a higher strength ferritic steel which contained high amounts of Ti and Nb (0.032 Nb for one composition and 0.085 Nb and 0.128 Ti for another composition, all wt%). Reducing the level of sulphur present (0.0120 to 0.0016 wt%) did lead to a reduction in the number of splits forming, but this was relatively small, indicating that the carbides played a more significant role on split crack formation than

sulphides. Figure 1.51 shows the intergranular nature of the split cracks observed and the elongated nature of the ferritic grains.

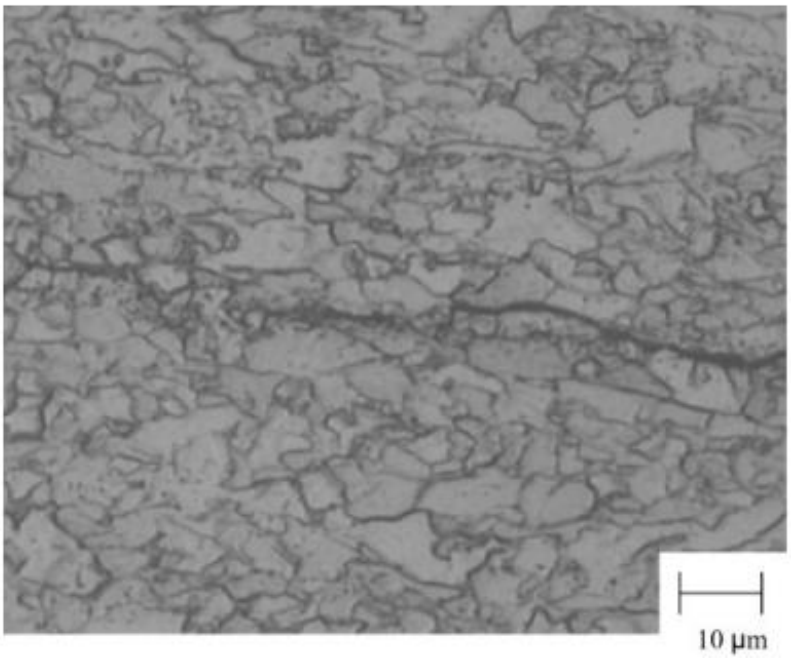

Figure 1.51. Optical micrograph showing a split crack propagating by intergranular cleavage in a Nb-Ti steel (77).

1.12.4. **Grain Elongation**

Grain elongation in hot strip steels is caused by the use of low finishing rolling temperatures, which also causes different textures to form. This section covers the reported effects of rolling temperature and grain elongation on splits.

Splits have been seen on the fracture surface of controlled rolled steels where the finish rolling temperature was in the two phase ($\alpha + \gamma$) region (a low finishing rolling temperature (FRT)) (56), however there are not as many reports of splits being observed in strip steels with a relatively high FRT. Bramfitt and Marder (79) carried out an investigation on the splitting phenomenon in a vacuum induction melted high purity Fe 1 wt % Mn alloy, which did not contain the undesirable factors that had previously been stated as initiation sites for

splits, such as inclusions, pearlite, and grain boundary carbides / nitrides. Finish rolling temperatures were varied from 960 - 150 °C with splits being observed parallel to the rolling direction for steels rolled below a finishing temperature of 760 °C. Figure 1.52 shows that the lower the finish rolling temperature the lower the upper shelf and ITT, with more splits being present on the fracture surface (Figure 1.53).

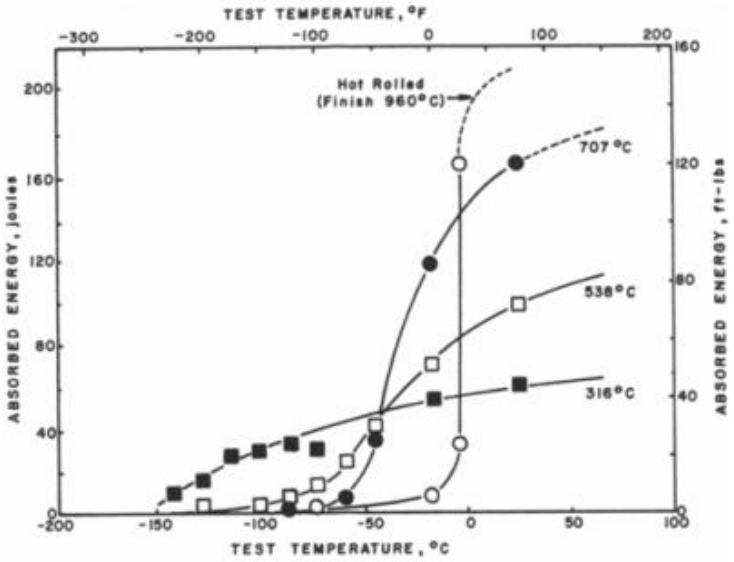

Figure 1.52. Charpy curves for specimens with different finish rolling temperatures (79).

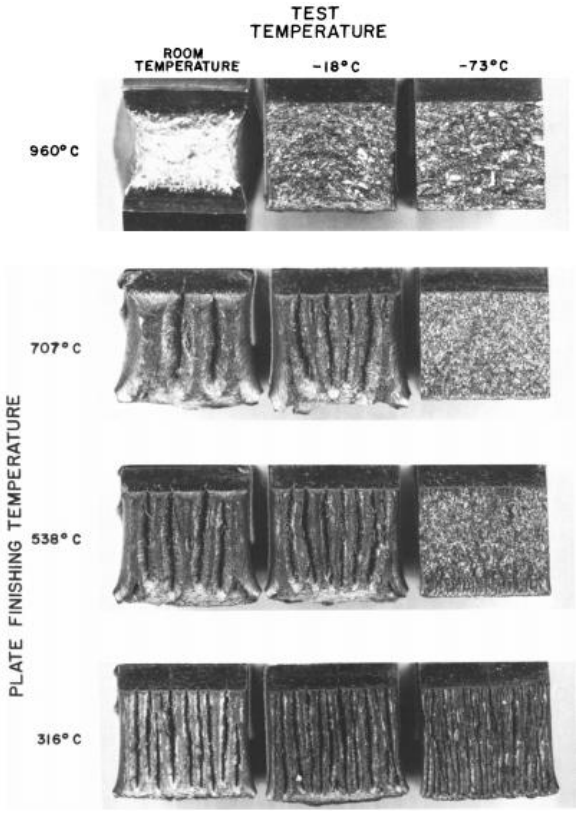

Figure 1.53. Charpy fracture surfaces for samples with different finish rolling temperatures (79).

It has been reported that the presence of splits can be caused by elongated 'pancaked' grains in the microstructure (75-77, 79). Bramfitt and Marder (79) stated that splits were found in steels rolled with a finishing temperature between 760 and 150 °C, with the number of splits increasing as the temperature decreased. Splits were observed to propagate by decohesion along grain boundaries which created a ductile tensile type failure, with decohesion of grains apparent due to the smooth split surface. Grain elongation was the parameter identified to be most responsible for the splits, with splits propagating when the grain elongation reached a critical point, in this case an aspect ratio of 3.4.

In another investigation by Mintz et al. (77) a C-Mn steel was given increased rolling reductions from 0 - 40% at 600 ^{0}C. The previous processing history was reheating to

1000 ^{0}C, rolled 40 % in the austenite region (950 °C), cooled to 760 °C, then another 40 % reduction in the two phase austenite / ferrite region (760 - 720 °C), then air cooled to 600 °C before the final rolling reductions. From Figure 1.54 it can be seen that the higher percentage of reduction resulted in a lower upper shelf energy and lower DBTT, along with a greater number of splits. Table 1.6 compares the fracture appearance, grain aspect ratio, strength and impact behaviour for two steels with different rolling reductions. Considering the C-Mn steels in Table 1.6, it can be seen that as the low temperature rolling reduction increases so does the aspect ratio of the grains, along with the yield stress (due to dislocation hardening). This results in an increase in the number of splits seen on the fracture surface with a consequent reduction in USE. It is normally expected that dislocation hardening would increase the ITT by ~0.45 °C MPa^{-1} (93). This indicates that the 40 % reduction sample, which gave a ~200 MPa increase in strength, should have a 90 °C increase in the ITT. Instead, due to the presence of splits, a decrease of 30 °C is observed in the ITT. In the steels rolled to a reduction of 10 and 20% the ITT values are higher compared to no reduction. This is due to the fact that only a few splits are present and would be expected to only partially cancel out the large increase in ITT expected due to the increase in yield strength. In that study texture arguments were said to be unlikely to be of importance, and were not measured, as splits occurred prominently along the grain boundaries, with splits occurring when a specimen went from having equiaxed grains (no splits), to elongated grains (splits).

To summarise this particular work the main factor relating to the formation of split cracks (and the different number of split cracks observed) is the amount of grain elongation, with warm rolling altering the grain shape. It should also be noted that investigations on split crack formation where the same steels were normalised found that no splits occur in the normalised material due to its equiaxed grain shape (72,77).

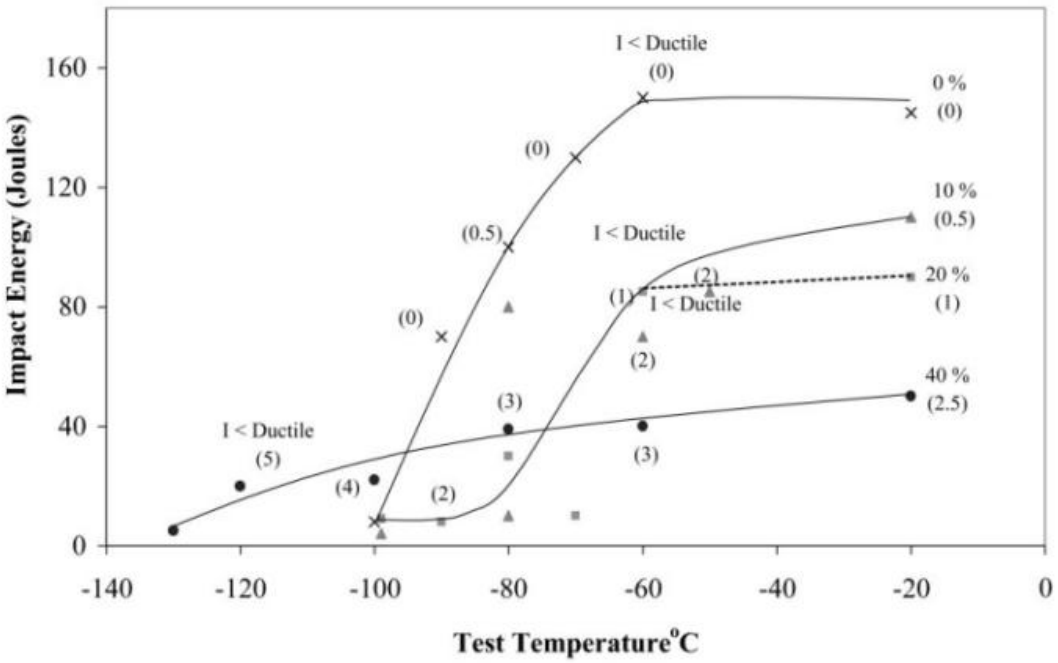

Figure 1.54. Impact transition curves showing the effect of rolling reduction at 600°C on a C-Mn steel in longitudinal Charpy specimens, number in brackets indicate number of splits seen on the fracture surface (77).

Table 1.6. Properties of steels in the Mintz et al. (77) investigation.

Steel	% reduction	Aspect ratio	Max. No. of fissures	Grain size, μm(45°)	Lowest energy value for 100% ductile failure	50%FATT, °C	36 J ITT, °C	LYS, MPa	UTS, MPa
C/Mn	0	1·23	0·5	9·6	142	−90	−93	360	457
	10	1·76	2	9·1	83	−77	−76	454	533
	20	2·45	2	8·0	83	−75	−73	480	554
	40	3·80	4·5	7·4	20	−120	−75	557	615
C/Mn/Nb	0	1·51	0·5	8·4	75	−63	−60	434	510
	10	1·55	1	7·8	60	−63	−60	532	593
	20	2·54	2	6·9	45	−47	−42	563	600
	40	3·25	3	6·2	37	−90	−73	647	695

1.12.5. **Role of Banded Microstructure**

Banded microstructures have been reported by a number of authors (74, 75, 78, 85, 94, 95) as having an effect on the formation of splits. Recent work carried out by Joo et al. (78) on API-X80 grade steel found that, although numerous features could be attributed to the formation of splits such as texture, intergranular cleavage along austenite boundaries, segregation of P

and S, anisotropy of microstructure banding and aligned particles, the most dominant factor in the study was considered to be the microstructural banding, see Figure 1.55. It can be seen from Figure 1.55 that the splits seem to propagate between a region of coarse ferrite grains and a finer region richer in harder phases (pearlite, bainite and MA constituent (mixture of martensite and retained austenite)). This might be expected due to the mechanical incompatibilities that exist between these two bands. Texture was also thought to play a role with a significant difference in texture being observed in the coarse compared to the fine grain patches.

Schofield et al. (85) found that, for high strength steel used for pipe line, arrow head markings formed on the fracture surface of DWTT and splits formed on Charpy fracture surfaces. The cause for this was the material anisotropy with coarse-grained regions lying parallel to the plate surface, as well as a preferred (100) [011] texture and elongated non-metallic inclusions (mainly MnS). The difference in the Charpy ITT values between the WR and TR orientation samples (see Figure 1.56 for specimen orientation for the Schofield et al. (85) data), was 70 - 80 °C whereas the difference was only 20 °C between these two orientations when the steel was normalised. As the coarse grained regions lie parallel to the plate surface, it was assumed that they provided an easy pathway for split formation in the WR plane, whereas in the TR plane the splits would have to pass though both coarse and fine grained patches.

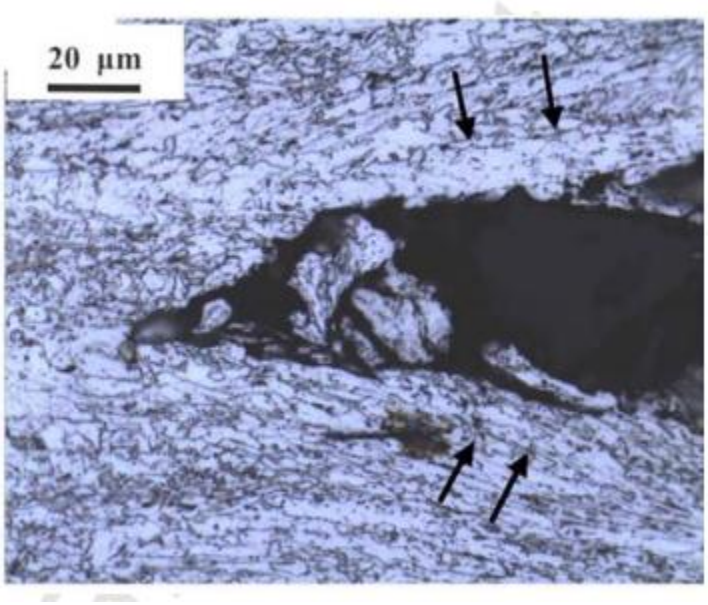

Figure 1.55. Micrograph showing a split going through coarse grain size patches, with the arrows indicating the microstructural banding (78).

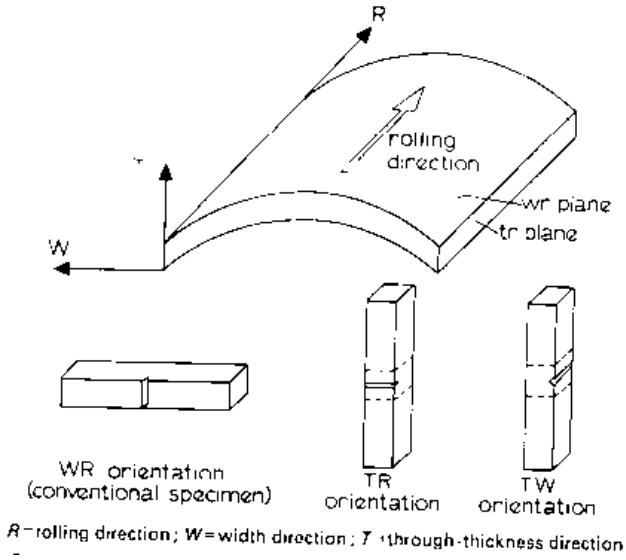

Figure 1.56. Specimen orientation for Schofield et al. (85) study.

1.12.6. **Role of specimen orientation (longitudinal and transverse specimens)**

Morrison (83) states that in a wrought steel the mechanical properties differ when measured in different orientations due to the material's anisotropy, which is influenced mainly by inclusions (with their shape playing great importance), as well as segregation and banding of the microstructure along with grain elongation. It was stated that the higher the amount of

deformation the greater the amount of anisotropy. Bramfitt and Marder (79) compared the difference in energy absorbed, for samples with a similar number of splits formed for longitudinal and transverse specimens and they found that the amount of energy absorbed decreased with an increasing number of splits for samples tested in both the transverse and longitudinal orientations, shown in Figure 1.57. From this graph it would seem that the longitudinal samples absorb a higher energy, when a similar number of splits are present on the fracture surface, than the transverse samples. The solid line of the graph represents Equation 1.13 (79), where E_o is the energy absorbed for an un-split, full size Charpy specimen (10 mm), N is number of splits and the term N+1 represents the number of sub size specimens created by the splits.

E = Absorbed Energy = $\frac{E_0}{(N+1)}$ Equation 1.13

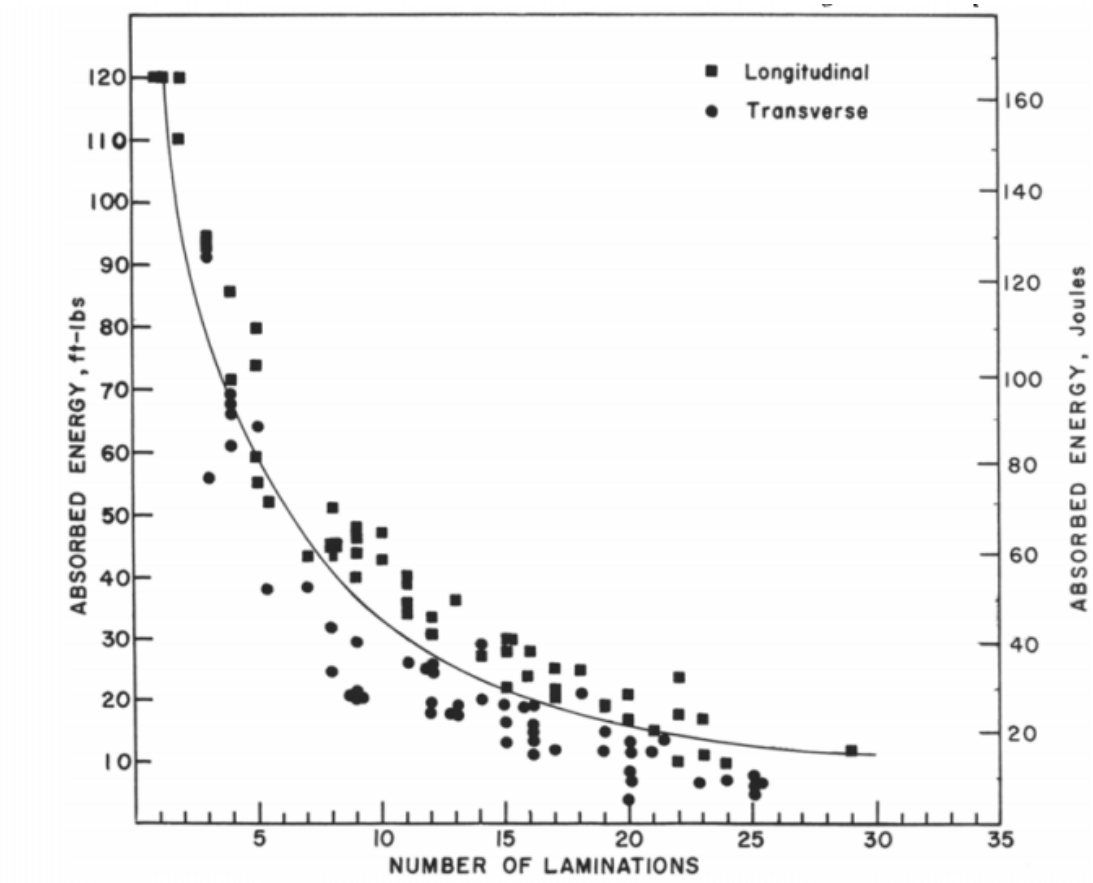

Figure 1.57. Number of splits with Charpy energy absorbed for longitudinal and transverse specimens, for all temperatures when splits formed (79).

The fact that longitudinal specimens produce a higher upper shelf value (46) and lower DBTT was also shown by Baldi and Buzzichelli (73), Figure 1.58. They also noted that the splits observed for samples tested in the longitudinal were more predominate (i.e. deeper, longer, thicker) than those observed on samples tested in the transverse orientation.

Mintz and Morrison (75) found, that for X65 controlled rolled steels, longitudinal specimens had a ~20 ^{0}C lower ITT when compared to the transverse orientation and contained more splits. The longitudinal specimens contained between one and four splits, depending on the rolling reduction, with the transverse specimens containing fewer splits and the normalised specimens (both orientations) containing no splits. The main factor influencing the formation

of these splits was found to be grain elongation, which explains the difference between the longitudinal and transverse orientations. The longitudinal orientation samples showed more elongated grains than the grains in the transverse orientation, with aspect ratios of 1.71 for the specimen with ~ 4 splits and 1.55 for specimens with around ~1 split. The aspect ratio was measured in the longitudinal / through thickness orientation. In the normalised steels no splits were seen with aspect ratio values of ~ 1.

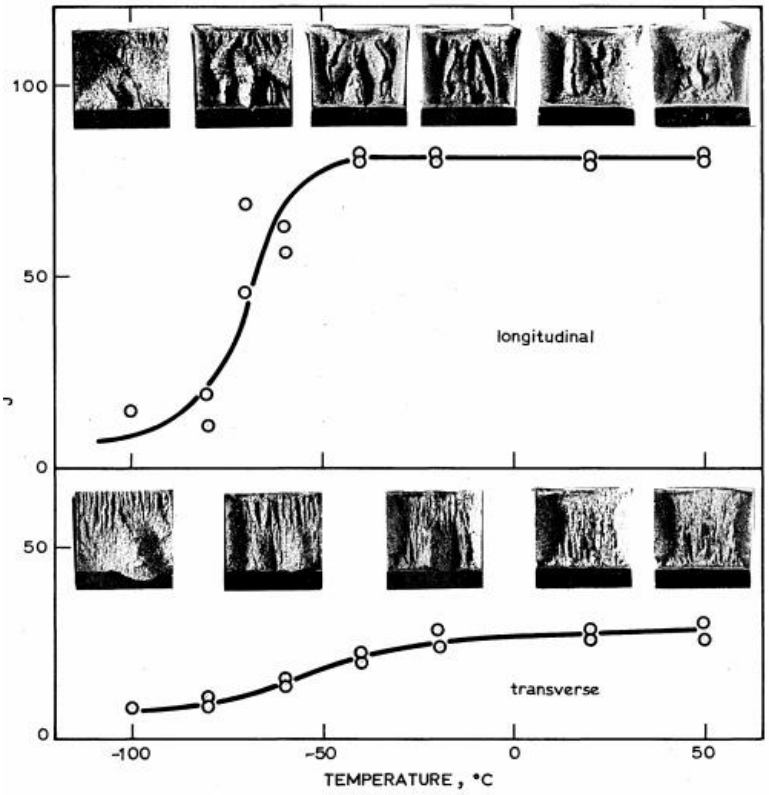

Figure 1.58. ITT curves for longitudinal and transverse Charpy specimens for a HSLA steel (73).

1.12.7. **Role of yield stress**

The yield stress affects the stress developed during loading under a blunt notch, as an increase in yield stress decreases the plastic zone size, which increases the stress in the plastic zone. The steel strength is an important factor when looking at the influence of splits on the Charpy toughness, as it controls the through thickness stress acting on the grain surfaces. An

increase in yield stress makes the steel more susceptible to the formation of splits (77). As the test temperature increases the yield stress decreases, making it more difficult to open up the split cracks, as well as reducing the number of splits that forms. This leads to an increase in the ductile upper shelf energy as temperature is increased (76). A prerequisite for split formation is a high yield stress which allows for a high level of constraint to be attained (85).

The yield stress in the transverse orientation tends to be higher than in the longitudinal orientation; Mintz et al. (76) found this to be ~ 25 MPa higher, which was attributed to texture, resulting in a slightly lower T_3. When the temperature is increased in Charpy testing, the yield stress decreases, which makes it difficult to open up the cracks reducing the number of splits, leading to a gradual recovery in the ductile shelf energy temperature. This would mean one of the reasons why it is harder for the splits to form in the transverse orientation is due to the higher yield stress.

1.13. **Summary of literature**

High strength strip steels (yield strength approx 700 MPa) can achieve their high strength through a combination of a fine ferrite grain size and strengthening precipitates. They are controlled rolled and splits are commonly observed on the fracture surfaces during Charpy impact testing in the ductile to brittle transition region for both longitudinal and transverse orientations. These steels can contain coarse TiN inclusions, which have been reported in other steels to initiate cleavage cracking, particularly in coarse grain sized steels. However, one paper in the literature indicated that whilst coarse TiN particles had been observed to initiate cleavage in the steels examined, they had no significant effect on the Charpy DBTT values (for ferrite grain sizes in the range 5 – 28.4 μm).

It has been well documented in the literature that splits on the fracture surface of Charpy specimens lower the ITT as well as the upper shelf energy. Splits lower the ITT because they promote plane stress instead of plane strain below the notch, and result in the Charpy sample behaving as a group of thinner samples rather than one thick sample. In the literature there are a number of different mechanisms proposed for the formation of these splits. In this project the cause, and effect, of splits formed during Charpy impact testing of high strength strip steels has been investigated. In particular the reason for differences in Charpy toughness for strip steels hot rolled to different thicknesses has been examined, along with the effect of test orientation. Particular focus was given to the mechanism for split crack formation and propagation in these steels.

1.14. **Aims and Objectives**

Tata Steel currently produces a high strength strip steel at a thickness of 8 mm with a yield stress of ~700 MPa for the yellow goods market (earth moving equipment), for parts such as booms on cranes. Customers are now requesting thicker strips of the same grade, allowing the earth movers to increase the loads they can move. To meet this request Tata Steel has produced three experimental compositions to a range of thicknesses, 10 - 17 mm, matching the required yield strength of ~700 MPa. Although these steels meet the yield stress target they do not meet the toughness specification (Charpy value of 27 J at -40 °C), with specimens showing considerable scatter in Charpy impact values, with the thicker strip producing the worst toughness values. These high strength strip steels show splits on the fracture surfaces from samples in the transition range particularly at the upper transition temperature from Charpy impact testing, and it is believed that these affect the toughness properties in the different thickness strips as well as in different test orientations.

This study aims to characterise the microstructure, and identify the factors affecting the Charpy impact toughness, in thick (10-16 mm) high strength steel strip steels. In particular the work will consider the reasons for the formation of splits in the different thickness strips, and the effect they have on the ITT. The specific objectives for the project are:

Objectives

- To characterise the microstructure (grain size distributions, grain shape phase balance, coarsest cementite particles, crystallographic texture) and mechanical properties (tensile, Charpy impact and hardness) for three strip steel compositions and three thickness conditions.

- To characterise any inclusions present in the steels, in particular to identify the role of coarse TiN particles on toughness.
- To characterise the size and number of split cracks on the fracture surface of Charpy impact samples and to identify the origin of the splits. In addition to determine if there is a relationship between the number and severity of the split cracks with the different sample thicknesses and specimen orientations.
- To understand how, and under what impact energy, the split cracks form, using techniques such as tomography, acoustic emission testing and low energy Charpy testing.
- To relate the Charpy impact toughness of high strength strip steels, of different thicknesses and tested in different orientations, to the materials microstructure.

2. MATERIALS, PROCESSING AND EXPERIMENTAL PROCEDURE

2.1. **Materials Studied**

The three different experimental compositions provided by Tata Steel UK (MAC, MAD and MAE), and another, titled Steel X, are given in Table 2.1. MAC, MAD and MAE are trial steel compositions rolled to a range of thicknesses between 10 and 17 mm. The main composition differences between the trials are that MAC contains less Ni than MAD and MAE. Ni is added as it is known to increase toughness; however it can also reduce the surface quality during processing due to the formation of an oxide layer which cannot be easily removed by the descaling process. MAC contains more Cr but less Mo that MAD and MAE, which will affect the hardenability and fine scale precipitation. MAE contains less Ti, which may affect the number density of coarse (>1μm) TiN particles that are present and the precipitation strengthening from fine scale Ti-rich precipitates that form during coiling. Table 2.2 gives details of the different strip thicknesses provided; all samples were provided from the middle of the coils.

Table 2.1. Strip composition in wt % and ppm(*) for strip samples provided.

	N*	**Al**	**B***	**C**	**Ca***	**Cr**	**Cu**	**Mn**	**Mo**	**Nb**	**Ni**	**P**	**S**	**Si**	**Sn**	**Ti**	**V**
MAC	48	0.035	<2	0.057	17	0.596	0.014	1.654	0.019	0.064	0.370	0.010	0.004	0.102	<0.002	0.082	0.007
MAD	49	0.041	<2	0.063	27	0.021	0.013	1.61	0.105	0.066	0.974	0.010	0.004	0.097	<0.002	0.089	0.007
MAE	56	0.041	<2	0.059	23	0.015	0.013	1.62	0.182	0.068	0.951	0.009	0.004	0.096	<0.002	0.066	0.007
Steel X	50	0.038	3	0.049	23	0.389	0.010	1.89	0.006	0.079	0.255	0.014	0.002	0.326	0.002	0.102	0.011

Table 2.2. Specimens available and thickness

Code	Grade	Thickness (mm)
A	MAC	10
B	MAD	10
C	MAE	10
D	MAC	11.8
E	MAC	11.6
F	MAD	13.2
G	MAE	13.2
H	MAE	13.1
J	MAE	16.4
K	MAD	16.8
L	MAD	15.5

2.2. **Material Processing**

The as-cast slabs were reheated to between 1200 and 1250 °C then rolled in a roughing mill from a thickness of 230 mm to 35 – 40 mm. The strip then entered the finishing line of 5 - 6 stands, depending on the final thickness required, at around ~ 1000 °C. The finishing rolling temperature was ~ 900 – 950 °C, and then the strip was cooled by water sprays to approximately 650 °C before coiling. Steels MAC, MAD and MAE were all rolled to the same nominal rolling schedule for the same thickness strip, with the ≤ 12 mm strip passing through 6 finishing stands whilst the ≥13 mm strip was rolled using 5 finishing stands.

2.3. **Experimental Techniques**

2.3.1. **Optical microscopy and image analysis**

Longitudinal and transverse samples from each strip were mounted in Bakelite, ground, polished and etched in 2% nital, Figure 2.1. The samples were characterised using a Zeiss Axioskop-2 microscope with Axiovision 4.6.3 and KS 400 image capture and analysis software. The microstructure was characterised by the average grain size (equivalent circle diameter, ECD) for around 7000 grains. Inclusions and amount of second phase were also measured (number density, average size (TiN by max edge length), area fraction) by this method for around 20 fields using at 50x objective.

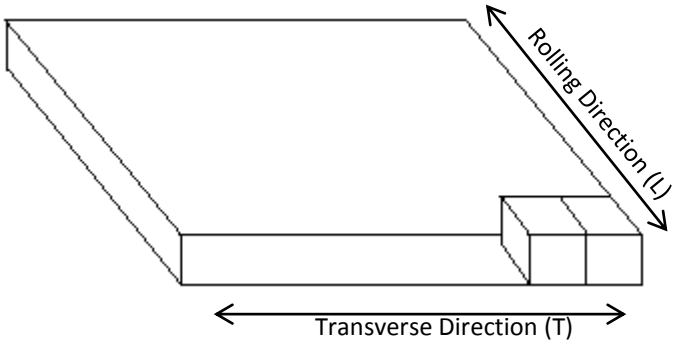

Figure 2.1. Diagram showing the orientation of the samples

2.3.2. **Scanning Electron Microscopy (SEM) Analysis**

SEM analysis was carried out on fracture surfaces as well as mounted, ground, polished and etched samples. A Jeol 6060 was used, operating at 20 kV, with a working distance of ~10 mm. The Jeol 6060 SEM was equipped with an energy dispersive X-ray spectroscopy system (EDX) which was used to determine the composition of inclusions present in the steel. Carbide thickness measurements (average of largest 15 seen for each composition or until numbers were consistent) and inclusion characterisation (composition content) were also carried out using the SEM on as polished and etched samples.

2.3.3. **Electron Backscattered Diffraction (EBSD)**

EBSD was carried using a Jeol JSM-7000F field emission gun scanning electron microscope (FEG-SEM) at UoB and FEI Quanta 600 at Tata Steel, to determine grain size and the general and local texture in the strip samples. Samples were polished with 1 µm diamond and etched using 2% nital solution. This process was repeated six times, before a final polish with 0.05 micron colloidal silica but without etching. EBSD was carried out at two locations each sample, at ¼ and ¾ depth below an arbitrarily chosen tip surface. Each scan area was 200 x 250 µm and was collected at 0.5 µm steps. Grain size information was set for 2°, 5°, 10° and 15° boundary angles. Orientation distribution functions (ODF) were carried out at Tata Steel only, using an ODF slice for each area scanned, with the grain boundary angle set at 5°.

2.3.4. **Thermodynamic modelling**

Thermo-Calc (version S) can be used to predict the equilibrium phase balance, precipitate formation temperatures, transformation temperatures and the phase compositions between 600 and 1700 ^{0}C. For this work it was used in predicting formation of TiN. It has been reported by Zhang (50) that thermodynamic predictions by Thermo-Calc correlated well with experimental results when predicting coarse TiN. Data input into the software included the composition of steel, and pressure (constant at 101325 N/m^2) for a total of 1 mole of material. The TC-Fe7 steel database was used for this study, with results only as good as the data stored within the Thermo-Calc database.

2.3.5. **Hardness testing**

Macro hardness measurements were carried out using an Indentec Vickers hardness testing machine with a 20 kg load. Indents were made through the sample thickness with the average

hardness determined from at least three indents. Hardness tests were carried out on specimens which had been mounted and polished as in section 2.3.1.

2.3.6. **Impact testing**

Charpy impact testing was carried out using a calibrated Instron Charpy machine, on standard specimens according to standard ASTM E23, to produce a Charpy impact energy graph. Standard specimens of size of 10 x 10 x 55 mm with a 2 mm deep notch with a 0.25 mm root radius (45° notch) were used. 90° notches were used to generate a larger plastic zone size when investigating the effects of TiN inclusions on Charpy impact toughness in order to increase the probability of a large TiN inclusion being sampled, shown in section 4.1.

Specimens were tested in the longitudinal and transverse orientations (Figure 2.2), at temperatures between -180 °C and 90 °C. Temperatures were achieved by immersing specimens in a mixture of liquid nitrogen and ethanol (-80 to -20 °C), ice water (0°C) and hot/boiling water (over 20 °C), with the temperatures measured using a thermocouple to within ± 1 °C of the test temperature required. Specimens were held for 5 minutes at test temperature, along with the tongs used to place the specimen in the Charpy machine, with the transfer to the Charpy machine being within 5 seconds. After the Charpy test, specimens were washed in ethanol and placed in a desiccator ready for SEM analysis.

Tata Steel carried out three tests at five different temperatures for each strip steel composition, thicknesses and orientation (i.e. the MAD steel composition at 10 mm thickness, was tested using 15 specimens in the longitudinal orientation and 15 specimens in the transverse orientation). Charpy tests (low blow and full energy) were also carried out at

the UoB for the MAD steel composition of 10 and 16.8 mm thickness in the longitudinal and transverse orientation.

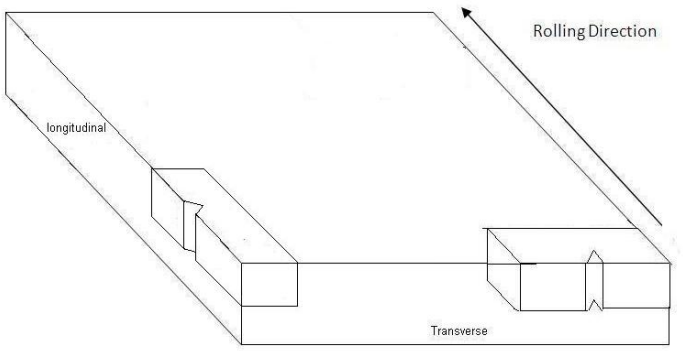

Figure 2.2. Orientation of Charpy specimens

Low blow Charpy tests were carried out at the UoB to determine the initiation energy for split formation. Low blow Charpy impact tests were carried out using an initial 20, 40, 60, 80 and 100 J impact energy, at room temperature, which corresponds to the upper transition region of the steels examined where pronounced splits were observed on the fracture surface. Low blow tests were carried out by raising the Charpy impact hammer to the desired impact energy i.e. 20, 40, 60 or 80 J.

Tata Steel Charpy results were plotted and the average from each temperature test was used to plot the Charpy curve. The curve was then re-plotted as a *tan*(h) function curve (96), using the non-linear regression (Equation 2.1). The root mean square (RMS) values were also fitted to the Tata Charpy curves. This was done by finding the difference between the *tan*(h) curve and the experimental data points, taking the square of all the numbers in the set, finding the mean of the squares, and then taking the square root of the result.

$$A + B\tanh\left(\frac{T - T_0}{C}\right)$$

Equation 2.1

Where, A and B are constants (A+B equals the upper shelf temperatures and A–B equals the lower shelf temperature). T is the dependent variable of test temperature, T_0 is a constant defining the position of the curve along the temperature axis, and C is a constant defining the slope of the curve in the transition region.

2.3.7. **Acoustic Emissions (AE) testing**

AE monitoring was used during the low blow Charpy tests with a broadband frequency piezoelectric crystal sensor linked to an acoustic acquisition station produced by Physical Acoustics Corporation (USA) (97). The sensor was connected to the specimen using a paraffin gel to achieve good coupling and signal output; this necessitated the tests being carried out at room temperature, Figure 2.3.

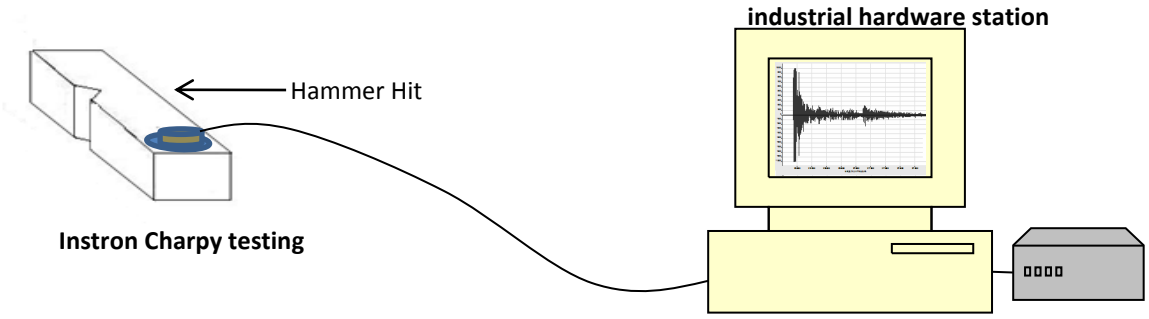

Figure 2.3. Representation of acoustic emission set-up on a Charpy Specimen.

2.3.8. **X-ray tomography and Matlab image reconstruction**

The unbroken low blow Charpy impact specimens were analysed using X-ray tomography to determine if split cracks were present. X-ray tomography was carried out using a SkyScan1172 MicroCT System and CTAn software, using hardware version D. The source voltage was set to 100 kV, and the current 100 μA, with a camera pixel size of 9 μm and

image pixel size of 4.35 µm. An Al+Cu filter was used when carrying out the procedure. Once the X-ray tomography slices were produced, the co-ordinates were then manually recorded for a variety of slices. These co-ordinates were used as inputs into a Matlab model 2010a (code for model in Appendix 10.1), to produce a 3D reconstruction of the split.

2.3.9. **Split Characterisation**

Splits were characterised by the length, depth and width as shown in Figure 1.36. Measurements were taken in identical ways. For fully fractured specimens, specimens were cut halfway through the specimen (not including notch), to measure the width and depth, shown in Figure 2.4. Low blow measurements were taken from the halfway point of a split, as shown in Figure 2.4. All splits were measured as described for one specimen per temperature for MAD samples in the longitudinal and transverse orientation at thicknesses of 10 and 16.8 mm.

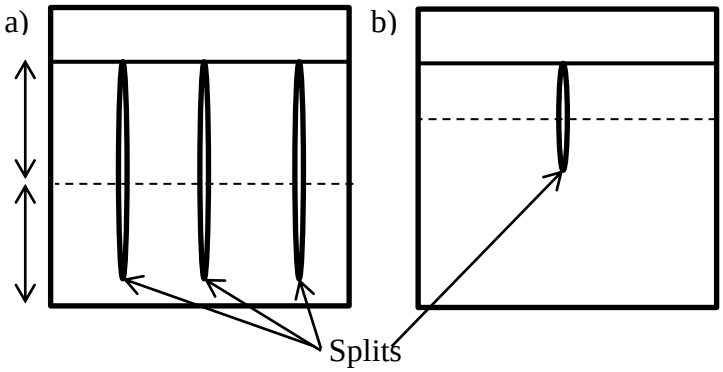

Figure 2.4. Schematic showing the sectioning position for Charpy specimens for the length, depth and width of splits. Dashed line indicates sectioning position, a) full blow Charpy specimens and b) low blow Charpy specimens.

3. CHARACTERISATION OF AS-RECEIVED STRIPS

High strength strip steel meeting requirements of ~700 MPa yield strength and 27 J Charpy V notch impact energy at -40 °C, can be produced at 8 mm thickness, but it is difficult to achieve these properties at higher thicknesses. This chapter covers the microstructure and mechanical property characterisation for a series of as-received strip samples with thicknesses between 10 and 16.8 mm for the 3 different compositions MAC, MAD and MAE.

3.1. **Mechanical properties**

The yield stress and tensile strength values for the as-received strip samples are given in Table 3.1 for samples in the longitudinal and transverse orientations. It can be seen that MAE has consistently lower yield stress and tensile strength values compared to MAC and MAD at similar strip thicknesses, with the strength values decreasing as the thickness increases. The transverse specimens have higher strength (yield and tensile) values than the longitudinal specimens; this is typical for rolled product (73) and is consistent with the more elongated grain shapes experienced in the longitudinal orientation. Elongated grains give a greater mean free path between boundaries than equiaxed grains resulting in higher stress intensification at the head of any dislocation pile-ups so that less external stress is needed to overcome the critical resolved shear stress and initiate yielding beyond the first grain in the longitudinal orientation.

Table 3.1. Yield and tensile properties of as-received strip steels (data from Tata Steel U.K Limited, apart from hardness data which were determined at the University of Birmingham (UoB).

Sample	Thickness (mm)	Long Yield Stress (MPa)	Long Tensile Strength (MPa)	Tran Yield Stress (MPa)	Tran Tensile Strength (MPa)	HV 20
MAC A	10	710	802	794	828	281 ±13
MAD B	10	726	830	805	839	284 ±6.5
MAE C	10	689	783	806	826	285 ±6.8
MAE G	13.2	655	754	731	783	255 ±9.3
MAE J	16.4	672	777	754	807	279 ±13.2
MAD K	16.8	685	787	758	812	285 ±11
MAD L	15.5	686	783	740	793	281 ±13.4

3.2. **Hardness**

Hardness values are shown in Figure 3.1 and Figure 3.2 and the average value is given in Table 3.1. MAE consistently has the lowest yield stress when compared to similar thick strips, although significant scatter seems to be present. When considering the hardness results, a similar pattern is expected as shown with the yield stress i.e. MAE having the lowest yield stresses. This trend is not consistent with the hardness values, with hardness values being similar for all specimens falling within the scatter band of the results.

Hardness results indicated that all materials are softest along the centre-line for all thicknesses. The variation in the hardness values could be explained if the region below the surfaces is strained more than the middle of the strip, which would lead to a greater amount of work hardening on the surface of the strip. Overall, there are no consistent significant

differences between the compositions and thicknesses studied, with most sub-surface hardness values being in the range 280 – 300 HV falling to 260 - 280 HV at the centre.

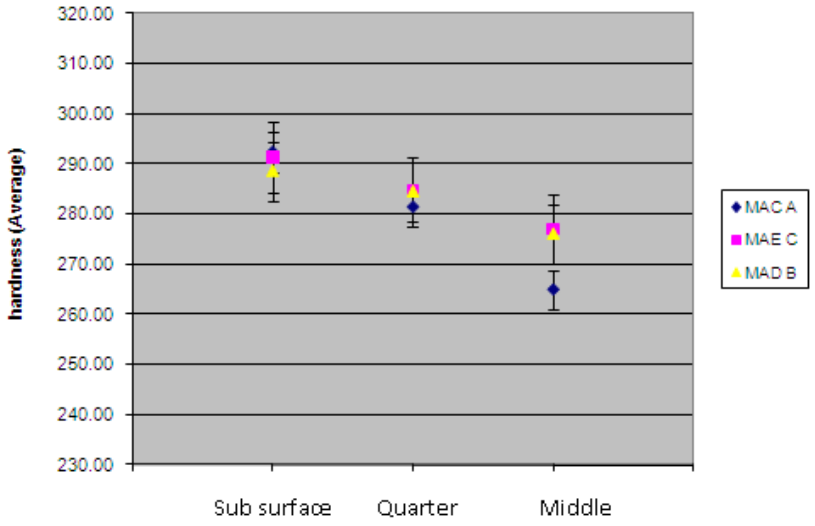

Figure 3.1. Hardness results for 10 mm thickness strip samples.

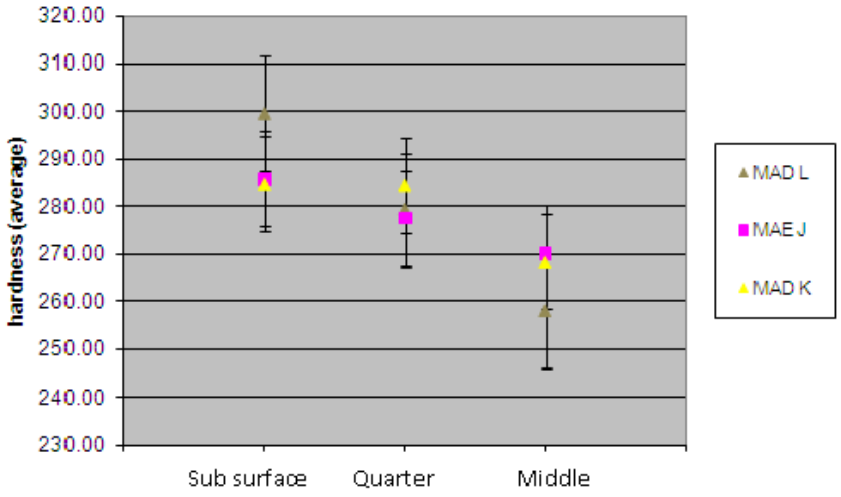

Figure 3.2. Hardness results for MAD 16.8 mm (K) and 15.5 mm (L), and MAE 16.4 (J) thick strip samples.

3.3. **Microstructure**

The microstructure is similar for all compositions, consisting of polygonal ferrite grains with a small amount of 2nd phase (pearlite / bainite), less than 1 %, grain boundary carbides and inclusions such as MnS, TiN and Al_2O_3 (identified by EDX), Figure 3.3 and Figure 3.4. It can

be seen from Figure 3.5 and Figure 3.6 that there are bands of coarse and fine grain-sized ferrite in the microstructure. The proportion of coarse grain-sized ferrite is quantified in Table 3.2, and the effect of coarse patches on splits in section 5.2. The thicker strip has a slighter larger average grain size, which is shown in Figure 3.6 and Table 3.2. The grain size does not differ significantly for the different grades at similar thicknesses. Figure 3.4 shows the variety of inclusions present in the steels.

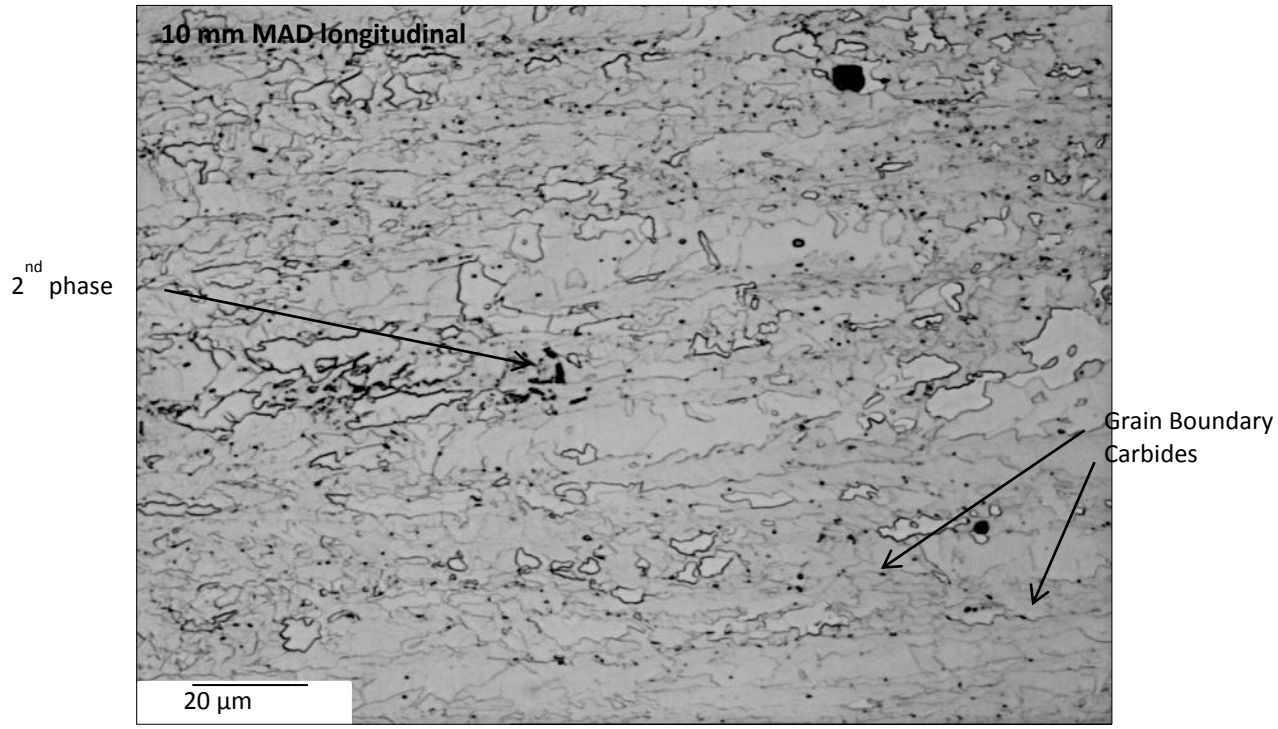

Figure 3.3. Micrograph of MAD 10 mm thick strip, longitudinal section showing 2nd phase.

Table 3.2. Grain size for the four different strip grades investigated at the different thicknesses, where L is the longitudinal orientation and T the transverse orientation.

Sample	Thickness (mm)	Direction	Grain size (μm)	% coarse grains
A- MAC	10	L	4.40	15
B- MAD	10	L	4.33	11
C- MAE	10	L	4.70	12
G- MAE	13.2	L	4.65	34
J- MAE	16.4	L	4.64	39
K- MAD	16.8	L	4.99	42
K- MAD	16.8	T	5.13	50
B- MAD	10	T	3.47	15

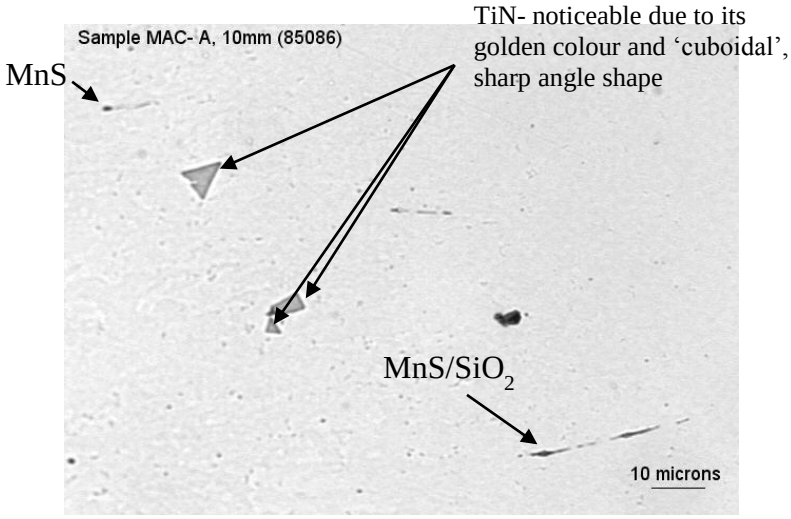

Figure 3.4. Micrograph of an un-etched MAC A specimens, showing typical inclusions present in the steel.

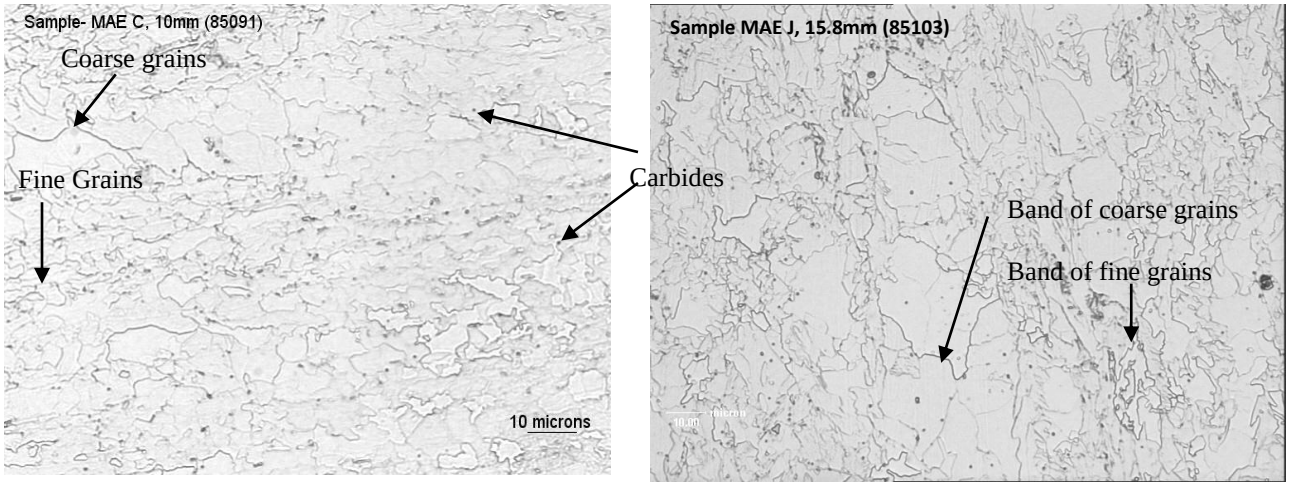

Figure 3.5. Micrographs of composition MAE (10 mm, B and 16.4 mm J) showing microstructure.

Figure 3.6 contains micrographs of the 10 mm strip in the transverse and longitudinal orientation a, b respectively and the 16.8 mm strip transverse and longitudinal, c and d respectively. It can be see that coarse grain-sized patches are present in all specimens with coarser patches being observed in the thicker strips. It can also be seen that grains are more elongated in the longitudinal specimens than in the transverse specimens.

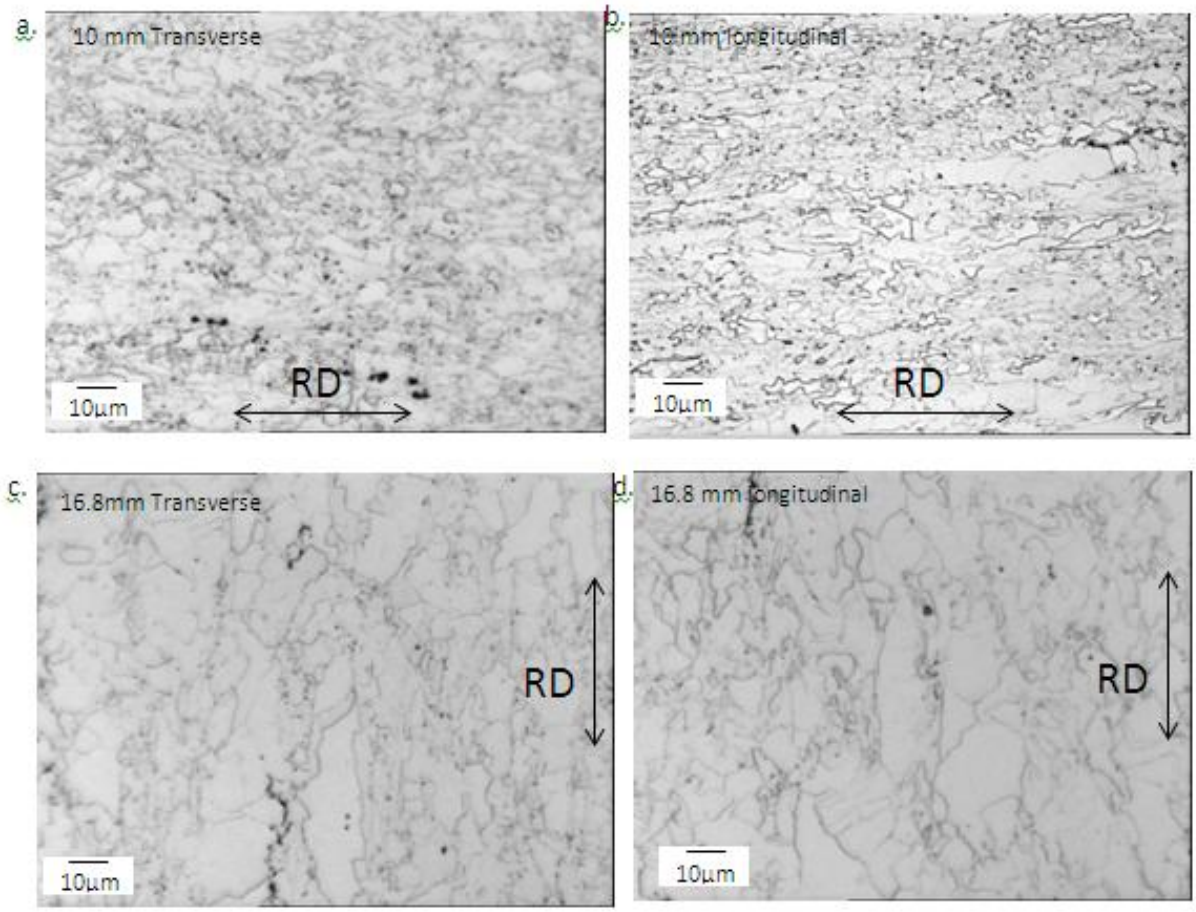

Figure 3.6. Micrographs of composition MAD showing the microstructures, a) 10 mm transverse, b) 10 mm longitudinal, c) 16.8 mm transverse, b) 16.8 mm longitudinal . RD and arrow- indicates the rolling direction.

The results in Table 3.3 are based on area % values apart from the average grain size, which is number based. The ferrite grain size distributions (based on area %) are shown in Figure 3.7 and Figure 3.8. It can be seen that the distributions generally show log-normal shapes that are skewed to larger grain sizes. The microstructural observation of coarse and fine grain patches is not clearly seen in the distributions, although MAE at 13.2 mm (G) and 16.4 mm (J) thicknesses do show a small amount of bimodality (as shown by the peaks in the distributions at larger grain size, indicated by arrows in Figure 3.7).

The ferrite grain size distributions for the 10 mm thickness strips for all three compositions (Figure 3.8), exhibit the same log normal shape, with a slight 2nd peak observed for the coarse grains, at similar values to those in the thicker strip grain distributions.

Table 3.3. Ferrite grain size quantitative data

Sample	Code	Thickness (mm)	Average grain size ECD (µm)	Mode (µm)	Coarsest (µm)
3MAC	9PH8A	10	4.40	5-6	19-20
3MAD	9PH8B	10	4.33	5-6	20-21
3MAE	9PH8C	10	4.70	6-7	20-21
3MAE	9PH8G	13.2	4.65	5-6	20-21
3MAE	9PH8J	16.4	4.64	5-6	21-22
3MAD	9PH8K	16.8	4.99	5-6	25-26

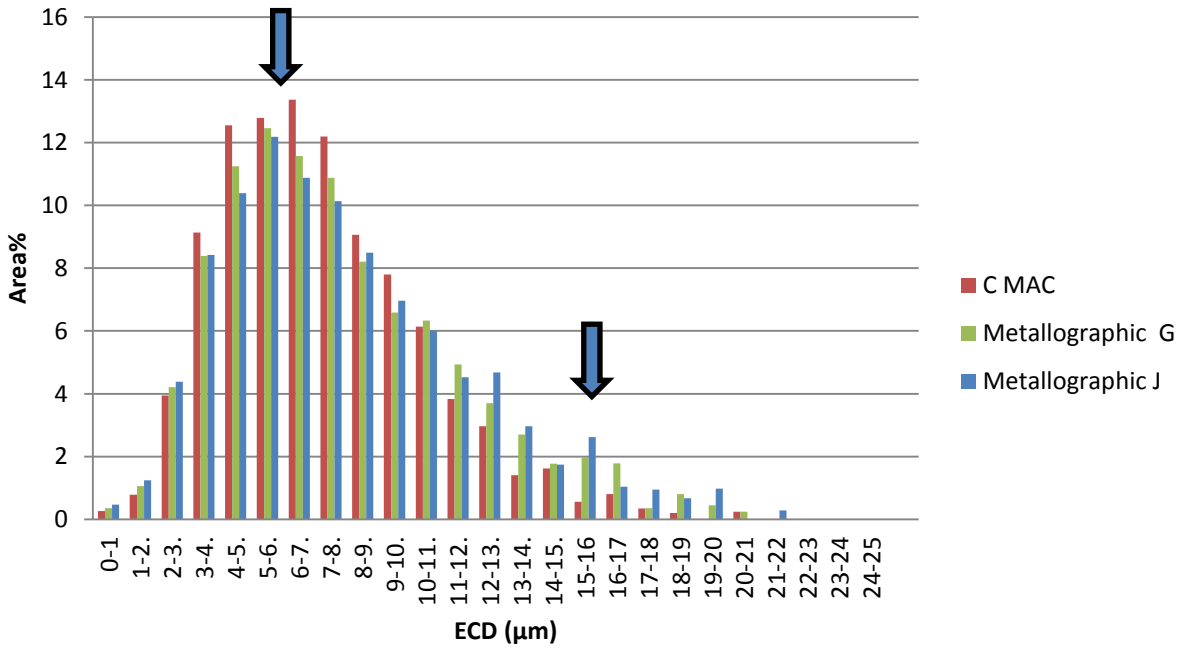

Figure 3.7. Grain size distribution (area %) for composition MAE at 10 mm (C), 13.2 mm (G) and 16.4 mm (J) thickness

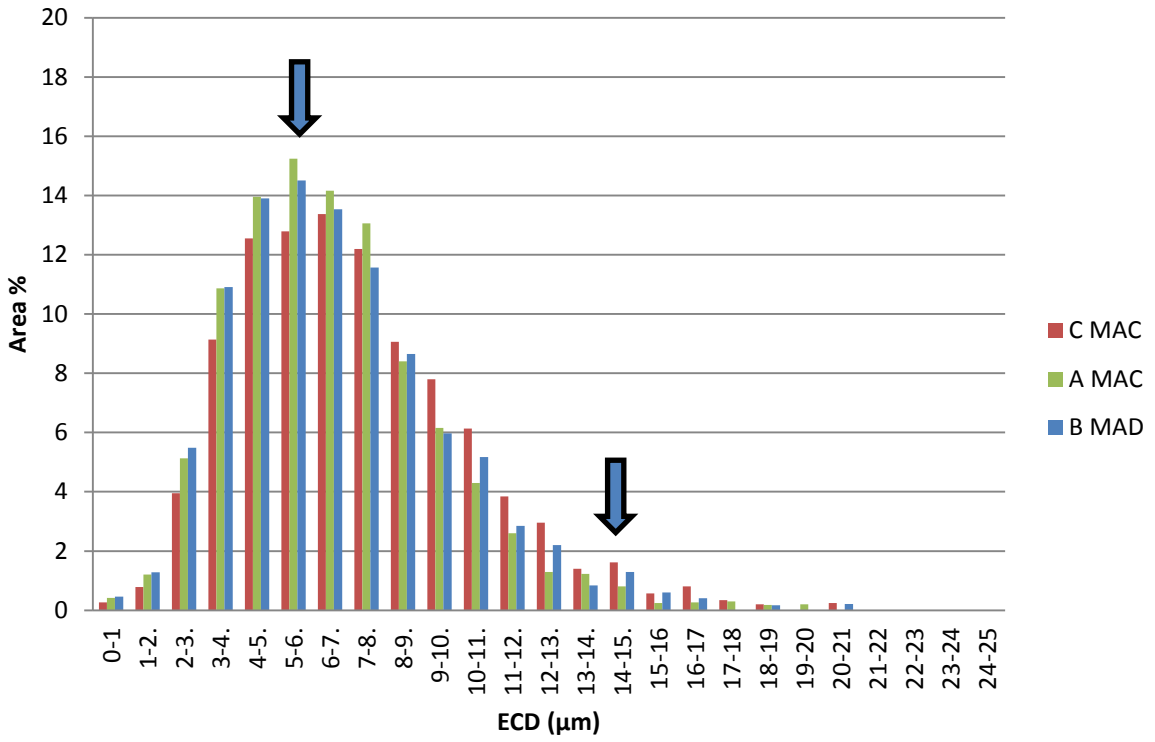

Figure 3.8. Grain size distribution (area %) for compositions MAC, MAD and MAE at 10 mm thickness

3.3.1. **Contributions to yield stress**

Table 3.4 summarises the contributions that grain size, solid solution, precipitation and work hardening (derived) make to yield stress for the steels studied, based on the compositions and microstructures determined above in section 1.5.2. The contributions to yield stress are shown for sample B and K in the transverse orientation, with transverse specimens having higher yield stresses.

Table 3.4. Summary of contributions to yield stress

Sample	Thickness (mm) and orientation	Average grain size (μm)	$d^{-1/2}$ ($mm^{-1/2}$)	Yield stress (MPa)	σ_{ss} (MPa)	$\sigma_{0\ gs}$ (MPa)	Work hardening and precipitation (MPa)
A-MAC	10 Long	4.40	15.1	710	50	196	464
B- MAD	10 Long	4.33	15.2	726	67	198	461
C- MAE	10 Long	4.70	14.6	689	68	190	431
K-MAD	16.8 Long	4.99	14	685	67	182	436
B- MAD	10 Tran	3.47	16.9	805	67	199	539
K-MAD	16.8 Tran	5.13	14	812	67	182	563

3.3.2. **EBSD**

Data provided by Tata Steel (Table 3.5) show that there is a difference in the measured EBSD grain size as the grain boundary mis-orientation threshold settings change. Table 3.5 and Table 3.6 compare the EBSD measurements made at Tata Steel and the University; both show an increase in grain size as the threshold boundary mis-orientation increases from 2 to 15°, which indicates that there is a proportion of low angle boundaries present in the steel affecting the apparent number average grain size. The number average grain size (University measurements) increases by ~35% as the threshold mis-orientation angle is raised from 2^0 to 15^0; a similar increase was also seen by Tata Steel (Table 3.5) for C - MAE at 10 mm thickness (~40 %). For this steel composition and thickness there is some difference between Tata Steel and UoB values at the different mis-orientation thresholds, but agreement is good for a threshold of 15°. Table 3.5 also indicates that, for the thicker (16.4 / 16.8 mm J and K respectively) strips the same variation in threshold resulted in a ~ 50% increase in number average grain size. The average grain sizes determined by EBSD are smaller than those

measured by optical metallography, Table 3.3, suggesting that some low angle boundaries are not being clearly identified by etching.

Table 3.5. EBSD grain size (μm) data for samples (data from Tata Steel U.K Limited)

Sample	Thickness (mm)	2 Deg	5 Deg	10 Deg	15 Deg
A-MAC	10	2.14	2.49	2.74	2.90
B-MAD	10	1.84	2.31	2.60	2.73
C-MAE	10	2.02	2.35	2.64	2.84
G-MAE	13.2	2.29	2.82	3.19	3.42
J-MAE	16.4	2.40	3.40	3.48	3.65
K-MAD	16.8	2.90	3.50	4.00	4.34

Table 3.6. EBSD grain size data for MAE 10 mm thick strip (UoB data)

University	2 Deg	5 Deg	10 Deg	15 Deg
Average	2.09 ±0.25	2.48 ±0.27	2.70 ±0.24	2.82 ±0.24

Low angle grain boundaries offer less resistance to crack propagation than high angle ones (Bhattacharjee et al. (41) set the threshold for mesotexture as <15°(40) so that 'grains' separated by lower angle boundaries can act as a larger 'effective' grain). Figure 3.9 shows the effective grains in MAE 10 mm strip as the mis-orientation threshold is increased, where some large effective grains, approaching an ECD of 10 μm, can be seen.

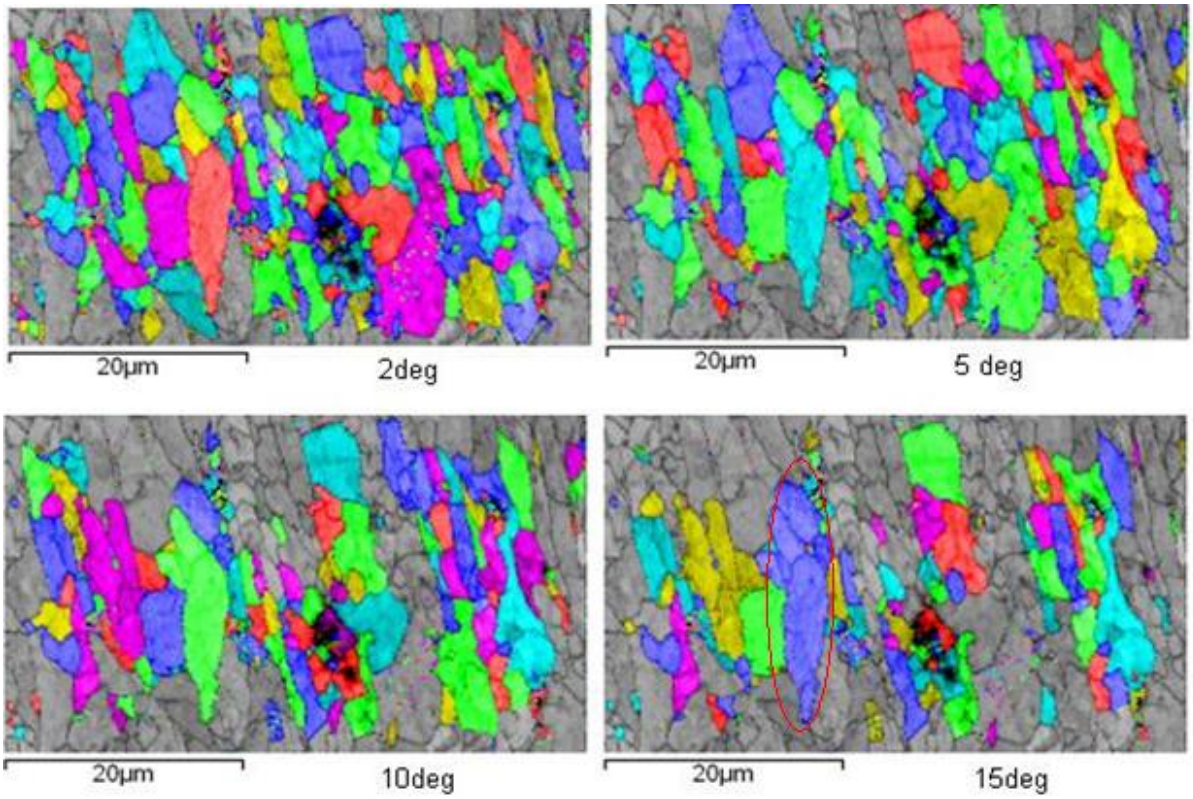

Figure 3.9. EBSD grain maps from MAE 10 mm thick strip for different mis-orientation thresholds, Area outlined bottom right in red, indicates a cluster of grains that merge to form a large ‘effective’ grain (each colour indicates an individual ‘effective’ grain based on the misorientation threshold used).

3.3.3. **TiN**

The presence of TiN particles in the strip steels was identified by their cuboidal shape and golden colour, their identity was confirmed by EDX analysis as shown in Figure 3.10. The size distributions of coarse TiN particles through-thickness for the 10 mm thick strips of MAC, MAD and MAE are summarised in Table 3.7 and Figure 3.11. The size distributions show a skewed unimodal distribution for all three steels with MAE showing the lowest number density and MAD the greatest. In terms of size MAC shows the largest range due to one very large inclusion being observed; if this is excluded then the distributions are largely similar, although MAD shows a greater occurrence of particles in the 6 – 7.5 µm size range.

The TiN inclusions appeared to be clustered and possibly occur in bands when observed at lower magnifications, which would be consistent with the TiN particles forming in or being swept into the solute enriched interdendritic liquid during solidification resulting in an inhomogeneous spatial distribution. The number density values in Table 3.7 agree with the variation in [Ti] for these steels, despite variations in [N]. Looking at the stoichiometry, the [Ti] value is higher then the [N] value. This would suggest that these steels contain excess [N] so that decreasing [Ti] content reduces the formation temperature and hence nucleation rate in the liquid. Earlier studies (50) carried out on steels where the [N] content is less than stoichiometric showed that increased [Ti] did not increase the nucleation rate of TiN, but gave greater growth i.e. a similar number of TiN particles, but larger ones.

Table 3.7 compares the size range of TiN inclusions characterised by feret max. (a measure of maximum side length) values with the majority of TiN being complex inclusions with Al_2O_3 cores and/or Nb(C,N) and MnS also present on their surfaces (Figure 3.10). The thicker strip had a smaller number density of coarse TiN particles, and a slightly smaller average inclusion size but with the particles being present in the same size range as in the thinner strip, the differences seen in number density and average feret max. size between the two thicknesses are consistent with a greater rolling reduction for the thinner strip, and hence greater sampling frequency, as both strips were produced from the same cast material and would be expected to have the same starting coarse TiN distribution.

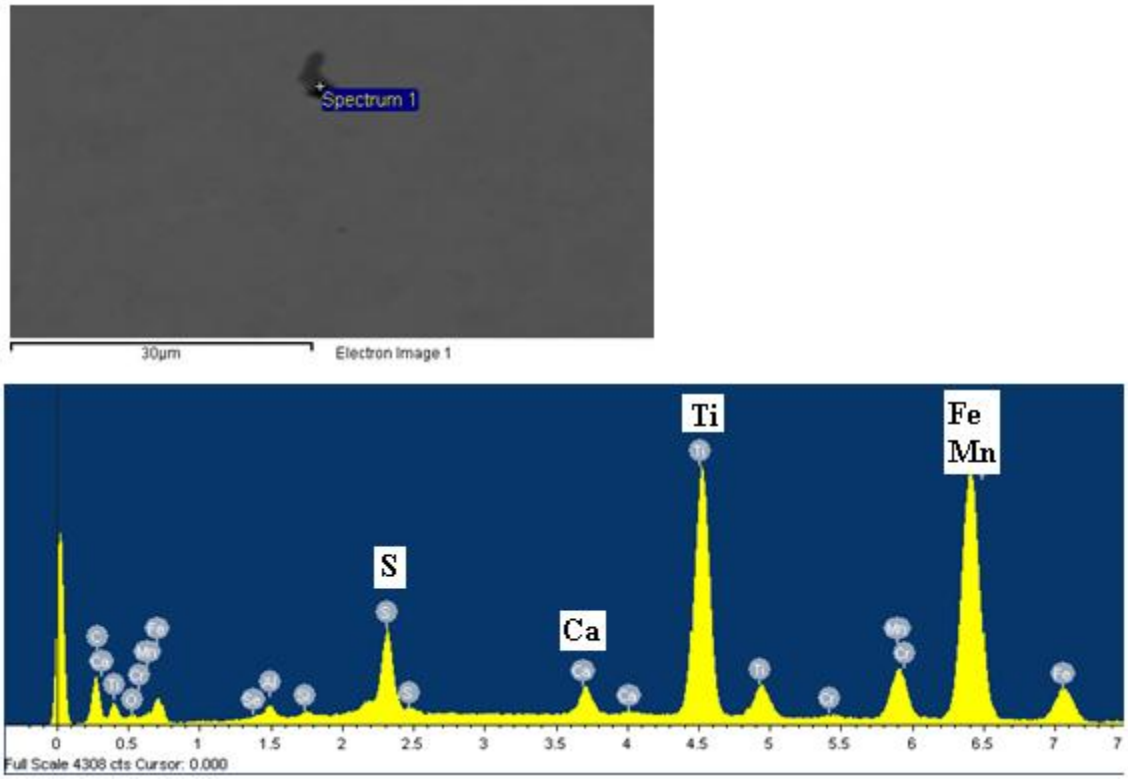

Figure 3.10. EDX sample of MAE, 10 mm, TiN and MnS inclusion.

Table 3.7. TiN inclusion size and number density for the 10.0 mm MAC, MAD and MAE and 16.8 mm MAD thick strips

Strip grade and thickness	**Average feret max. (µm)**	**Feret max. range (µm)**	**Number density (mm^{-2})**
MAC 10 mm	1.92 ±1.41	0.5- 11.5	216
MAD 10 mm	2.18 ±1.85	0.5 - 9.0	241
MAE 10 mm	2.25 ±2.81	0.5- 9.0	186
MAD 16.8 mm	1.6 ±1.60	0.5-9.5	159

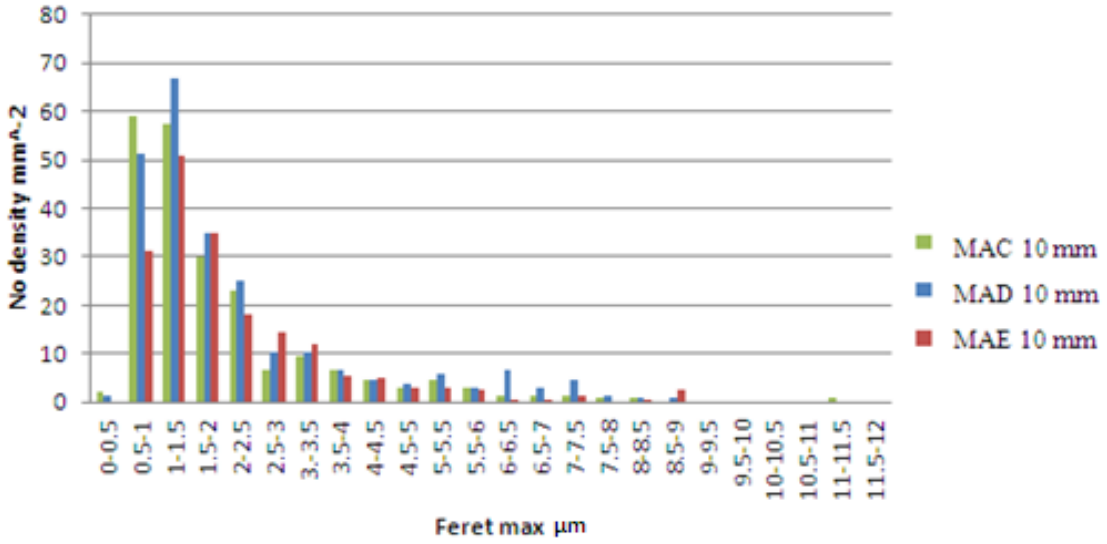

Figure 3.11. Size distribution plot for coarse TiN particles in the 10 mm thick strips of MAC, MAD and MAE.

3.3.4. **Thermo-Calc predictions for TiN**

Prediction of the amount of TiN forming in the range 1470 – 1480 °C was carried out (using Thermo-Calc) and compared to the area % measured, Table 3.8, as this was the temperature range over which TiN started to form coarse inclusions, Figure 3.12. The experimentally measured data showed a higher area % especially in MAD compared to the Thermo-Calc predictions; this could be explained by the optical measurements being those of TiN/ MnS/ Al_2O_3/ Nb (C, N) inclusions, not just pure TiN.

Table 3.8. Thermo-Calc prediction compared to metallographic data for MAC, MAD and MAE at 10 mm.

Sample	Temperature °C	Volume Fraction Thermo-Calc	Area % Metallographically
MAC A	1470	0.038	0.041
MAD B	1470	0.039	0.080
MAE C	1470	0.065	0.051

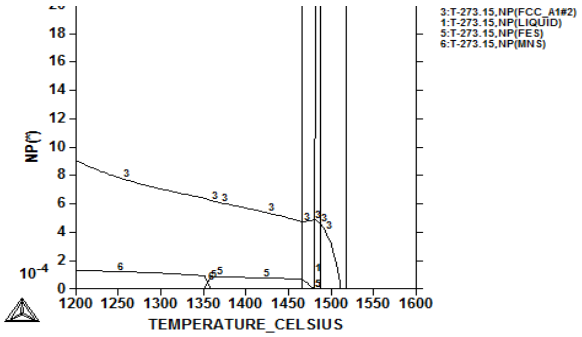

Figure 3.12. Thermo-Calc plot of stable phase mole fraction (NP(*)) as a function of temperature for MAE, the number 3 indicates the TiN.

3.3.5. **Charpy impact testing**

Charpy impact transition curves for the 10 mm and ~16 mm thick strip steels (transverse and longitudinal orientations) are presented in Figures 3.13 – 3.16. The root mean square (RMS) values are given for the Charpy curves and indicate that most scatter is less than ±10 J for all specimens, apart from the longitudinal samples MAD 16.8 mm and MAE 16.4 mm; which give values of ±17.2 and ±20.7 respectively. These larger RMS values can be attributed to the scatter seen at 0 °C in the in MAE 16.4 mm longitudinal, where values range from ~ 30 - 130 J; and in the scatter at the upper shelf for MAD 16.8 mm longitudinal, as the tan-h curves fit between experimental data at 40 and 60 °C. Despite the scatter in the Charpy test results it can be seen that the differences between the ITT values are significant, albeit small for the ~16 mm thick strip samples.

Charpy properties are reported to be worse (higher transition temperature and lower upper shelf energy (USE), (73, 78)) in the transverse orientation and this is also the case for all compositions at the different thicknesses, Figure 3.13 compared to Figure 3.14 for the 10 mm thick strips and Figure 3.15 compared to Figure 3.16 for the ~16 mm thick strips. The impact curves for the 10 mm strip steels, in Figure 3.13 show a steep transition curve for the transversely oriented specimens unlike the impact curves in Figure 3.14 for the longitudinal

specimens. MAE gave the lowest transition temperature followed by MAD then MAC; this is consistent for both the longitudinal and transverse orientations. Figure 3.15 and Figure 3.16 compare MAD and MAE at a thickness of ~16 mm, and show that MAE gives a slightly lower transition temperature then MAD. Table 3.9 summarises the Charpy data.

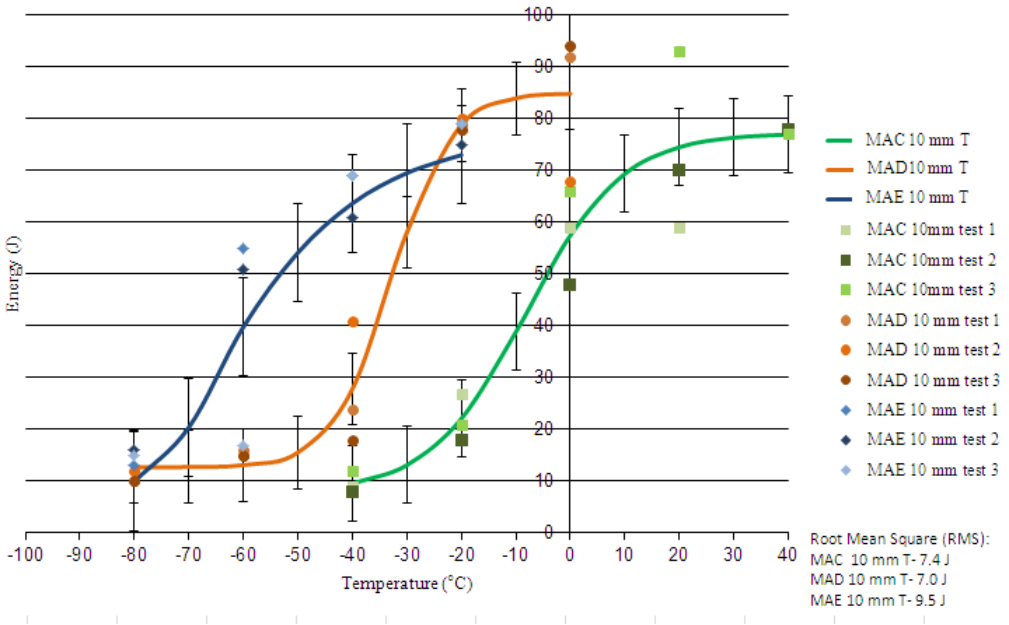

Figure 3.13. Charpy impact results for the 10 mm strips of MAC, MAD and MAE in the transverse orientation (data from Tata Steel U.K. Limited).

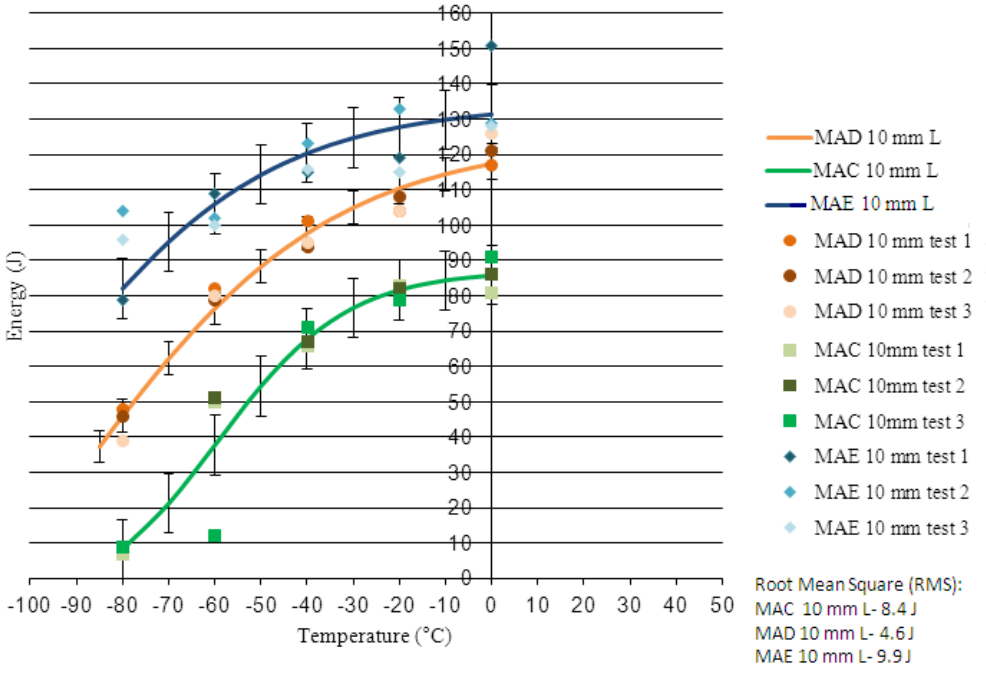

Figure 3.14. Charpy impact results for the 10 mm strips of MAC, MAD and MAE in the longitudinal orientation (data from Tata Steel U.K. Limited).

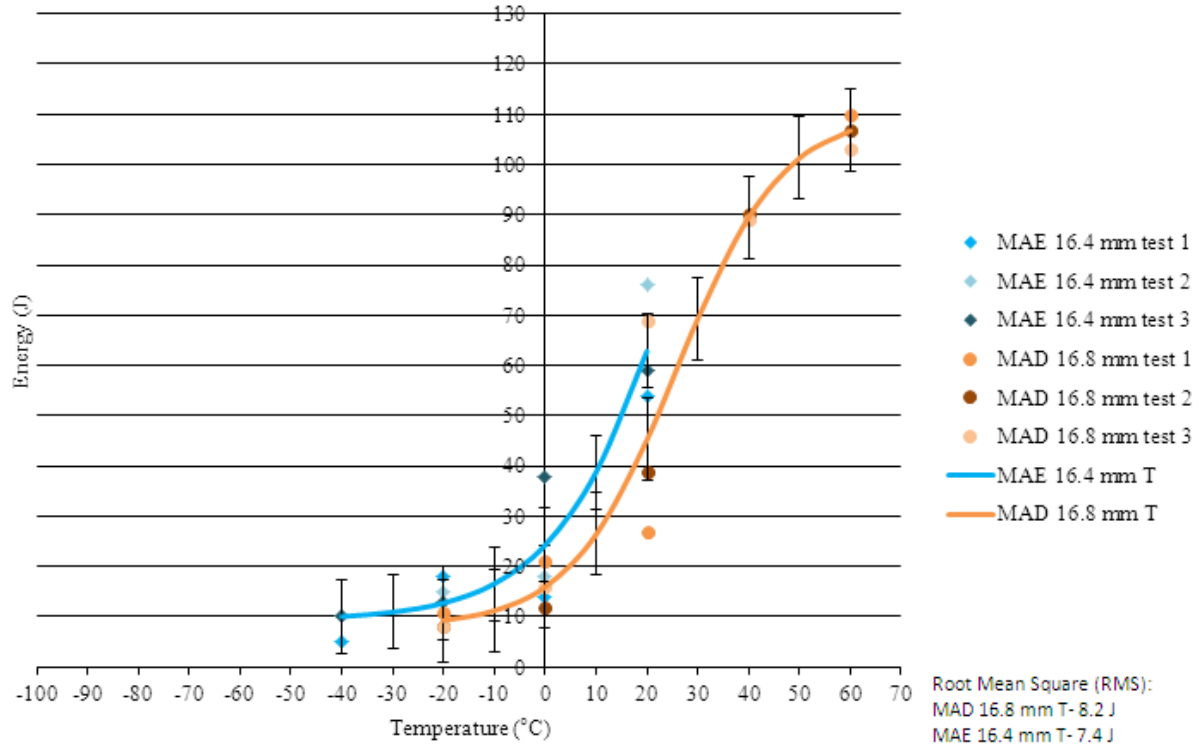

Figure 3.15. Charpy impact results for the ~16 mm strips of MAD and MAE in the transverse orientation (data from Tata Steel U.K. Limited).

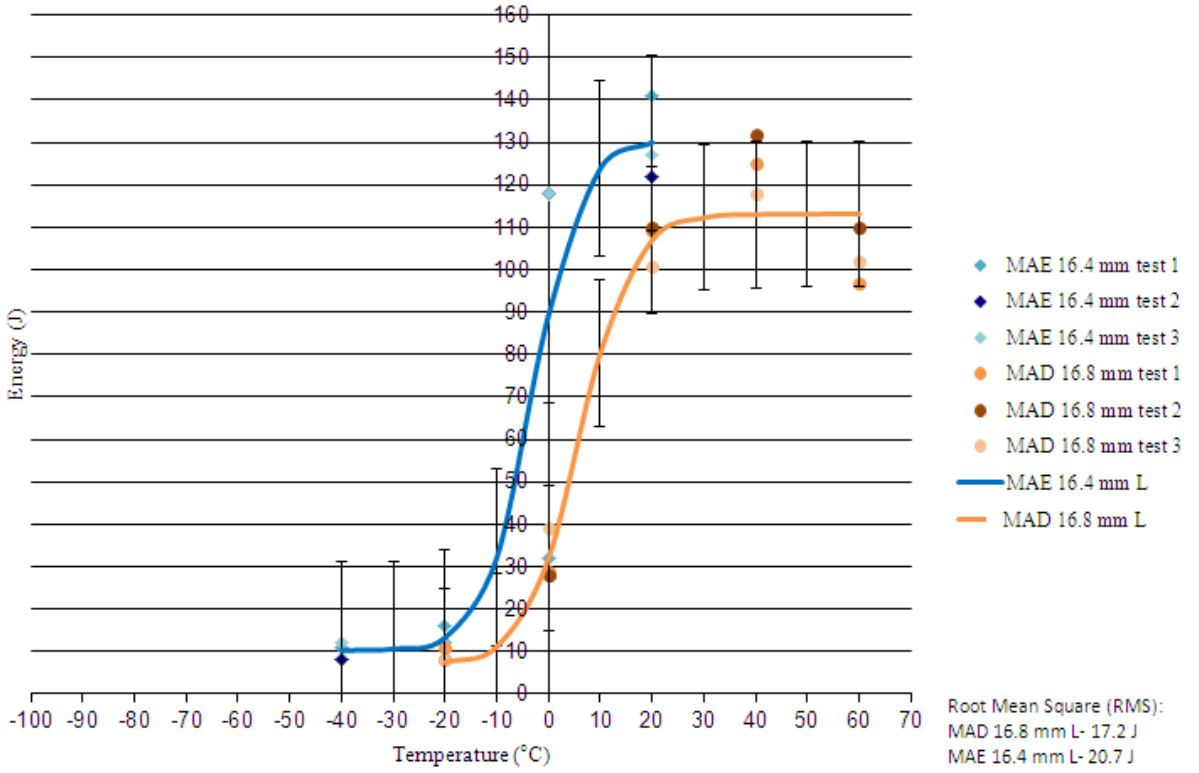

Figure 3.16. Charpy impact results for the ~16 mm strips of MAD and MAE in the longitudinal orientation (data from Tata Steel U.K. Limited).

Table 3.9. Summary of Charpy impact test results.

ID	Composition	Orientation	Thickness (mm)	Upper shelf energy (J)	40 J impact temperature (°C)
A	MAC	L	10	82	-58
B	MAD	L	10	120	-80
C	MAE	L	10	n/a	n/a
J	MAE	L	16.4	130	-8
K	MAD	L	16.8	113	3
A	MAC	T	10	65	-10
B	MAD	T	10	86	-34
C	MAE	T	10	72	-60
J	MAE	T	16.4	n/a	10
K	MAD	T	16.8	111	18

The difference in composition / microstructure between MAC, MAD and MAE does lead to a small difference in the ITT values, which can be attributed to the small differences seen in grain size and yield stress, with 50 % ITT predictions using the Gladman-Pickering equation (section 1.8.1), of -187, -189 and -181 °C for 10 mm MAC, MAD and MAE strip respectively. The main difference is seen between the strips with different thicknesses for the same composition. MAD shows a difference of ~80 ^{0}C in ITT between the 10 and 16.8 mm thick strips in the longitudinal orientation and ~50 °C difference in the transverse orientation, with the thicker strip showing the higher ITT. Due to the significant differences in the ITT values for the different MAD thickness strips these were selected for further analysis, Figure 3.17.

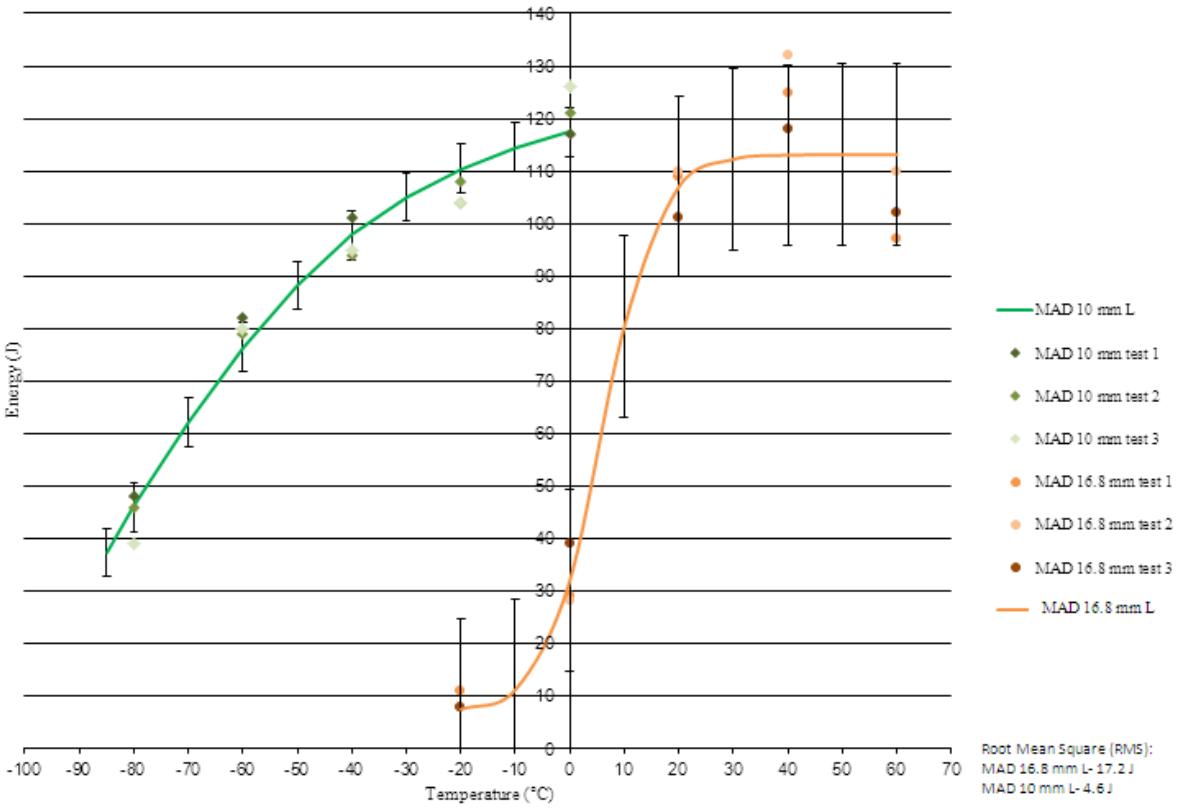

Figure 3.17. Charpy impact results for 16.8 and 10 mm strips of MAD in the longitudinal orientation (data from Tata Steel U.K Limited).

3.4. **Summary of section 3**

Overall it was established that all three compositions contained a similar microstructure, with similar mechanical properties. As the thickness of the strip increased a decrease in toughness and strength properties occurred for all compositions. From the ITT graphs a slight difference can be seen for the different microstructures at the same thickness, which could be down to the slight microstructure changes and composition, but the most significant difference is noted between different thicknesses for a given composition; this is further analysed in section 5. Another dominant effect is that of orientation of the Charpy specimens, with longitudinal specimens producing a lower ITT temperature and a higher upper shelf energy; this is covered in further detail in section 6.

4. FRACTURE ANALYSIS

Specimens recovered from the Charpy impact testing, were prepared and the fracture surfaces analysed by microscopy.

4.1. **TiN Inclusions**

Charpy tests were conducted on steel composition MAD strips of 10 mm and 15.5 mm thickness, and compositions MAC MAD and MAE (using Charpy samples with a 90° notch carried out at the UoB) at 10 mm strip thickness. Fractography was carried out, using a JEOL SEM 6060, on selected specimens. Charpy samples with a 90° notch were tested as the plastic zone ahead of the notch is larger, which increases the volume of material experiencing high stresses/strains, and hence the likelihood of sampling a TiN particle.

Figure 4.1 shows that considerable scatter occurred in the Charpy impact energies for tests carried out with the 90° notch for samples from the compositions MAE, MAD and MAC at 10 mm thickness in the transverse orientation. The scatter is much greater than for the similar tests (10 mm strip thickness transverse orientation) using the 45° notch samples, Figure 3.13, and is most noticeable for the MAD data. For the 90° notch samples a maximum of two repeat tests were carried out so a full error analysis has not been carried out. Charpy curves have not been fitted to the data because of the high scatter in results. The high scatter may be due to the increased volume of material below the notch experiencing high stresses and strains giving increased statistical variability in sampling features that contribute to toughness, such as TiN particles. It is possible that the differing amounts of TiN in the specimens could cause the difference in toughness, with MAD containing a larger amount of Ti (0.089 wt%) followed by MAC (0.082 wt%) then MAE (0.066 wt%). It should be noted that the trend in ITT seen in Figure 4.1 (90° notch tests) is different from that shown in Figure 3.13 (standard 45° notch tests), where the MAE strip has the lowest ITT. Therefore,

the ITT values from the 90° notch tests are not used when comparing the strip steels in the subsequent analysis; however these samples were used to investigate the role of microstructural features on crack initiation below the notch.

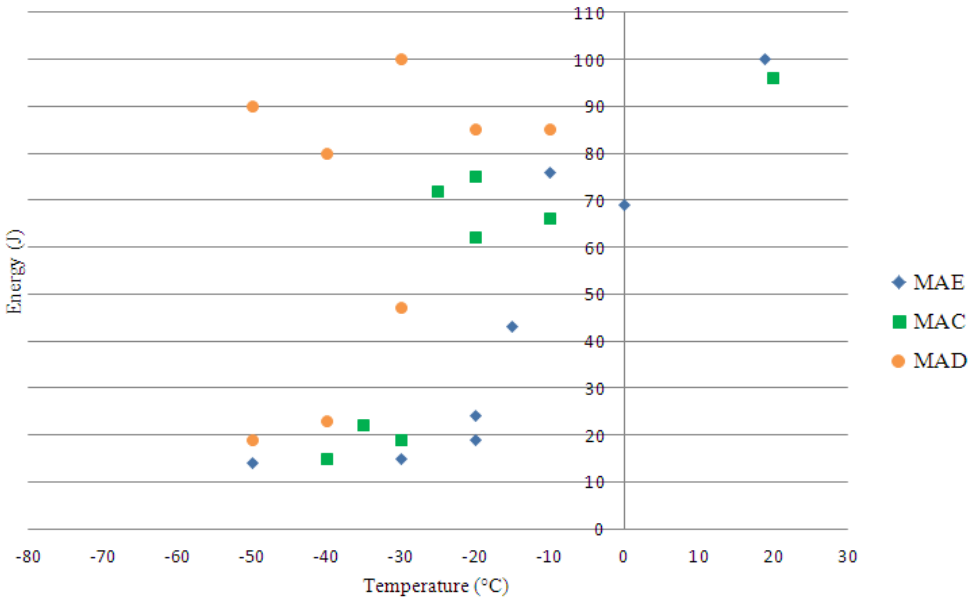

Figure 4.1 Charpy impact results for 10 mm strips of MAC, MAD and MAE, 90° notch transverse orientation (UoB).

Fractography analysis was carried out on the fracture surfaces of both standard 45° and 90° notched samples for 10 and 15.5 mm thick MAD strip. Coarse TiN particles were found on the fracture surfaces for the as-received 15.5 mm thickness strip Charpy samples with a 45° notch in the lower ITT region, but were not seen to initiate cracks, as shown in Figure 4.2. In Figure 4.2 the TiN particle indicated is approximately 3.6 µm in size and is located in a facet of approximately 10 µm in diameter which is 500 µm from notch root, river patterns on the facet confirm that the crack passed around the TiN particle. Figure 4.3 shows the fracture surface for a Charpy specimen with a 90^0 notch for MAD 15.5 mm strip where a coarse TiN particle was seen to initiate cleavage fracture. Figure 4.3 shows the TiN particle to be approximately 4 µm in size and located in a facet of approximately 35 µm in diameter, which is 250 µm from the notch root. No coarse TiN particles were found to cause fracture initiation in the 10 mm thick strip, although TiN particles were seen on the fracture surface, generally

in small voids. One of the main differences between the MAD 10 and 16.8 mm (B and K) thick strip (the 16.8 mm thick strip is very similar to the 15.5 mm thick strip) is that the thicker strip contains coarser grains, Table 3.3; this may contribute to the differing impact behavior and will be discussed further in sections 5 and 6.

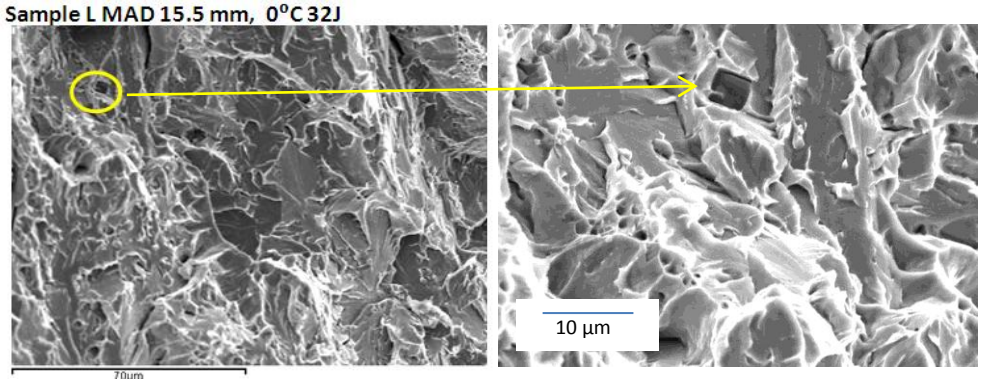

Figure 4.2. SEM image for MAD 15.5 mm strip 45^0 notch sample for a Charpy test at 0 ^{0}C absorbing 32 J.

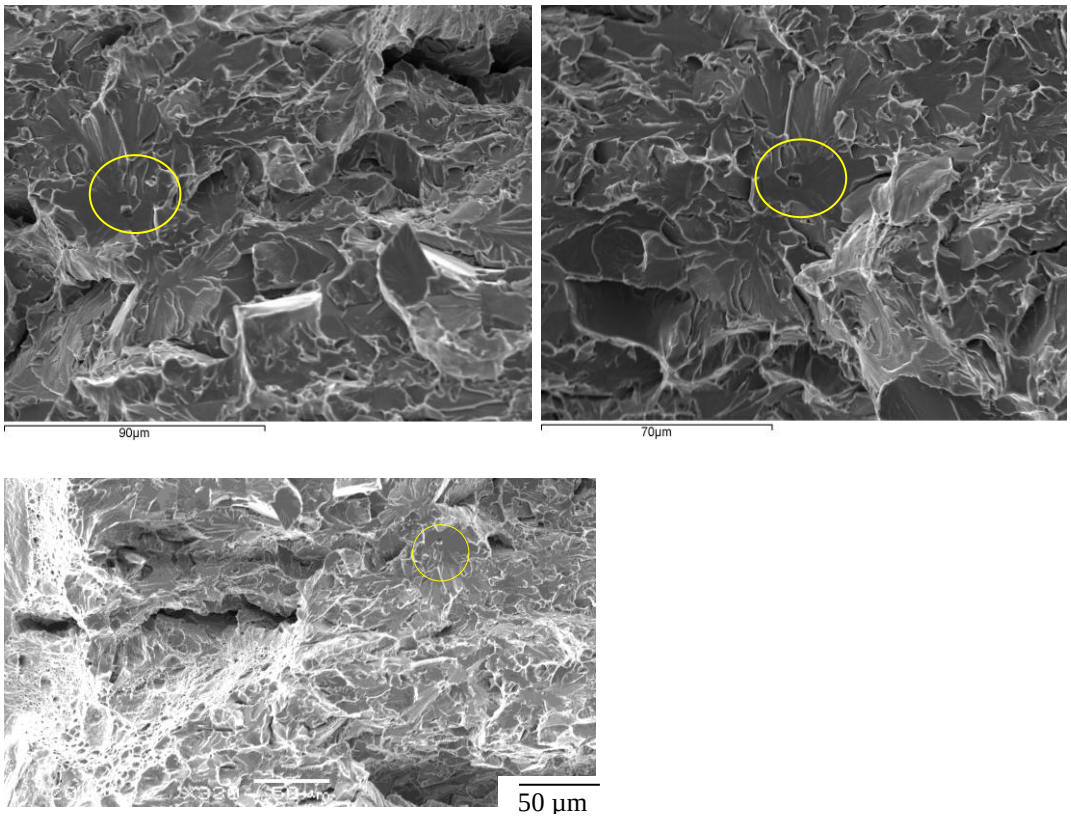

Figure 4.3. SEM image for a MAD 15.5 mm strip sample with a 90^0 notch for a Charpy test at 25 ^{0}C absorbing 18 J. Image shows the inclusions from both Charpy halves and a lower magnification showing the initiation of cleavage failure.

Du et al. (64) investigated three low carbon steels (see Table 4.1 for composition), with a ferrite + pearlite microstructure heat treated to give different ferrite grain sizes, the steels contained TiN particles of a similar size as seen in this work. When coarse TiN particles were present they were found to initiate fracture in the heat treated specimens with an average ferrite grain size in the range 9.5 - 27.3 µm, but no TiN particles were found to initiate cleavage in the heat treated steel with an average grain size of 5 µm. Although Du et al.(64) found TiN particles initiating cleavage, no significant effect was found for these coarse particles on the ITT, with values being adequately predicted by the Mintz et al. equation(58) for the ferrite grain size range of 5 - 27.3 µm. In the absence of coarse TiN particles the effects of ferrite grain size change due to heat treatment were also predicted well by the Mintz et al. equation (with a modification to take into account the presence of 0.50 wt % Ni being used). Therefore, it is suggested that, whilst coarse TiN particles are observed to initiate cleavage in heat-treated and as-received samples (15.5 mm thick strip in the 90° notch Charpy samples only), they may not have a significant effect on the Charpy ITT.

Table 4.1. Composition of steels investigated (wt %) by Du et al.(64)

Materials	C	Si	Mn	P	S	Ni	Mo	Cr	Cu	Al	Nb	V	Ti	N	B
Steel 1	0.093	0.01	1.5	0.01	0.002	<0.02	<0.005	<0.02	<0.02	0.026	0.05	<0.005	0.045	0.0045	–
Steel 2	0.135	0.35	1.33	0.012	0.001	0.02	<0.005	0.03	0.01	0.037	0.027	0.054	0.027	0.0046	0.002
Steel 3	0.087	0.36	1.44	0.01	0.003	0.50	<0.004	0.011	0.004	0.041	0.023	0.004	0.006	0.0061	–

4.1.1. **Summary of effect of TiN**

TiN particles were not found to act as initiation sites in the 45° notch as-received strip (both 10 mm and 15.5 mm thick) samples. However, TiN particles were found to initiate cleavage for the 90° notch samples for the 15.5 mm thick as-received strip. A TiN particle was found to be a cleavage initiation site in one of the specimens, Figure 4.3, with a TiN side length of 4 µm, which is at the coarse end of the size distribution found during optical microscopy characterisation, in a grain size of 22 µm (ECD). Du et al. (64) concluded that even when the

TiN particles are observed to cause cleavage initation this does not have a significant effect on the ITT values, with the ITT predictions, using the Mintz equation, being accurate for heat treated samples with a grain size range of 5 - 27.3 µm even with coarse TiN particles present.

Overall, it was concluded that the effect of TiN on the ITT of these steels, does not play a significant part, which was also confirmed by Du et al.(64), who carried out work on similar microstructures. The Mintz et al. equation used by Du et al. to predict the ITT, did not work for the steels in this study, with values of 19 and 28 °C for MAD 10 and 16.8 mm repectfully, compared to measured 50% ITT values of -75 and -28 °C for MAD 10 and 16.8 mm (see Table 5.5). This could be down to the presence of splits,and the strong influence they have on the ITT, discussed in section 5.

4.2. **Splits/ Fissures/ Laminations**

One of the main distinguishing features on the facture surfaces for many HSLA steels is the presence of splits. Figure 4.4 shows splits on the room temperature Charpy tested specimen facture surfaces, in the longitudinal and transverse orientations for 10 and 16.8 mm thick MAD composition strips. Visibly, a difference can be noticed between the two thicknesses for both orientations, with splits in the 10 mm transverse samples being sharper and more prominent compared to splits in the 16.8 mm transverse, with no splits being seen for samples tested at =<30 ^{0}C in the 16.8 mm transverse orientation. Splits form parallel to the rolling direction, with 3 or more splits being observed on the fracture surfaces (normally 3 full length splits with others being smaller). Splits were detected on the fracture surface in the upper transition and upper shelf region, with a similar number of splits being observed in the samples from the two orientations tested (longitudinal and transverse).

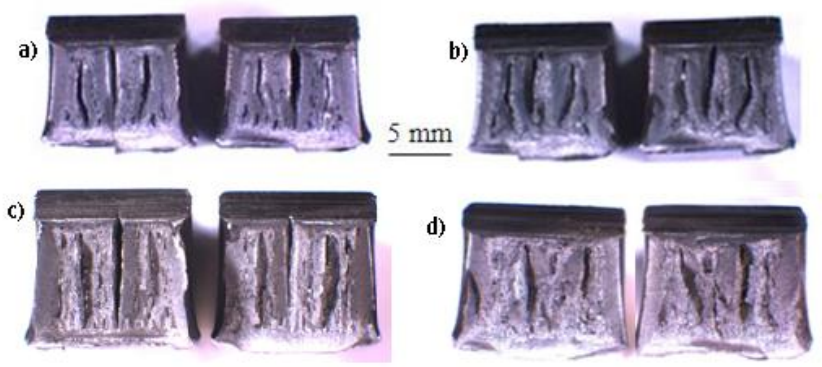

Figure 4.4. Macro images of upper transition region (room temperature) fracture surfaces from longitudinal orientated Charpy specimens of a) 10.0 mm and b) 16.8 mm thick strip, and transverse oriented Charpy specimens c) 10 mm and d) 16.8 mm at 40 °C (when splits formed).

4.3. **Split Fracture Mode**

Splits were characterised according to the classification shown in Figure 4.5. A fully fractured sample from a thick (15.5 mm) strip sample (MAD composition) tested at room temperature was sectioned to observe the split fracture surface (Figure 4.6 and Figure 4.7). The entire split fracture surface was composed of brittle transgranular cleavage fracture, with Figure 4.8 showing this for a 16.8 mm strip after a 100 J low blow Charpy hit (low blow Charpy testing is discussed further in 4.4.1).

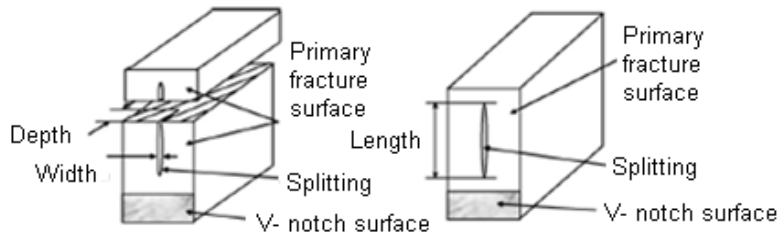

Figure 4.5. Definitions of size for the splits on the fracture surface (71).

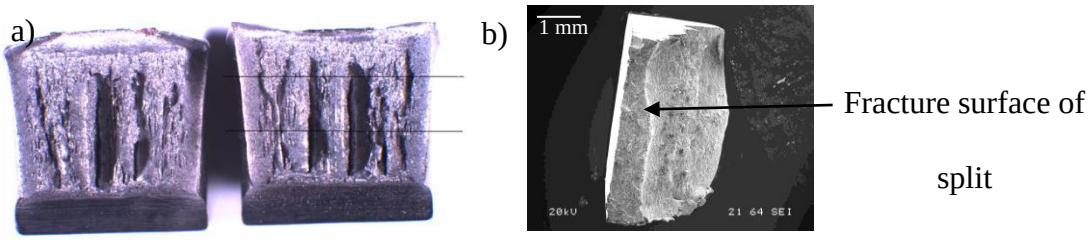

Figure 4.6. Fracture surface of broken Charpy sample tested at room temperature (15.5 mm strip transverse orientation Charpy sample) showing, a) splits on the full fracture surface, b) SEM side view image of the middle split after sectioning to reveal the split surface.

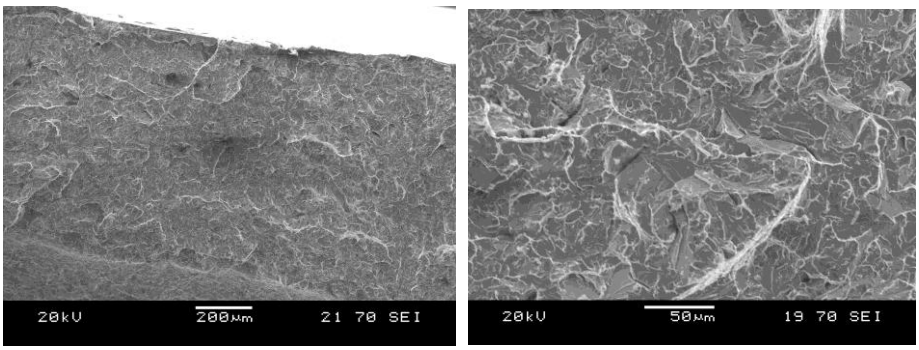

Figure 4.7. Split fracture surface (from Figure 5.6 b) showing transgranular cleavage.

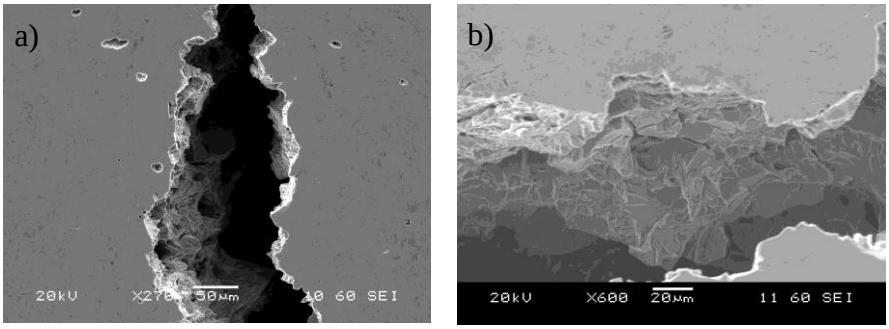

Figure 4.8. SEM micrographs taken from the sectioned strip 16.8 mm longitudinal sample after a low blow Charpy test at 100 J impact energy (used to generate a split crack without overall sample fracture); a) shows the sectioned (and polished) surface with a large split (notch position at bottom of image) and b) shows the split fracture (transgranular cleavage).

4.4. **Split Crack Initiation**

Further analysis was required to determine split initiation so that the operative fracture mechanisms could be identified and related to the microstructure. A variety of techniques were used, which are discussed in this section.

4.4.1. **Low blow Charpy testing**

The initiation of split cracks, and the extent of their growth are important factors in understanding the influence of splitting on the ITT. Therefore low blow Charpy testing was carried out to investigate the energy required to initiate split cracks (and establish the size to which they developed) before overall sample fracture. Samples from the MAD composition strips at 10 and 16.8 mm thickness were used in the longitudinal and transverse orientations. The low blow Charpy impact tests were carried out at room temperature, corresponding to the upper transition region for all tests (where split cracks are observed on the fully broken samples).

4.4.2. **Acoustic emission testing**

To aid in the assessment of the low blow tests, acoustic emission (AE) monitoring was carried out in situ, for the longitudinal specimens. To confirm the identification of the AE signal with split crack formation an annealed, low carbon mild steel was also tested at 20, 40, 60, 80 and 100 J impact energy along with the 10 and 16.8 mm thick strip samples. The upper shelf energy value for the mild steel was 180 J compared to ~120 J for the strip samples, and no split cracks were observed.

During the low blow testing of the mild steel samples only two clear AE signals were recorded, these were related to the hammer hit event (high energy and short duration AE event) and plastic deformation in the sample (low energy and longer duration), shown in

Figure 4.9. Figure 4.10 shows the low blow tested Charpy mild steel sample illustrating the angle through which the sample bent (up to 27 ^{0}), with no splits expected as none are seen on the fully fractured samples. The power spectra (Power vs. Frequency) AE data for the mild steel sample related to plastic deformation shows a peak at 50 kHz. There was no significant difference noticed for the mild steel in the acoustic signal for the low blow tests with 40 – 100 J impact energy, apart from a slight increase of up to 10 dB (97) noted in the amplitude for the increase in impact energy. This would be consistent with the increase in the volume of the specimen which is plastically deformed.

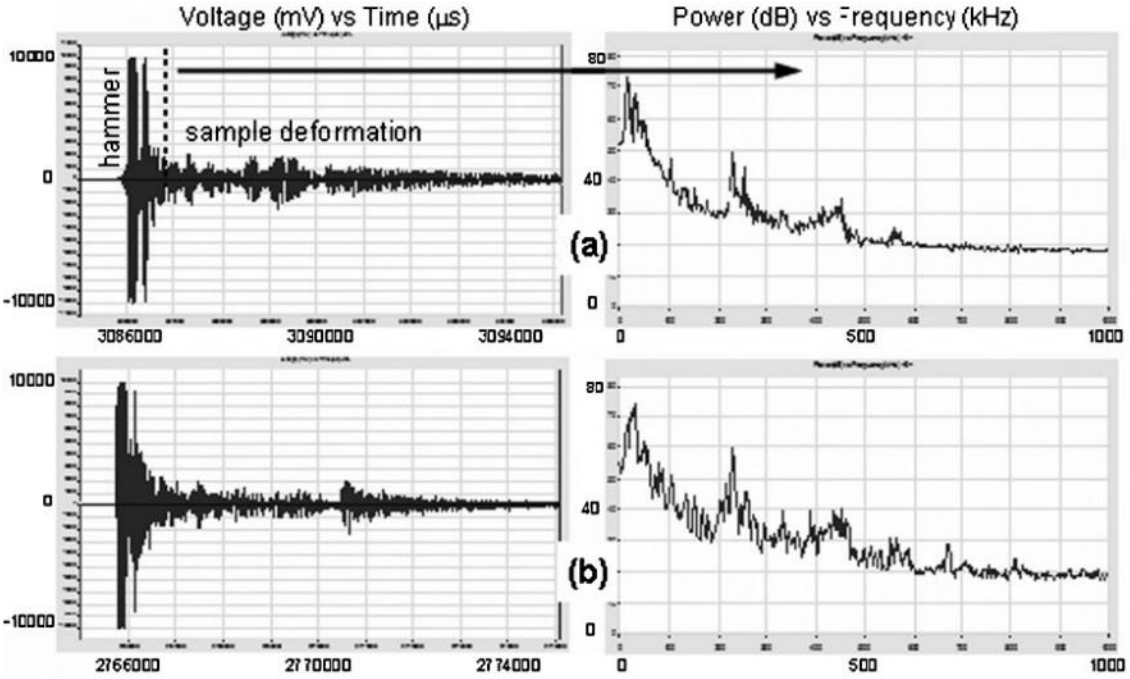

Figure 4.9. Acoustic waves (a) and power spectra (b) for the mild steel samples tested with a) 60 and b) 80 J low blow hit for the sample deformation only, not the hammer hit (97).

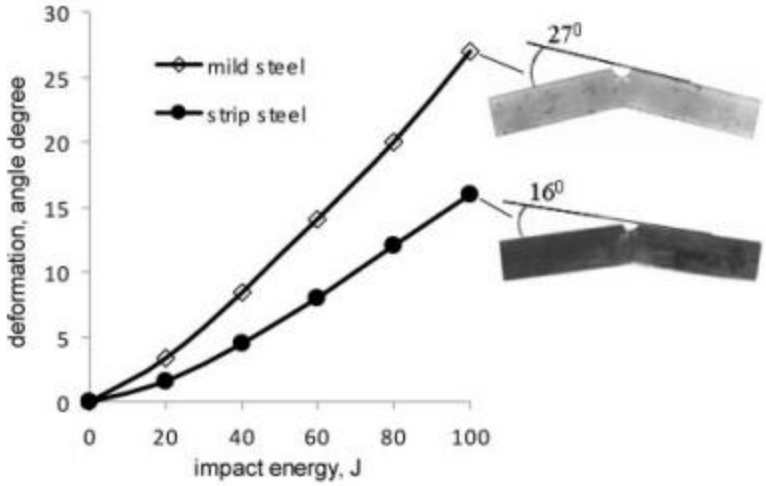

Figure 4.10. Deformation of samples for mild steel and the MAD 16.8 mm thick strip (97).

The acoustic wave time traces for the strip steels show contributions from the hammer blow (short time, high amplitude) and plastic deformation (lower amplitude over a longer time period), in the same manner as those for the mild steel samples. A third peak in the trace was also observed in some of the strip steel tests carried out at impact energies above 70 J, which had a high amplitude at times intermediate between the hammer blow and plastic deformation signals, Figure 4.11. This trace was ascribed to the formation of split cracks and was found to correspond to a higher amplitude at approximately 40 kHz in the power spectrum.

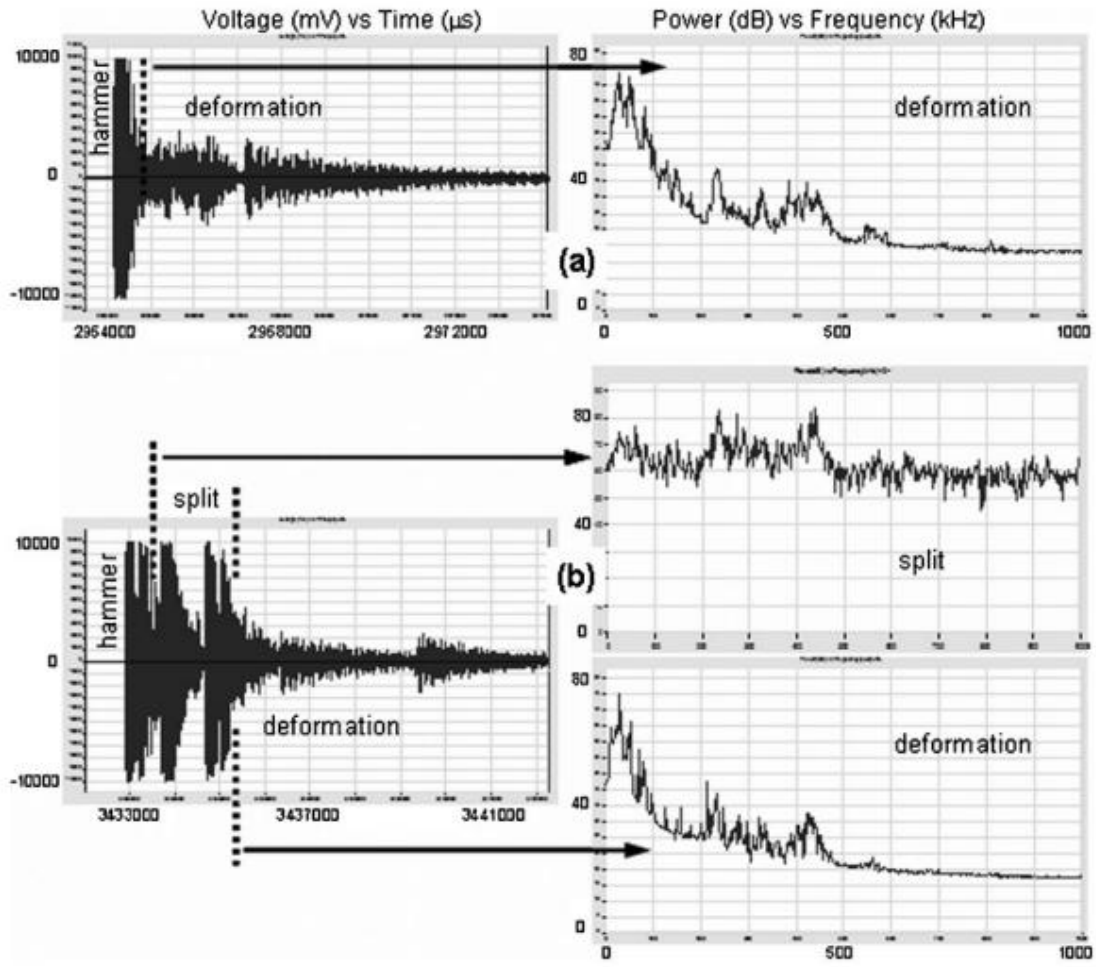

Figure 4.11. Acoustic waves and power spectra for the MAD 16.8 mm longitudinal low blow tests with a) 60 J (no split crack signal observed) and b) 80 J (split crack signal observed) impact energy (97).

Due to the size of the samples and the use of only one AE sensor it was not possible to locate the origin of the split signal, nor to differentiate whether there was one or more split cracks forming.

The presence of split cracks when an AE signal was identified was confirmed by subsequent sectioning of the low blow sample, Table 4.2. The smallest split crack seen during all testing, and identified by the AE signal, was subsequently measured to be 1.6 mm in length. AE testing was not carried out on specimens in the transverse orientation (discussed in section 6) as the sensor could only be used for room temperature testing and the transverse specimens

required low blow testing at higher temperatures to generate split cracks. AE testing was confirmed to be a viable technique for detecting the formation of splits during low blow testing.

Table 4.2. Acoustic emission data with relation to presence of split(s) for longitudinal orientated specimens.

Sample	**Impact energy (J)**	**AE confirms split**	**Microscopy confirms Split**
16.8 long	300	N/A	Y
16.8 long	100	Y	Y
16.8 long	80	Y	Y
16.8 long	70	Y	Y
16.8 long	60	N	N
10.0 long	300	N/A	Y
10.0 long	100	Y	Y
10.0 long	80	Y	Y
10.0 long	70	Y	Y
10.0 long	60	N	N

4.4.3. **X-ray Tomography**

X-ray tomography was carried out on a number of low blow tested specimens and the results, in terms of the observation of split cracks, matched with the AE data, Table 4.2. AE cannot distinguish the size or number of splits present, whereas X-ray tomography can do so by producing a 3D image, in which splits are clearly identified (if they are sufficiently large to be resolved). X-ray tomography has the advantage that the specimens do not need to be sectioned unlike samples for optical microscopy and SEM, which require the split cracks to be sectioned in the correct place and the removal of some material. Micro CT scans clearly showed the presence of split cracks after low blow impacts, e.g. Figure 4.12.

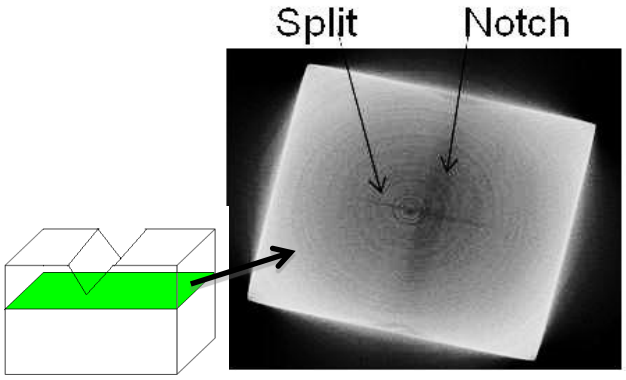

Figure 4.12. A slice from the X-ray tomography carried out on the 10 mm longitudinal orientation sample with a low blow hit of 70 J.

To observe the 3D image of the splits the co-ordinates of the splits (points plotting around the split as shown in Figure 4.12) were entered into a Matlab model from X-ray slices spaced at about 4.5 µm normal to the notch (length), Figure 4.13 and Figure 4.14. This analysis was also carried out on Charpy specimens tested at 300 J on the upper shelf to observe the depth of the splits which have fully failed and are denoted in the tables by having an impact energy hit of the full 300 J. Micro CT was carried out on the specimens, and these results were then confirmed by sectioning and using microscopy to directly measure the split depth and width.

A difference between the X-ray tomography and microscopy data was seen for the split crack sizes for three samples; the 16.8 mm thick strip with a low blow impact energy of 70 J, and the 10 and 16.8 mm strip with a 300 J hit (fully broken sample), Table 4.3. Errors can arise when the samples are cut if the sectioning is not perpendicular to the split and through the deepest point. The depth measured for the 300 J hit for the 10 and 16.8 mm thick samples are in reasonable agreement, with a difference of ~1 mm in length being observed for one of the three splits present in both specimens. Resolution limits with X-ray tomography can also cause a problem; it has been found that when the cracks are very fine (crack faces pressed together) the full crack is not observed during micro-tomography, with the resolution determined to be around 0.2 mm for the length and 0.15 mm for the width by comparing the tomography and macro images. Tomography data can give a smaller value of size as they do not necessarily resolve the fine cracks, which can open up during sectioning and are then quantified. These data are summarised in Table 4.3.

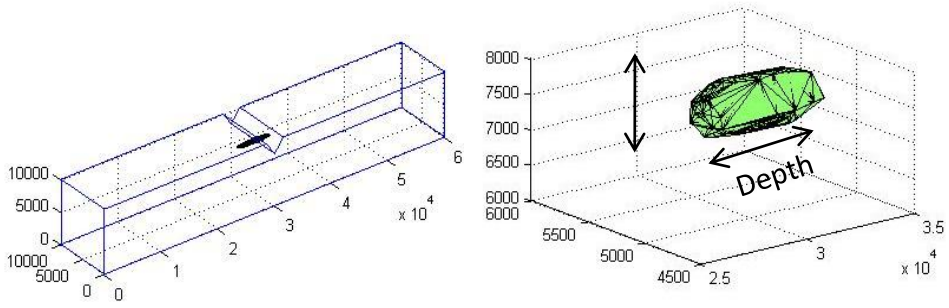

Figure 4.13. 3-D image of a split crack, generated using a Matlab model, for the 10 mm longitudinal orientation Charpy sample with a low blow hit of 70 J.

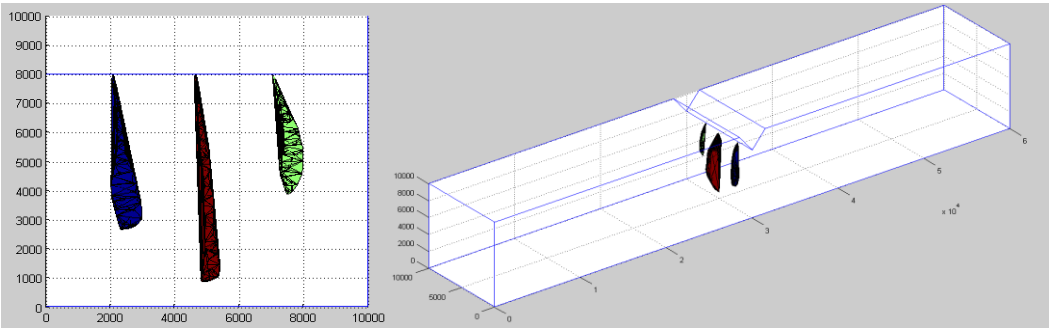

Figure 4.14. 3-D image of a split, generated using a Matlab model, for the 10 mm longitudinal orientation on a 300 J Charpy specimen, fully upper shelf, with the Charpy specimen in two pieces.

Table 4.3. Summary of the presence and size of splits formed during Charpy tests carried out on 10.0 and 16.8 mm strips in the longitudinal orientation, numbers in bold indicate the split in the middle of the samples. Multiple values indicate number of splits, with bold numbers indicating middle split.

Sample	Impact energy, J	AE confirms split	Microscopy confirms Split	Split length from optical microscopy mm	Split depth from optical microscopy mm	Split length from X-ray Tomography mm	Split depth from X-ray Tomography mm
16.8 long	300J blow (100 J absorbed)	-	Y	5.7, **5.9**, 3.7	3, **5.9**, 3	5, **6**, 4	4.2, **5.4**, 3,2
16.8 long	100	Y	Y	**3.5**	**3.4**		
16.8 long	80	Y	Y	**4.2**	**3.6**		
16.8 long	70	Y	Y	**2.9**	**3.4**	**1.6**	**3.5**
16.8 long	60	N	N	-	-	-	-
10.0 long	300J blow (114 J absorbed)	-	Y	5.3, **6.2**, 5.2	3.2, **5.2**, 1.6	5.4, **7.1**, 4.1	3.4, **5.4**, 3
10.0 long	100	Y	Y	**4.3**	**5.4**		
10.0 long	80	Y	Y	**4.4**	**4.8**		
10.0 long	70	Y	Y	**3.5**	**5.8**	**3.3**	**5.9**
10.0 long	60	N	N	-	-	-	-

4.5. **Summary of Section 4**

This section focuses on fracture analysis of the broken Charpy specimens, and the characterisation of any splits present. The fracture surface for the splits is a brittle transgranular cleavage, which occurs before main crack extension from the notch. In this chapter longitudinal specimens were analysed for two thicknesses, 10 and 16.8 mm for the MAD composition with three experimental techniques used - AE, X-ray tomography and final sectioning and microscopy of all specimens to confirm results. All three methods were found to be effective methods to distinguish and characterise splits, with optical being used as an independent check to correlate the AE and tomography data.

From the previous section the main difference seen in the Charpy transition curves is seen when the thickness is increased (with a lower ITT seen for the thicker strips). The splits seen in the 10 and 16.8 mm strips are also significantly different, with the thinner strip showing deeper and longer splits, this is carried out in more detail in section 5.

5. SPLITS - COMPARISON OF LONGITUDINAL 10 AND 16.8 MM THICK STRIPS

As mentioned previously, the main difference in toughness properties observed for the different strip steels (compositions and thicknesses) was between the 10 and 16.8 mm MAD composition strip. The microstructure for the two thicknesses have been discussed previously (see section 3.3) and are shown in Figure 5.1 and summarised in Table 3.2.

The average grain sizes were found to be 4.9 µm and 4.3 µm for the 16.8 and 10 mm strip thicknesses respectively. The 16.8 mm strip also contained a higher % of coarse grains than the 10 mm strip, 42 % compared to 11 %. The coarse TiN particles were measured (see Table 3.7) and it was found that the thicker strip has a slightly smaller average inclusion size (1.6 compared to 2.2 µm) and contained a smaller number density (159 compared to 241 per mm^2) for the coarse inclusions, however TiN inclusions were present across the same size range in both thicknesses. The differences seen in the number density and average feret max size are consistent with the greater rolling reduction that the thinner strip experiences, so that coarse TiN inclusions are sampled more frequently; both strips are produced from the same cast and are therefore expected to have the same TiN distribution before rolling.

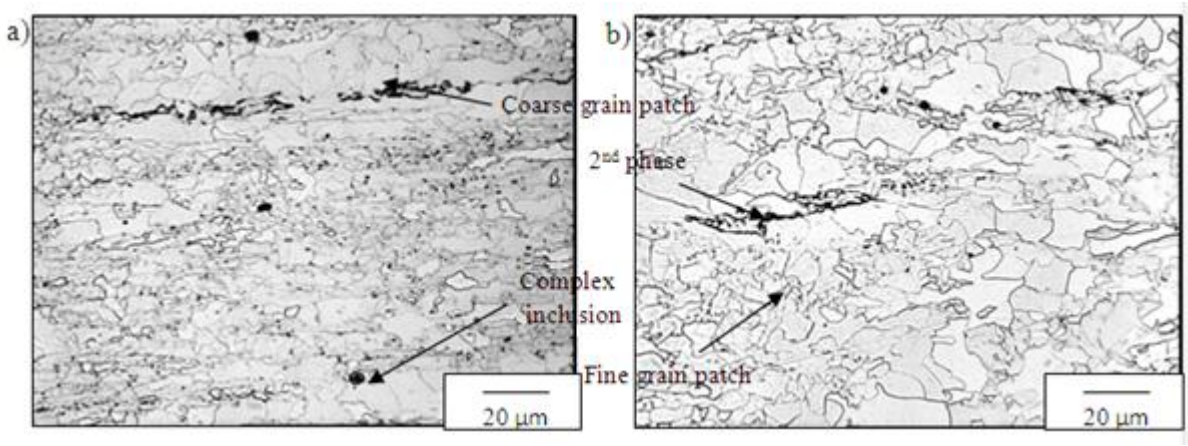

Figure 5.1. Optical micrographs a) 10 mm thickness and b) 16.8 mm thickness in the longitudinal orientation

5.1. **Charpy impact toughness of the 16.8 and 10 mm strips in the longitudinal orientation.**

Figure 5.2 compares the transition behaviour of the 10 and 16.8 mm strip in the longitudinal and transverse orientations. The 10 mm strip has a lower 40 J ITT by ~80 °C compared to the 16.8 mm strip for the longitudinal orientation and ~50 °C in the transverse. For the MAD composition RT is on the upper shelf for all the specimens, bar the 16.8 mm strip which does not reach the upper shelf until ≥40 °C. The RMS values show that the difference in ITT values is significant, and not just down to results scatter. Full upper shelf energy Charpy specimens for the 16.8 mm strip transverse and longitudinal specimens has been carried out at the University of Birmingham (UoB), with the transverse data presented in section 6, figure 6.1, these results correlated well with Tata Steel data.

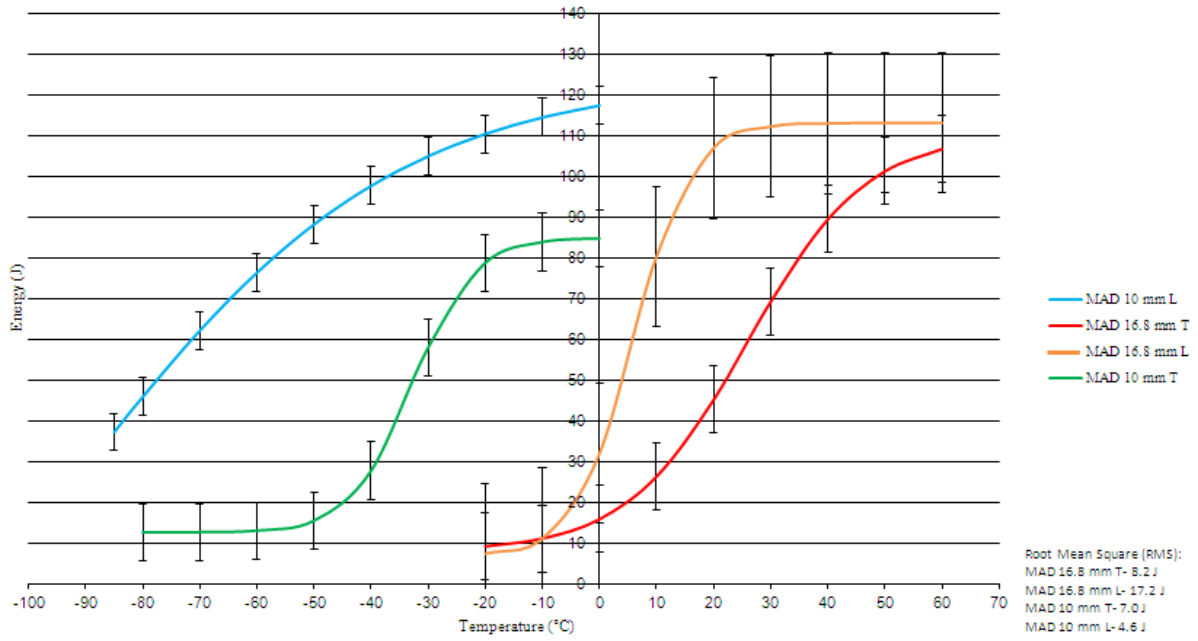

Figure 5.2. Charpy ITT curves for MAD composition for 10 and 16.8 mm strip in the longitudinal and transverse orientation. For individual data points refer to section 3.3.5 (data from Tata Steel U.K. Limited).

The Charpy impact fracture surfaces are shown in Figure 4.4 for the samples tested at room temperature from both thickness strips and it can be seen that they show similar characteristics of general ductile failure with splits present. Splits were observed on the fracture surfaces for both strips in the upper transition and upper shelf region with a similar number of splits noted at each temperature.

5.2. **Split crack initiation**

A summary of the low blow impact testing results, in terms of the split cracks observed is given in Table 4.3 along with split sizes for the full hit Charpy samples for both thicknesses. Splits were present following low blow tests with impact energies ≥70 J, and were not observed for low blow tests with an impact energy ≤ 60 J, for both strip thicknesses. This was confirmed by sectioning, shown in Figure 5.3 and Figure 5.4. The fact that splits do not form during low blow tests with an impact energy of < 70 J suggests that a certain amount of

energy is required to initiate splits, which indicates that some plastic deformation is required. This is consistent with the absence of splits on the fracture surfaces of lower shelf Charpy specimens.

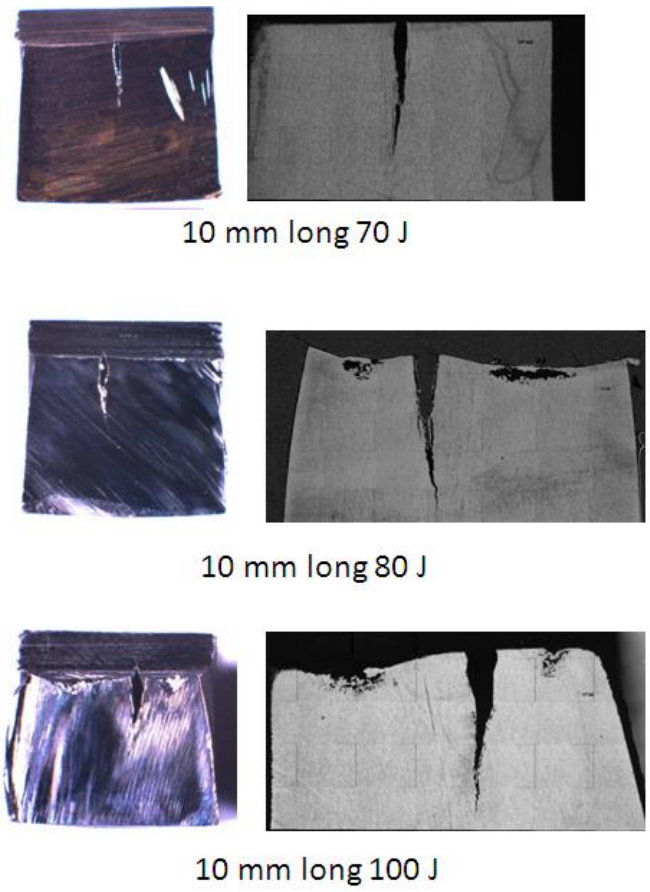

Figure 5.3. Macro-images and optical images for low blow tests carried out at 70, 80 and 100 J on the 10 mm longitudinal samples of MAD.

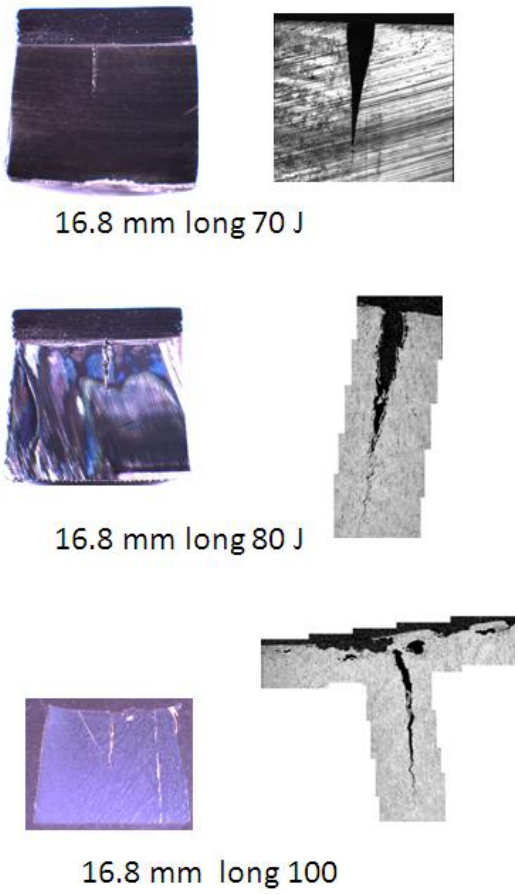

Figure 5.4. Macro-images and optical images for sectioned samples from low blow tests carried out with an impact energy of 70, 80 and 100 J on the 10 mm thick MAD strip in the longitudinal orientation.

Higher magnification images of a single split, formed in the 16.8 mm thick MAD longitudinal specimens with 100 and 80 J hits, are shown in Figure 5.5 and Figure 5.6. Specimens with a single split showed that the split initiated in the middle of the specimen at the base of the notch, which is the region of highest strain and plane strain constraint. Subsequent splits (if present) then formed either side of the main split, halving the ligaments on either side. One split in the middle of the specimen formed in all low blow tests carried out at impact energies of $\geq$ 70 J. In addition, large voids were observed in the region where the initiation of further splits occurred on the fully fractured specimens, Figure 5.7.

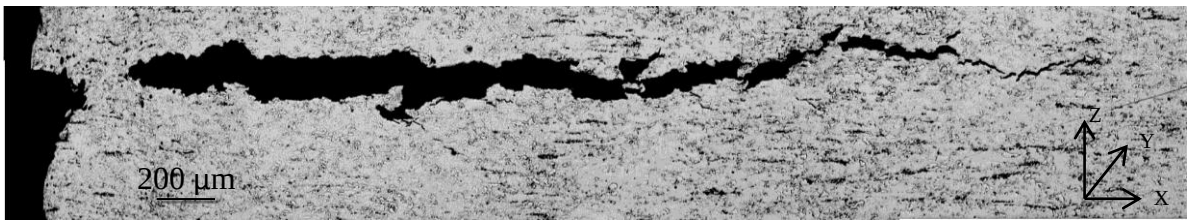

Figure 5.5. Optical microscopy image for the sectioned low blow (100 J impact energy) sample from the 16.8 mm strip in the longitudinal orientation showing a large (≈3.5 mm length) split. The notch position is to the left of the image.

Figure 5.6. Optical microscopy image for the sectioned low blow (80 J impact energy) sample from the 16.8 mm strip in the longitudinal orientation showing a large (≈4.2 mm length) split. The notch position is to the left of the image.

At the head of a split crack, which is near the notch of the Charpy specimen, coarse TiN inclusions / complex TiN-containing inclusions were observed to have initiated voids, an example of this is shown in Figure 5.7. Voids, which contained TiN particles, were also observed in 2nd phase regions, Figure 5.8. Figure 5.8 also shows a void with a TiN particle away from the 2nd phase region and a void, which may have initiated on a TiN (not present in the plane of view), in the 2nd phase region. It is not clear if voids forming on TiN inclusions or 2nd phase initiate the split crack. Voids with TiN particles present were only observed in the region around the beginning of the split near the notch, voiding was not observed around the split for the rest of its length and no ductile voids were observed on the split fracture surfaces. No other inclusions (MnS or Al_2O_3) or carbides were observed to be present in these voids, just pure TiN or complex TiN (containing a mixture of TiN, MnS and Al_2O_3).

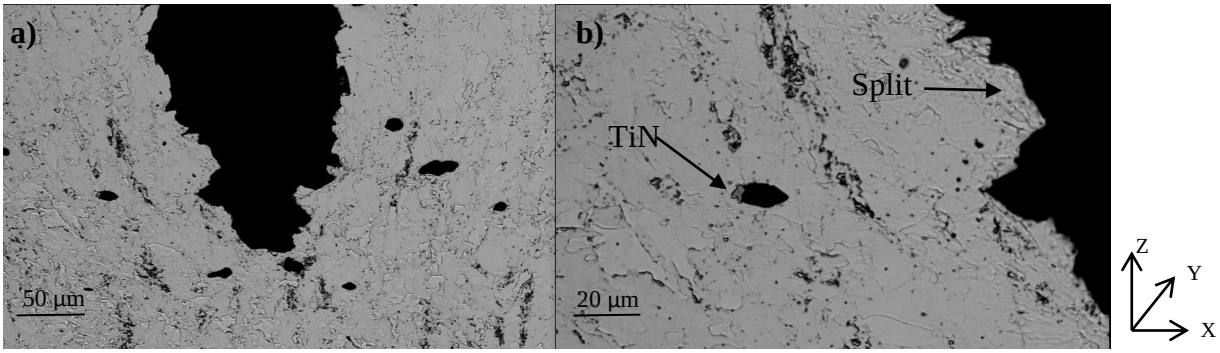

Figure 5.7. Images from the sectioned low blow Charpy sample from the 16.8 mm thick MAD strip, longitudinal with a 100 J impact energy hit showing voids detected near the notch. (a) Overview of crack tip region and (b) higher magnification image of TiN particle and associated void.

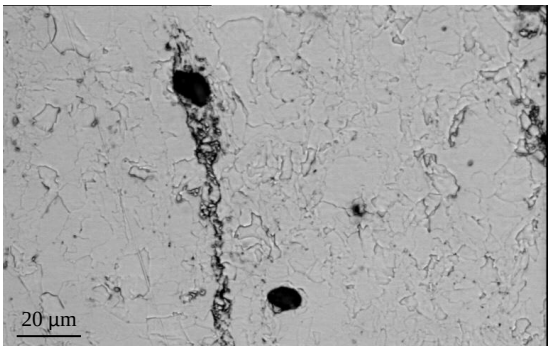

Figure 5.8. Sectioned low blow Charpy sample from the 16.8 mm thick MAD strip, longitudinal with a 100 J impact energy hit showing void formation in the second phase, note that the other void is associated with a TiN particle.

5.3. **Split crack propagation relative to the microstructure**

Song et al. (80) observed a split crack path in ultrafine grained C–Mn steels, and noted its direction changed when it crossed high angle boundaries. A decrease in grain size is generally associated with greater toughness and increased resistance to crack initiation/propagation. The grain size associated with the split cracks was determined by measuring the fraction of the split length, in the sectioned etched sample, that occurred in fine grained (≤4 µm ECD ferrite grain size) material compared to coarse grained material (≥5 µm ECD ferrite grain size), shown in Figure 5.9.

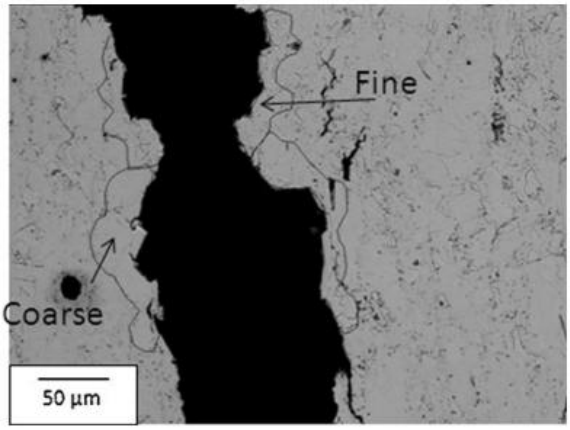

Figure 5.9. Optical microscopy image for the sectioned low blow (100 J impact energy) sample from the 16.8 mm strip, showing coarse and fine grain patches along the split crack length.

Table 5.1 shows the percent of coarse-grained microstructure associated with the main split crack. For the 16.8 mm thick MAD strip at 80 J low blow impact energy in the longitudinal orientation the length of the split is 61% in coarse grained material, which compares to only 42 % coarse patches in the microstructure overall. Figure 5.10 shows examples of the coarse patches in the overall microstructure. Splits were consistently observed to propagate through a higher amount of coarse grains than present in the overall structure (Figure 5.10), which suggests that splits tended to preferentially propagate through the coarse grained regions.

Table 5.1. Percentage of coarse and fine grain patches along the split crack length and in the overall microstructure.

Strip thickness (mm)	Low blow impact energy (J)	Coarse grain patches % around split	Coarse grain patches % microstructure	Split length (mm)	Aspect Ratio of Fine Grains	Aspect Ratio of Coarse Grains
16.8	100	61	42	3.5	1.67	1.57
16.8	80	70	42	4.2	1.67	1.57
10.0	100	59	11	4.3	1.67	1.59
10.0	80	73	11	4.4	1.67	1.59

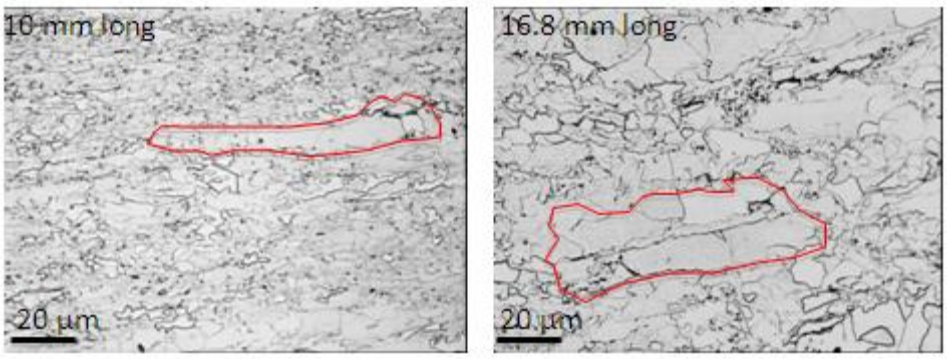

Figure 5.10. Examples of coarse patches identified (outlined in red) in the 10 and 16.8 mm thick MAD strip in the longitudinal orientation.

Song et al. (80) established that, for a C-Mn steel to achieve a combination of excellent strength and toughness, an ultrafine grain size (average grain diameter 1.3 µm) is required produced by large strain warm deformation (at 550 ^{0}C warm deformation was performed by a four-pass plane strain compression process, with an inter-pass time of 0.5 s. Each of the four subsequent steps imposed a logarithmic strain of 0.4). Song et al. (80) performed the large strain warm deformation after the recrystallisation stop temperature achieving pancake grains - the greater rolling reduction increased the presence and number of splits in Charpy tests (80). Therefore it might be expected that the 10 mm strip would show a greater number

or size (length and/or depth) of splits compared to the 16.8 mm strip, as they were both rolled from the same starting thickness slab. Table 5.2 - Table 5.4 contain the rolling schedules for the 10 and 16.8 mm thick MAD strips, with both strips going through the same roughing process (Table 5.2). The differences in rolling stages are presented in Table 5.3 (10 mm) and Table 5.4 (16.8 mm), which show that the 10 mm thick strip goes through an extra rolling pass (6 compared to 5 for the 16.8 mm strip) and more strain is used in the initial rolling stages. A 16 ^{0}C difference is noted for the final rolling temperature with the thicker strip having the higher temperature. These results correlate with data seen for the work carried out by Song et al. (80), with the strips used in this study producing deeper splits when they had undergone extra rolling and higher strains (10 mm).

Table 5.2. Rolling data for the roughing stands

Pass number	Thickness in (mm)	Thickness out (mm)	Strain at stand	Strain rate (s^{-1})	Average temperature (°C)
VW1_1	225	206	0.102	0.974	1173
VW1_2	206	181	0.149	1.245	1164
VW1_3	181	158	0.157	1.599	1155
VW1_4	158	133	0.199	1.944	1146
VW1_5	133	110	0.219	2.462	1137
VW2	110	81	0.353	2.903	1120
VW3	81	62	0.309	5.172	1103
VW4	62	46	0.345	12.715	1086
VW6	46	37	0.251	16.874	1069

Table 5.3. Rolling data for the finishing stands on the hot rolling mill for the 10 mm thick MAD strip.

Pass number	Thickness in (mm)	Thickness out (mm)	Strain at stand	Strain rate (s^{-1})	Average temperature (°C)
EW1	35.839	25.951	0.373	6.743	1007
EW2	25.951	19.55	0.327	9.741	984
EW3	19.55	15.957	0.234	11.961	958
EW4	15.957	13.07	0.23	16.17	941
EW5	13.07	11.497	0.148	17.108	921
EW6	11.497	9.887	0.174	22.627	906
EW7	9.887	9.89	.	.	890

Table 5.4. Rolling data from the finishing stands on the hot rolling mill for the ~16 mm thick MAD strip.

Pass number	Thickness in (mm)	Thickness out (mm)	Strain at stand	Strain rate (s^{-1})	Average temperature (°C)
EW1	35.865	28.559	0.263	6.305	1015
EW2	28.559	23.907	0.205	7.336	994
EW3	23.907	21.246	0.136	7.502	970
EW4	21.246	18.471	0.162	10.052	947
EW5	18.471	16.319	0.143	11.998	922
EW6	16.319	16.319	.	.	907
EW7	16.319	16.321	.	.	891

Considering the lengths of the splits, from Table 4.3, it can be seen that there is no significant difference between the splits for the 10 mm and 16.8 mm thick MAD samples on the fully broken Charpy fracture surfaces. However, there is a difference in the split depth for the low blow hits, with the 10 mm samples showing deeper splits. It should be noted that the low blow Charpy test temperature used does represent a slightly different position on the transition curve for the 10 and 16.8 mm thick strips. However, the results are consistent with the literature suggesting that the greater rolling reduction for the 10 mm thick strip results in deeper splits. These deeper splits may be a contributing factor to the lower ITT values for the 10 mm thick strip.

5.3.1. **Texture in the longitudinal 10 and 16.8 mm strip**

Some authors (78, 85) have reported that texture influences split formation in steels and this has been assessed for the 10 mm and 16.8 mm thick MAD strip samples. {100} is the preferred cleavage plane in ferritic steels, as the steel strip is hot rolled whilst austenitic the main plane aligned parallel to the rolling plane is {110}(69). Orientation distribution functions (ODFs) were measured by Tata Steel; Figure 5.11 shows that there is a weak texture for both strips (maximum intensity of 7x background for the 10 mm thick MAD strip at the ¾ thickness position. The strongest texture components in the 10 mm strip are {113}<110> and {110}<110>, whist the strongest texture in the 16.8 mm strip are {001}<110> and {110}<001>, with some variation seen at different positions through thickness. EBSD analysis was carried out to determine if there was a difference in texture between the coarse and fine grains, and the results shown in Figure 5.12. No distinguishable differences were detected between the fine and coarse regions, therefore it is unlikely that texture is a major factor in the formation of splits in these strips and does not explain the difference in the ITT between the two strip thicknesses.

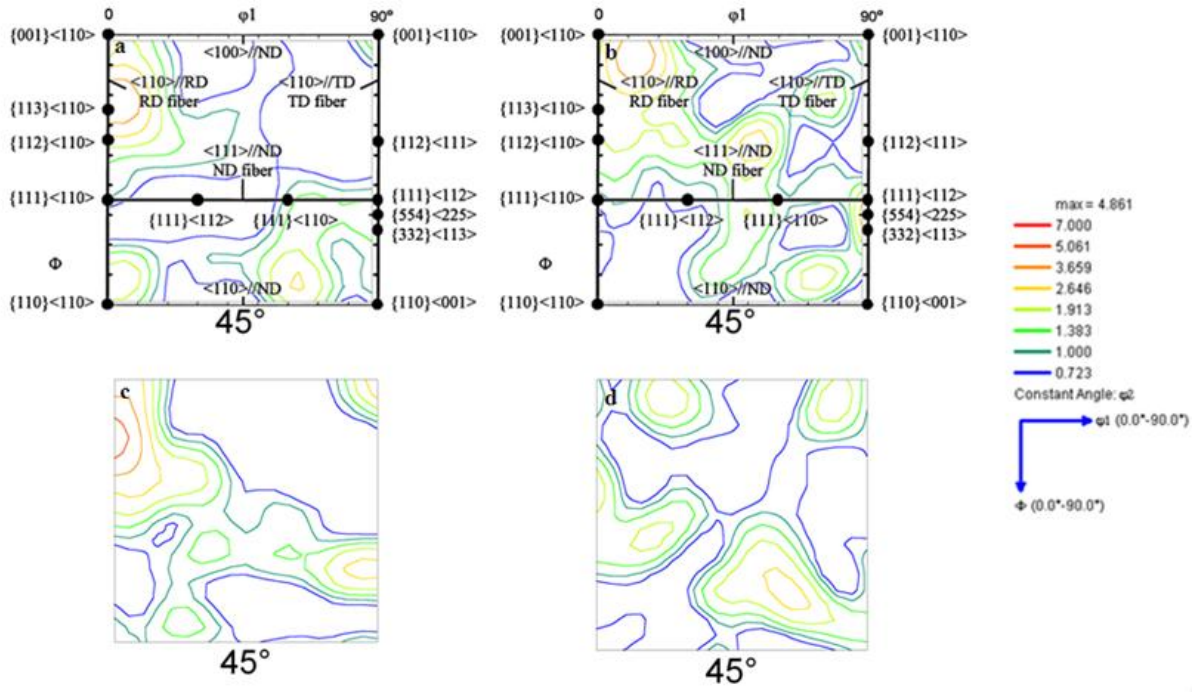

Figure 5.11. Orientation distribution function (ODF) for a) 10 mm thick MAD strip ¼ thickness b) 16.8 mm thick MAD strip ¼ thickness c) 10 mm strip ¾ thickness and d) 16.8 mm strip ¾ thickness (data from Tata Steel U.K. Limited). Superimposed is the φ2 = 45 deg ODF section showing the position of the main texture components (98).

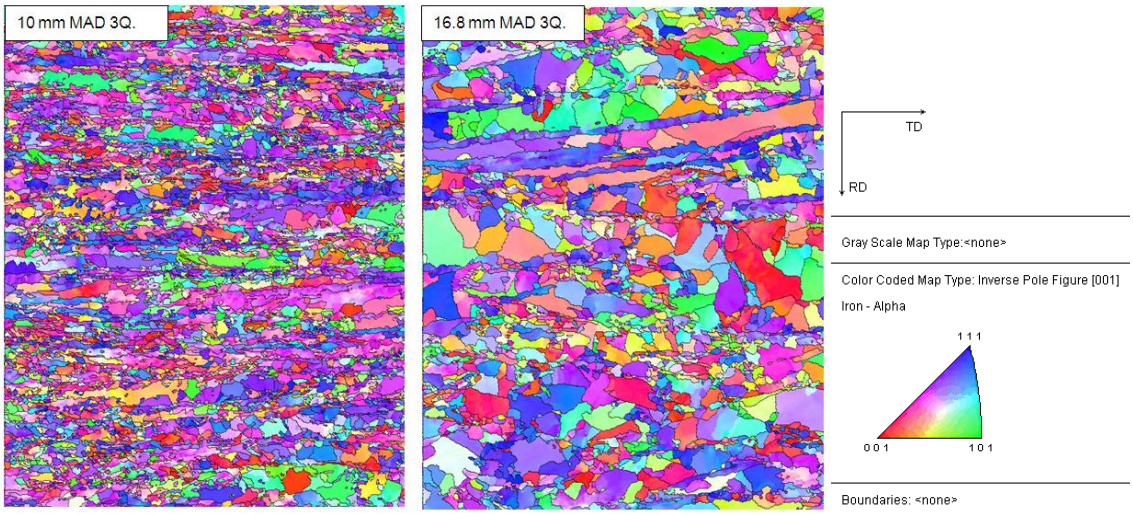

Figure 5.12. Inverse Pole Figures (IPF) analysis, carried out at the ¾ thickness position, with a 5° misorientation, to detect if any difference in texture is noted between coarse and fine regions for the 10 and 16.8 mm strip, (data from Tata Steel U.K. Limited).

5.3.2. **Effect of yield stress, carbide thickness and second phase on the ITT**

The difference in yield stress between the different strip steels (composition and thickness) was discussed in section 3.3. The effect of yield stress on ITT needs to be considered to determine if this can explain the difference in ITT between the 10 mm and 16.8 mm thick MAD strips. The yield stress values for the 10 and 16.8 mm thick MAD strips are 726 and 685 MPa respectively. This difference in yield stress is assumed to be due to differences in dislocation density (due to differences in work hardening on uncoiling the strip, expected to be a minor effect) and fine scale precipitation, since the average grain sizes are similar (4.33 compared to 4.99 µm, which equates to a yield stress difference of 16 MPa with a k_y value of 13) and the composition is the same.

The Mintz et al. equation (58) predicts a higher 50% ITT for the 10 mm thick MAD strip compared to the 16.8 mm thick MAD strip, based on the difference in strength alone (Table 5.5). When grain boundary carbides and the amount of 2^{nd} phase is taken into account (0.32 and 0.38 µm for the 10 and 16.8 mm respectively for the grain boundary carbide thickness and 0.33 and 0.24 % for the 10 and 16.8 mm thick MAD strips respectively for the percent of 2^{nd} phase). The Mintz et al. equation gives a difference of 9 ^{0}C in the ITT with the 16.8 mm strip having the higher value (19 °C and 28 °C for the 10 and 16.8 mm thick strips respectively) - see Table 5.5 for predicted and measured values. The Gladman - Pickering equation (1) predicted a difference in ITT of 12.5 ^{0}C with the 10 mm strip producing the lower value.

The experimental ITT values presented in section 3.3.5 show a difference of 80 ^{0}C for the ITTs between the 10 and 16.8 mm thick MAD strips in the longitudinal orientation, with the 16.8 mm strip showing the higher ITT. This indicates that the predictive equations do not

account for these steels well. Equations 1.7 and 1.8 were developed for steels that did not contain strong texture, splits or mesotexture. Therefore the predictions using these equations are not expected to be accurate, but can be used to determine how large the discrepancy is. Hence, the differences in yield stress; carbide thickness; and second phase cannot be accounted for using these equations. However, the large difference in experimental ITT values between the two strip thicknesses is likely to be greater than that achieved by these factors, so that other features, such as the difference in the depth of splits and the proportion of coarse grained patches, need to be considered.

Table 5.5. 50 % ITT predictions (°C) and measured values.

Material	50% ITT measured	°J measured	Predicted 50% ITT (Mintz et al.)	Predicted 50% ITT (Gladman - Pickering)	Predicted 50% ITT (Mintz et al.) 90th percentile
B MAD	-65	-80	19	-189	66
K MAD	6	3	28	-176	76

5.3.3. **Aspect Ratio**

Since the split cracks were observed to preferentially follow the coarse grain size patches the aspect ratio of these patches were assessed since it has been reported that there is an effect of grain aspect ratio on splits, with increased elongation of grains leading to larger/ more splits (79, 77).

Table 5.1 shows that the aspect ratio for the individual fine grains is the same for both thicknesses, with the individual coarse grain aspect ratio being fairly similar at 1.59 and 1.57 for the 10 and 16.8 mm thick MAD strips respectively. Therefore the aspect ratio of the coarse grain patches was considered (it was difficult to define fine grain patches in the 10 mm thick strip, as the majority of the microstructure was fine and contained isolated coarse

grained patches, hence only coarse grain size patches were measured). The 10 mm thick strip has coarse grain patches with an aspect ratio of 4.0 compared to 2.0 for the 16.8 mm thick strip, confirming that the 10 mm thick strip had coarse patches that are slightly more elongated. This may be the main contributing factor to the difference in depth of the splits measured between the two strip thicknesses, as all other factors are similar.

Mintz et al. (77) noted that, in plain C-Mn steel, the presence of a greater number of splits on the fracture surface gave a lower fracture appearance transition temperature (FATT). The number of splits that formed was related to the different grain aspect ratios generated through the application of different rolling reductions. No reduction had an aspect ratio of 1.23 with an average of 0.5 splits on the fracture surfaces examined, 10% rolling reduction gave an aspect ratio of 1.76 and two splits, 20% rolling reduction gave an aspect ratio of 2.45 and an average of 2 splits whilst 40% rolling reduction gave an aspect ratio of 3.80 and an average of 4 splits. The depth of the splits was not reported in the paper. In the current study the aspect ratios are 1.67 / 1.59 and 1.67 / 1.57 for the ferrite grains (fine / coarse), and 4 and 2 for the coarse grain patches, for the 10 and 16.8 mm thick strips respectively. On average 3 splits are seen on the fracture surfaces for both the 10 and 16.8 mm thick strip samples.

Mintz et al. (77) state that splits only lowered the FATT when a 40 % rolling reduction was used and the presence of more than two splits seemed to be the influential factor in reducing the FATT, when the increased dislocation density from cold deformation should have increased it. Bramfitt and Marder (79) concluded that splits propagated along the grain boundaries of elongated ferrite grains in a high purity Fe-1 wt% Mn alloy (used to eliminate other effects thought to influence the formation of splits such as the presence of sulphides, pearlite and carbides). It was found that splits were only present in the longitudinal Charpy

specimens when grain elongation reached a critical point, corresponding to an aspect ratio of 3.4 (79).

5.3.4. **Grain Boundary Misorientation**

It has been reported in the literature that grain boundary misorientation values below 12 ° do not significantly affect the cleavage crack path, and therefore toughness (41). It was suggested that when predicting Charpy toughness of TMCR steels boundaries with a low misorientation angle of <12 ° should be dismissed when determining the effective grain size. The distributions of grain boundary misorientation angles for fine and coarse grained patches for the 10 and 16.8 mm thick MAD strip is shown in Figure 5.13. Figure 5.13 shows that there is no significant difference between the samples and so grain boundary misorientation is not considered to be an influential factor in this study. It was also concluded by Bhattacharjee and Davis (41) that even if a difference in misorientation values is noted, the effect is small, for example for a deviation of 12 ° a decrease in energy-release rate for a kink propagating from a pre-existing crack is approximately 5 % when compared to a coplanar crack.

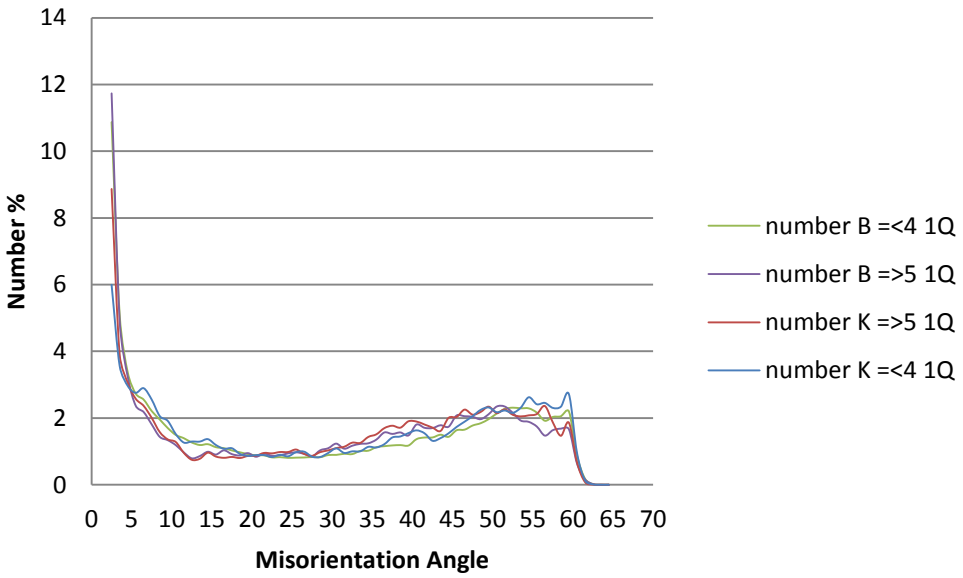

Figure 5.13. Grain boundary misorientation angles in the 10mm (B) and 16.8 mm (K) strip, with the data divided into coarse (≥5 µm) and fine (≤4 µm) grain regions (data from Tata Steel U.K. Limited).

5.4. **Sub-size Charpy specimens**

The effects of sub-size Charpy specimens on impact energy and behaviour and the equations used to predict these have been discussed in the literature review section 1.10.2. The Wallin et al. (87) equation was used in this study and gave a shift of -45 ^{o}C in the ITT due to the formation of 3 splits, Table 5.6. The depth of the splits has been seen to be greater in the 10 mm thick strip compared to the 16.8 mm thick strip, reducing the plane strain constraint, and therefore decreasing the ITT of the 10 mm thick strip compared to the 16.8 mm thick strip. In the 16.8 mm thick strip the splits are not dividing the sample into smaller sections as effectively as in thinner strips, whilst for the 10 mm thick strip their greater depth results in a more significant effect.

Table 5.6. Shift in ITT predicted by the Wallin et al. equation

Effective thickness of specimen (mm)	**Splits**	**ITT Shift (^{0}C)**
5	1	-20
2.5	3	-45
2	5	-56

5.5. **Summary of section 5**

For the 10 and 16.8 mm thick strips, low blow Charpy impact hits were carried out at room temperature, which corresponds to the upper transition range for the strips in the longitudinal orientation. The low blow hits were carried out to understand the formation of splits seen on the fracture surfaces of fully ductile Charpy specimens. It was found that there is a large difference in the ITT between the 10 and 16.8 mm thick strips of 80 ^{0}C. An average of three splits was observed on the fracture surfaces for both strips in the upper transition region, with the splits being consistently deeper in the low blow hits on the 10 mm thick strip. Splits only formed in both strips at room temperature with low blow hits of 70 J and above, which

corresponds to >55 % of the total fracture energy. No splits were observed in either the 10 or 16.8 mm thick strips in the longitudinal orientation for low blow impact energies <60 J. The splits observed in both the low blow hits and the broken fracture surfaces were found to be brittle and propagated by transgranular cleavage, preferentially following the coarse grain patches in the microstructure. The greater split depth seen in the 10 mm thick strip correlates with the higher aspect ratio and reduced area fraction of the coarse grain patches in the material when compared to the 16.8 mm thick strip.

Other characteristics of the microstructure were shown not to affect toughness, with the strip steels showing weak texture and no alignment of carbides or elongated MnS particles, which had previously been seen to influence split formation. These factors are similar for the two strips and are not responsible for the difference in toughness noted for the 10 and 16.8 mm thick strips. Differences noted in the grain size, grain boundary carbide size, yield stress and amount of second phase were predicted to give a difference of between 8.5 and 12 °C in ITT (Mintz et al. (58) and Gladman-Pickering (1) equations respectively). The difference between grain boundary misorientation was also found to have no significant effect for the fine and coarse regions for the 10 and 16.8 mm thick strips; there was also no difference in texture noted for the fine and coarse patches in both thicknesses.

6. SPLITS - COMPARISON OF LONGITUDINAL AND TRANSVERSE ORIENTATIONS

In addition to the difference in ITT between the 10 and 16.8 mm thick MAD strip samples (longitudinal orientation) there is also a difference in ITT between the longitudinally and transversely oriented samples, Figures 6.1 and 6.2. The yield stresses of the 10 mm and 16.8 mm thick strip samples, Table 3.1, are similar with a difference of 41 MPa between the 10.0 and 16.8 mm strips in the longitudinal orientation and 47 MPa in the transverse orientation, with the 10.0 mm thick strip having the higher value in both cases. The transversely oriented samples give higher tensile strength values than the longitudinally oriented samples, by 97 MPa for the 10.0 mm thick strip and 73 MPa for the 16.8 mm thick strip.

The difference in yield stress between the two test orientations is ascribed to the shape and size of the grains (79), with the longitudinal orientation test sampling elongated grains compared to a more equiaxed grain structure for the transversely oriented test samples. The elongated grains allow for a greater mean free path for dislocations between grain boundaries which results in a higher stress intensification at the head of any dislocation pile-ups, requiring less external stress to overcome the critical resolved shear stress and initiate yielding beyond the first grain. This effect will be modified by any crystallographic texture present, however as the texture in the strip samples is weak, see section 5.3.1, this is expected to be a minor factor. The yield stress of a material affects the stress developed under a blunt notch through the plastic zone size and the stress levels achieved within it, which will affect the toughness.

6.1. **Microstructure**

The microstructure contains the same inclusions and grain banding seen in the longitudinal specimens for the 10 and 16.8 mm thick MAD strip, although the grains are more equiaxed in the transverse orientation, see Figure 3.6. The average grain size is larger in the thicker strip for both longitudinal and transverse orientations with the 16.8 mm thick strip in the transverse orientation having the largest grain size. It is shown in Table 6.1 that the % of coarse patches is similar in the 10 mm thick strip for both longitudinal and transverse orientation (11 and 15 % respectively). The 16.8 mm thick strip contains the highest % of coarse patches at 50 % in the transverse orientation with 42 % measured for the longitudinal orientation.

As previously noted in the comparison between thicknesses in the longitudinal orientation, (section 5), the aspect ratio of the coarse grain patches appears to be an important factor in determining the depth of splits formed during Charpy impact testing.

The aspect ratio of grains was also measured for the transversely oriented specimens with both the 10 and 16.8 mm thick strip samples, as was done with the longitudinal specimens. The transversely oriented specimens produced higher aspect ratios for individual grains compared to the same thickness in the longitudinal orientation. Comparison of the aspect ratios for the coarse grain patches, in Table 6.1, reveals that the 10 mm thick longitudinal strip grain patches give the higher aspect ratio, with the values in the 10 and 16.8 mm strips in the transverse orientation differing by only 0.3. The thicker strip in the longitudinal orientation gives the lowest aspect ratio value of 2.0. These results would suggest that the extra rolling received in the 10 mm thick strip has a strong influence in the longitudinal

orientation, with the 10 mm transverse, having an aspect ratio in the coarse grain patches similar to the thicker strips.

Table 6.1. Grain size comparison for longitudinally (L) and transversely (T) oriented specimens for MAD 10 and 16.8 mm thick strips (AR: aspect ratio).

	Average Grain Size (μm)	**% Coarse Grain in Microstructure**	**AR Coarse Grain Patch**	**AR Individual Fine Grains**	**AR Individual Coarse Grains**
10 mm L	4.33	11	4.0	1.67	1.57
16.8 mm L	4.99	42	2.0	1.67	1.59
10 mm T	3.47	15	2.5	2.32	2.49
16.8 mm T	5.13	50	2.2	2.12	2.19

6.2. **Comparison between the ITT values for the transverse and longitudinal orientations**

The Charpy curves for the different orientations are shown in Figure 5.2 and summarised in Table 3.9. The 10 mm thick MAD strip longitudinal orientation gives the lowest 40 J ITT followed by the 10 mm thick MAD strip transversely oriented samples (difference in ITT of 46 ^{0}C between the 10 mm strip longitudinal and transverse). The thicker strip samples show the higher ITT values, with the 16.8 mm thick transverse strip having the highest value with a difference of 15 ^{0}C between the two orientations. From Figure 6.1 it can be seen that the Tata Steel and UoB experimental data correlate well.

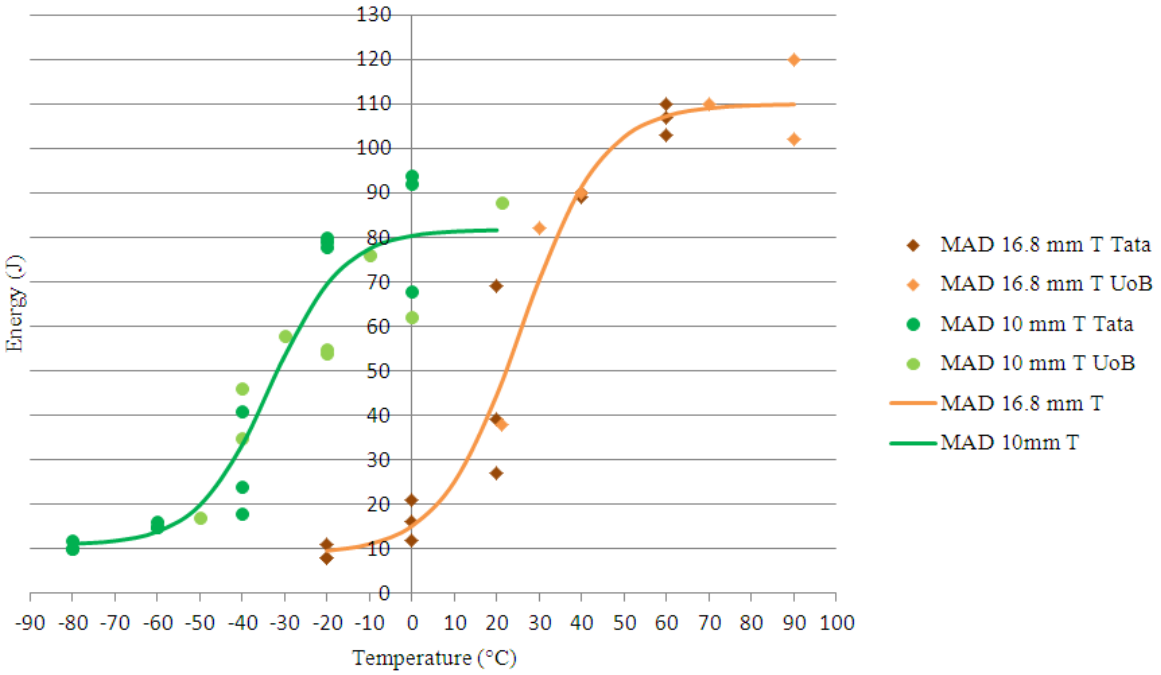

Figure 6.1. Charpy ITT curves for MAD 10 and 16.8 mm thick transversely oriented samples. Comparison between Tata Steel and the University of Birmingham (UoB) tests.

Splits were observed to be present on the fracture surfaces of the majority of specimens as shown in Figure 6.2. Splits on the fracture surface of the 10 mm thick transversely oriented specimens visually appeared sharper and more prominent compared to splits on the fracture surfaces of the 16.8 mm thick transverse specimens. When the splits for the 10 mm thick longitudinally and transversely oriented samples occurring on the upper shelf are compared, the splits are visually sharper in the longitudinal orientations, with the transverse specimens at 90 °C starting to lose split formation (splits become shallower and less defined), as main fracture becomes dominant.

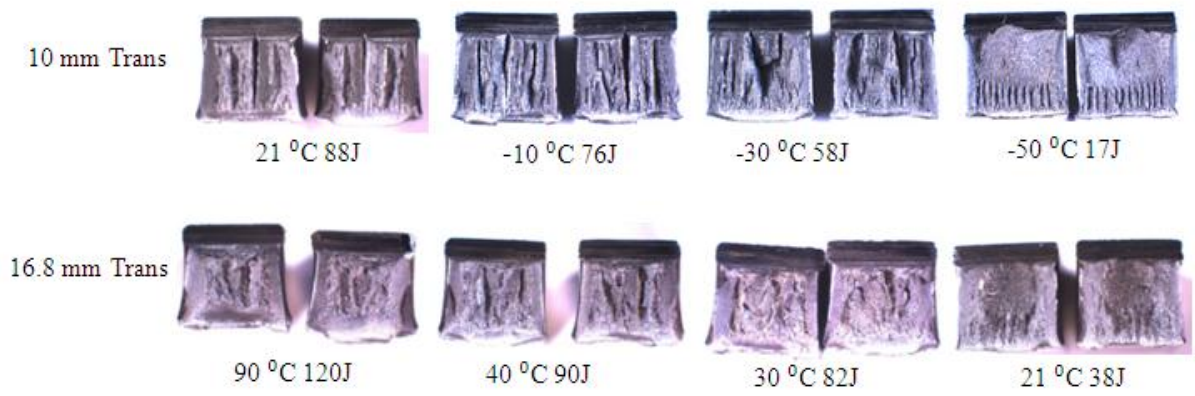

Figure 6.2. Macro-images of the 10 and 16.8 mm thick strip fracture surfaces tested in the transverse orientation.

6.3. **Low blow testing for the 16.8 and 10 mm thick MAD strips in the transverse orientation**

Low blow Charpy testing was carried out on specimens in the transverse orientation from the 10 and 16.8 mm thick strips for comparison against the longitudinal specimens. Low blow tests were carried out at room temperature for the 10 mm thick strip in longitudinal and transverse orientations as well as the 16.8 mm thick strip in the longitudinal orientation as, at that temperature, the material behaviour is upper shelf or near upper shelf. Low blow tests had to be carried out at slightly higher temperatures for the 16.8 mm thick strip in the transverse orientation as, at room temperature, the material in this orientation is in the lower transition region. For the 16.8 mm thick strip low blow tests were carried out at temperatures of RT, 30 and 50 ^{0}C, with no splits being observed to form with impact energies less than 100 J (confirmed by subsequent sectioning), Figure 6.3. At a test temperature of 50 ^{0}C splits were observed to be present after low blow hits with 115 and 120 J, however the main crack also initiated. For the 16.8 mm thick strip in the transverse orientation it was not possible to produce splits without the main crack also being initiated, as shown in Figure 6.4.

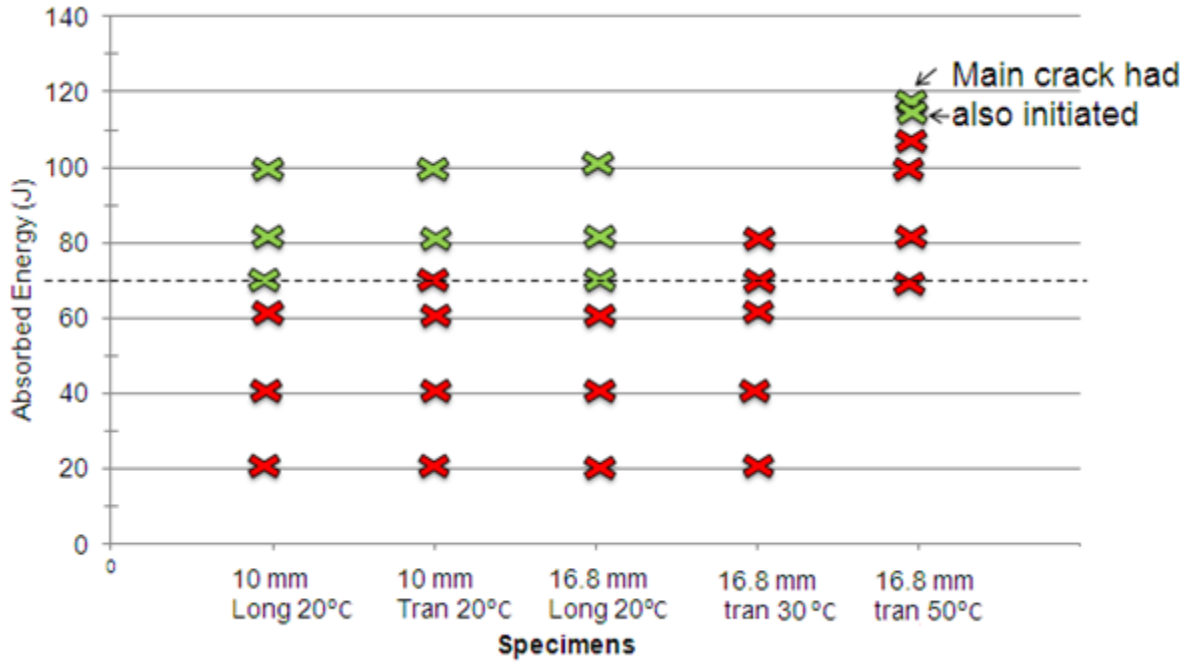

Figure 6.3. Graph showing low blow tests and when splits were initiated for the 10 and 16.8 mm thick strip tested in the longitudinal and transverse orientations (crosses indicate hit with red representing no splits and green indicating splits).

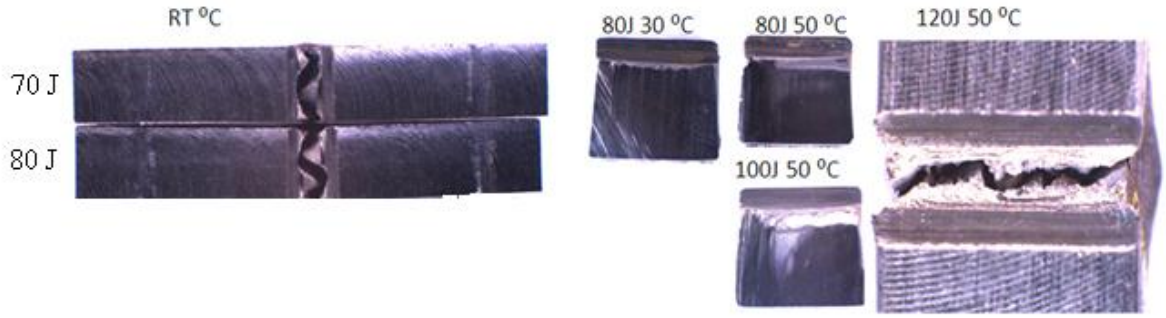

Figure 6.4. Charpy samples after the low blow hits carried out on the 16.8 mm thick strip in the transverse orientation; the sectioned samples at 30 °C (80 J) and 50 °C (80 and 100 J) show no splits formed.

Table 6.2 and Figure 6.3 confirm the presence of splits in samples after low blow hits for the 10 mm thick strip transversely oriented at energies of 80 and 100 J, with no splits being present at impact energies ≤ 70 J. No splits were noted after the low blow test carried out at

20- 110 J in the 16.8 mm thick transverse strip specimens, with splits forming at 115 and 120 J, although main cleavage extension had also occurred.

Table 6.2. Summary of splits seen during low blow hits, carried out on the 10 and 16.8 mm thick strips in the transverse orientation (multi values indicate number of splits present).

Sample (thickness, mm and orientation)	**Impact energy (J)**	**Split length from optical microscopy (mm)**	**Split depth from optical microscopy (mm)**
10.0 trans	80	2.8, 2.7, 0.7	2.1, 1
10.0 trans	100	3.9, 3.8, 2.1, 1.3, 0.9	2.3, 4.9, 1.1
10.0 long	70	3.5	5.8
10.0 long	80	4.4	4.8
10.0 long	100	4.3	5.4
16.8 long	70	2.9	3.4
16.8 long	80	4.2	3.6
16.8 long	100	3.5	3.4

Figure 6.5 shows macro images and optical microscopy images of the splits seen in the 10 mm thick transverse strip samples tested at 80 and 100 J impact energies. They show that more than one split had initiated, although these tests were carried out at 91 % and 114% of the upper shelf energy for the 80 and 100 J hit respectively. Both specimens did not fully break, as the fracture energy would need to be higher to do so.

The low blow hits carried out in the 10 mm thick transverse orientation strip samples at a low blow hit of 80 J, contained a large number of voids near the split initiation sites as well as

larger voids, shown in Figure 6.6, compared to the 100 J hit. This could be due to the fact that at 100 J the smaller voids have developed into larger voids, whereas at 80 J there is simply not enough energy. Some of these voids were seen to initiate in bands of 2nd phase, with voiding seen where TiN / complex TiN inclusions are present.

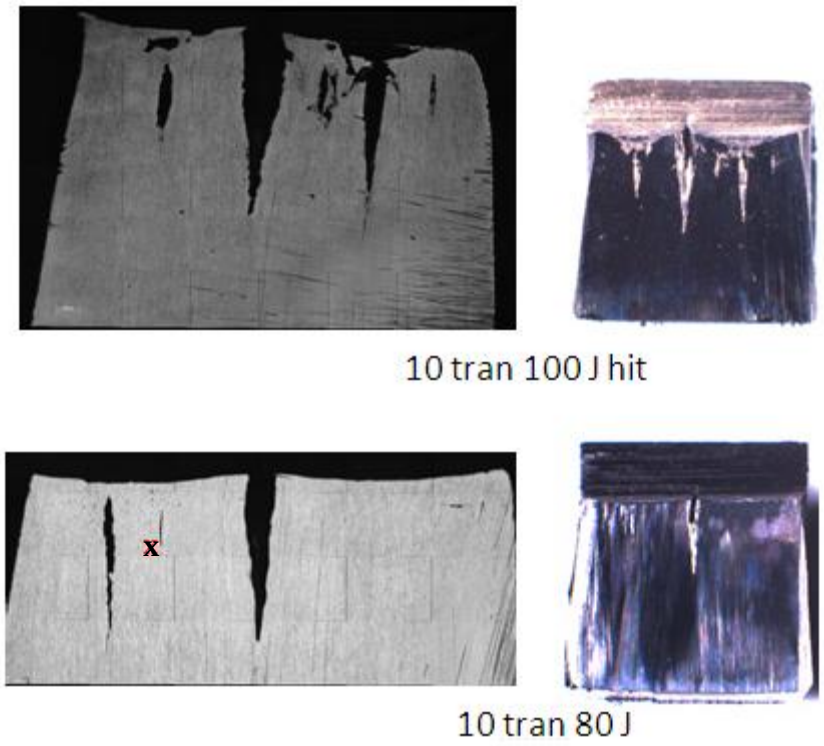

Figure 6.5. Microscopy and macro images of a 80 and 100 J low blow hit carried out on the 10 mm thick transverse strip specimens.

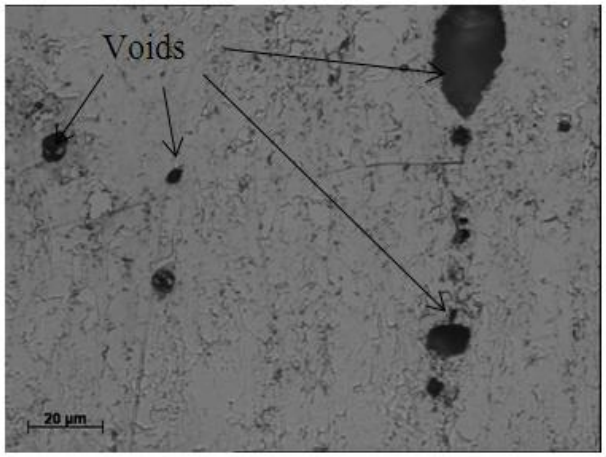

Figure 6.6. Microscopy image from the 10 mm thick transverse strip specimen impacted with an 80 J low blow hit, showing the presence of voids located in the 2nd phase. The ‘x’ in Figure 6.5 highlights where this image was taken in relation to the splits.

For the fully broken Charpy samples (Table 6.3) the splits were measured to be deeper in the longitudinal specimens than those in transverse orientations. The length was similar for most of the specimens, except for the 16.8 mm transverse samples where they were shorter in length. The splits in the longitudinal orientations are sharper (deeper and thinner) than splits in the transverse orientation.

Table 6.3. Summary of length and depth of splits seen on the fully broken Charpy fracture specimens, on the upper shelf for the 10 and 16.8 mm thick strip in the longitudinal (L) and transverse (T) orientations.

Sample	**Energy absorbed, (J)**	**Test temperature (°C)**	**Split length from optical microscopy (mm)**	**Split depth from optical microscopy (mm)**
16.8 L	100	RT	5.7, 5.9, 3.7	3, 5.9, 3
10 L	114	RT	5.3, 6.2, 5.2	3.2, 5.2, 1.6
16.8 T	110	70°C	3.9,5.4,3.6	3, 3.6, 1.2
10 T	88	RT	6, 7.4, 6.1, 5.2	1.1,2.3,5.2,2.6

The importance of the coarse grained patches and the aspect ratio of the patches was identified when analysing split formation and ITT difference between the 10 and 16.8 mm thick strip samples in the longitudinal orientation. A difference between the coarse patches has been identified for the four different specimens (10 mm thick longitudinal and transverse and 16.8 mm thick longitudinal and transverse samples), Table 6.1. Approximately 50% of the grain structure in the 16.8 mm thick strip was coarse grained and these patches in the longitudinal orientation had the lowest aspect ratio. The least fraction of coarse patches was seen in the 10 mm thick strip (the difference between the longitudinal and transverse orientations is 5%, which is within the scatter of experimental measurements). Coarse grain

patches were measured along the length of the split cracks after low blow testing, shown in Table 6.4. It can be seen from Table 6.2 that generally the low blow hits in the 10 mm transverse orientation samples produced more splits, although they were not as deep as in the longitudinal orientation. This may be due to the low blow hit being a greater % of the failure energy and the slightly higher % of coarse patches in transverse specimens, with lower aspect ratio, giving greater split initiation but less propagation (and hence stress relief through the relaxation of plain strain constraint).

Table 6.4 summarises the % of coarse grained patches along the split length, which agrees with the results found in the study of splits between thicknesses in that the splits seek out and propagate through the coarse grain patches. The proportion of coarse grain patches along the length of the splits was measured for the low blow 80 J impact energy tests on the 10 mm thick transverse strip samples and it was found that for the two splits measured they propagated through 68 and 78 % coarse grained microstructure, compared to 15 % seen in the overall microstructure. It was not possible to measure the proportion of coarse grained patches around the centre split in the 10 mm thick transverse 80 J or 100 J hit samples as the splits were well formed and wide which resulted in distortion around the splits. It was also noted that the smaller split lengths (splits which have just begun to form), contain a high amount of coarse patches (for example the 0.7 mm split length in the 10 mm thick transverse 80 J low blow hit strip sample propagated through 78 % coarse grained patches); it is unclear whether this is from statistical sampling or whether the initiation and early propagation stages are very strongly influenced by the coarse grained regions.

Table 6.4. Amount of coarse grain patches measured around the split cracks compared to the amount of coarse grained areas in the overall microstructure.

Strip thickness (mm) and orientation	**Low blow Charpy impact energy (J)**	**Coarse grain patches (%) around split**	**Coarse grain patches (%) in bulk microstructure**	**Split length (mm)**
16.8 Long	100	61	42	3.5
16.8 Long	80	70	42	4.2
10.0 Long	100	59	11	4.3
10.0 Long	80	73	11	4.4
10.0 Trans	80	68	15	2.7
		78	15	0.7
		-	15	2.8
10.0 Trans	100	-	14	3.9, 3.8, 2.1, 1.3, 0.9
16.8 Trans	No splits	-	50	-

6.4. **Summary of section 6**

Low blow Charpy impact tests produced splits in the 10 mm thick transverse strip specimens but not the 16.8 mm thick transverse strip specimens. The splits formed in the low blow tests in the 10 mm thick transverse strip for impact energies above ≥80 J, which was 10 J higher than the energy required to form splits in the 10 and 16.8 mm thick longitudinal strip specimens. The formation of splits required a higher percentage of the total energy to fracture in the 10 mm thick transverse strip specimens: 93 % of the total fracture energy was required compared to 58 and 56 % for the 10 and 16.8 mm thick longitudinal strip specimens respectively. Low blow hits were carried out on the 16.8 mm thick transverse strip specimens between 63 - 90 % of the total fracture energy (70 - 100 J low blow hits) with no splits being observed at a test temperature of 50 ^{0}C (upper shelf temperature). It was noted that splits did not form until 93 % of the fracture energy for the 10 mm thick transverse strip specimens, so that low blow hits were carried out at 110, 115 and 120 J for the 16.8 mm transverse

specimens, corresponding to 99, 104 and 108 % of the average total fracture energy, which resulted in splits forming in the 115 and 120 J hits although the main crack also formed.

In summary, a higher percentage of the fracture energy is required for split formation in the transversely oriented specimens compared to the longitudinally oriented specimens. The 10 mm thick transverse strip samples produced more splits during the low hit testing compared to the 10 and 16.8 mm thick longitudinal strip samples, although the tests were carried out at a higher percentage of the total fracture energy. The main difference between the strip thicknesses is the amount of coarse grained patches present and the aspect ratio of these, with the 10 mm thick longitudinal strip specimens containing the highest aspect ratio and lowest percentage of coarse grained patches. It was found that a high percentage of coarse grains with a low aspect ratio can lead to main crack failure without significant split formation, which was seen in the 16.8 mm thick transversely oriented strip specimens. As shown by the 10 mm thick transverse strip low blow hit results, more splits initiate on the low blow hits, but as the coarse grain patches are not as elongated as in the 10 mm thick longitudinal strip samples, the splits are not as deep and they have less of an effect on lowering the ITT. Therefore the main cause of deep splits forming, with a consequent improvement in ITT, is the presence of a low percentage of coarse grains in patches that have a high aspect ratio.

7. **STEEL X**

A 15 mm thick HSLA strip steel, produced by a different steel producer, was analysed to determine if any splits that formed affected the toughness properties in a similar manner to the Tata Steel produced strip. The composition of the steel strip, termed Steel X, is given in Table 7.1 and the yield stress and tensile strength values in Table 7.2. Steel X has lower yield stress and tensile strength values than the 16.8 mm thick MAD strip in both longitudinal and transverse orientations, but has a higher hardness value, Figure 7.1. It is unclear why the differences in strength and hardness values are opposite and may indicate some scatter in properties. It should be noted that the strength values were provided by Tata Steel measured from a different strip position than the hardness values, and it is known that there is property variation along a strip length from strip products. This is shown by the data sent from Tata Steel for the yield stress and tensile strength values for different positions on their strip products. The MAD composition rolled to a thickness of 13 mm has yield stress and tensile strength values of 738 and 843 MPa respectively at the head of the strip; 681 and 775 MPa in the middle and 707 and 798 MPa at the tail of the strip, all in the longitudinal orientation. There is not a large difference between the two strip steel of MAD 13 mm and the 15 mm steel X for strength values, both are produced to the same strength specification.

Table 7.1. Strip composition in wt % and ppm for Steel X, * indicates values in ppm.

	N*	Al	B*	C	Ca	Cr	Cu	Mn	Mo	Nb	Ni	P	S	Si	Sn	Ti	V
Steel X	50	0.038	3	0.049	23	0.389	0.010	1.89	0.006	0.079	0.255	0.014	0.002	0.326	0.002	0.102	0.011

Table 7.2. Yield stress and tensile strength values of Steel X compared with MAD 16.8 mm thick strip (data from Tata Steel U.K Limited).

	Yield stress Long (MPa)	Tensile strength Long (MPa)	Yield stress Trans (MPa)	Tensile strength Trans (MPa)
16.8 mm MAD	685	787	758	812
15 mm Steel X	638	764	728	797

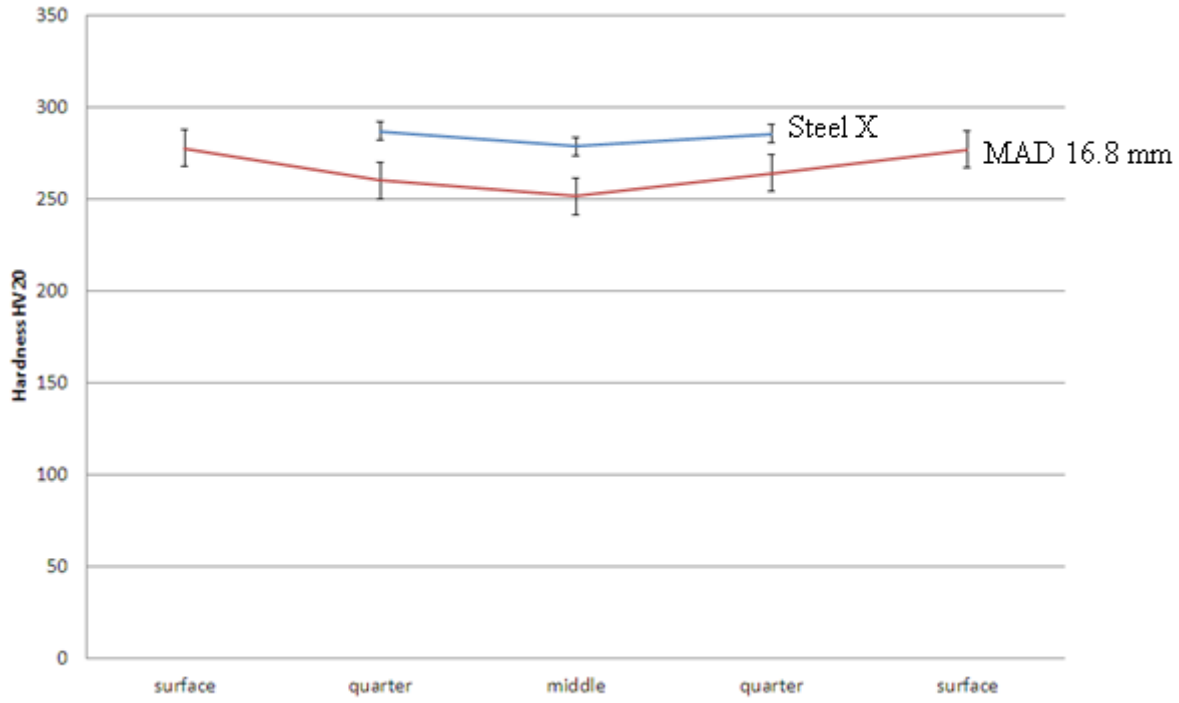

Figure 7.1. Hardness values for Steel X and the 16.8 mm thick MAD strip.

7.1. **Steel X Microstructure**

The microstructure of Steel X, Figure 7.2, is similar to that seen for the other strip steels in this study. It consists of a ferrite structure, with an average ECD of 3.99 µm, with a small amount (< 1%) of 2nd phase. The microstructure contains elongated grains in the longitudinal orientation, with the grains banded into fine and coarse patches (same ferrite grain size criterion applies in separating these for Steel X as for MAD). The area % of coarse grain

patches is 24%, which is higher than that seen in the 10 mm thick MAD strip (11%) but not as high as that seen in the 16.8 mm thick MAD strip (42%), both in the longitudinal orientation.

The aspect ratio of the individual grains in Steel X does not show any significant difference between the fine and coarse grains (2.27 and 2.47 respectively), which is similar to that seen for the MAD 10 mm and 16.8 mm thick strip (section 6.1). The aspect ratio of the coarse patches is 3.1, which is lower than that for the MAD 10 mm thick strip (4.0) but higher than that for the MAD 16.8 mm thick strip (2.0) indicating that the patches give an overall elongation between that observed in the Tata Steel supplied strips.

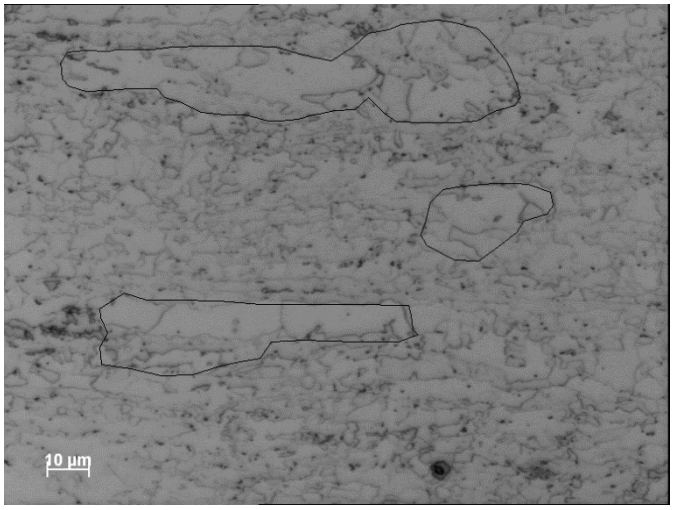

Figure 7.2. Optical micrograph of Steel X in the longitudinal orientation showing coarse grain patches (outlined).

7.2. **TiN inclusions**

Coarse TiN / complex TiN inclusions (≥0.5 µm) were observed in Steel X and are shown in Figure 7.3. The TiN size distribution is shown in Figure 7.4 along with that for the 10 and 16.8 mm thick MAD strip. The data are summarised in Table 7.3 and show that the TiN are within the same size range for all steels, but that Steel X contains more coarse TiN inclusions

in the 3.0 – 7.5 µm size range. The number density peaks are for a size of around 1.6 and 2.2 µm for the 16.8 and 10 mm thick MAD strip respectively, whereas Steel X shows a peak at 4.0 µm. The largest TiN inclusion size seen in Steel X matches that seen for the 10 mm thick MAD strip, which is 9 µm. The higher number density of coarser TiN inclusions observed for Steel X agrees with the presence of more Ti in the Steel X composition (0.102 wt %) compared to the 10 mm and 16.8 mm thick MAD strips (0.089 wt %), with a similar amount of nitrogen present in all steels.

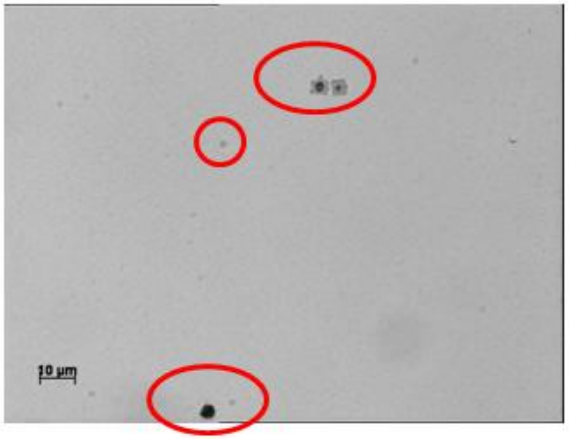

Figure 7.3. Micrograph showing the presence of complex TiN inclusions in Steel X.

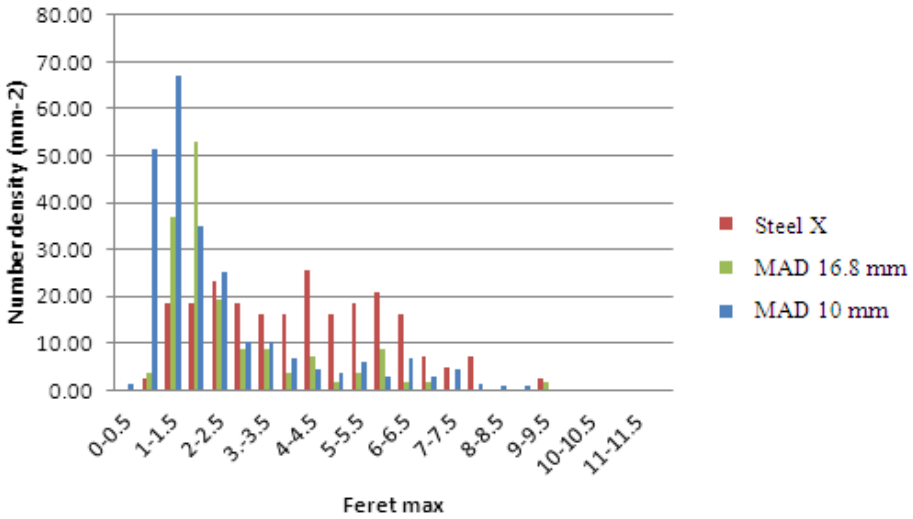

Figure 7.4. Number density for coarse TiN (≥0.5 µm) in Steel X and the 16.8 and 10 mm thick MAD strips.

Table 7.3. Summary of TiN inclusion size and number density for Steel X compared to the 16.8 and 10 mm MAD strips.

Strip composition and thickness (mm)	Average Feret max. (µm)	Feret max. range (µm)	Number density (mm^{-2})
MAD 10.0	2.2	0.5 - 9.0	241
MAD 16.8	1.6	0.5- 9.5	159
Steel X 15	4.0	0.8 – 9.0	233

7.3. **Charpy impact Curves**

Figure 7.5 and Figure 7.6 show the Charpy transition curves for Steel X in the longitudinal and transverse orientations respectively. On each graph the transition curve for the MAD 10 and 16.8 mm thick strips for each orientation are present for comparison.

Table 7.4 contains a summary of the ITT and upper shelf energy values for Steel X and the 10 mm and 16.8 mm thick MAD strip steels. It can be seen that Steel X has a lower ITT than the 16.8 mm thick MAD strip with a difference of 16 and 26 °C noted for the longitudinal and transverse orientations respectively at 40 J. When compared to the 10 mm thick MAD strip the difference in ITT is 63 and 42 °C for longitudinal and transverse orientations respectively, showing a larger difference then that seen with the thicker strip.

The upper shelf energy value is lower for Steel X when compared to the MAD 16.8 mm strip. A difference of approximately 34 J in noted in the transverse orientation. The difference between Steel X and the 10 mm thick strip is 9 J for transverse orientation. It is difficult to determine the upper shelf from the Charpy transition curve for Steel X longitudinal, as the impact values did not reach a clear upper shelf by the maximum temperature tested, so no

correlations can be made for upper shelf. The higher number density of large TiN would be expected to give a lower USE as would higher proportions of larger grains.

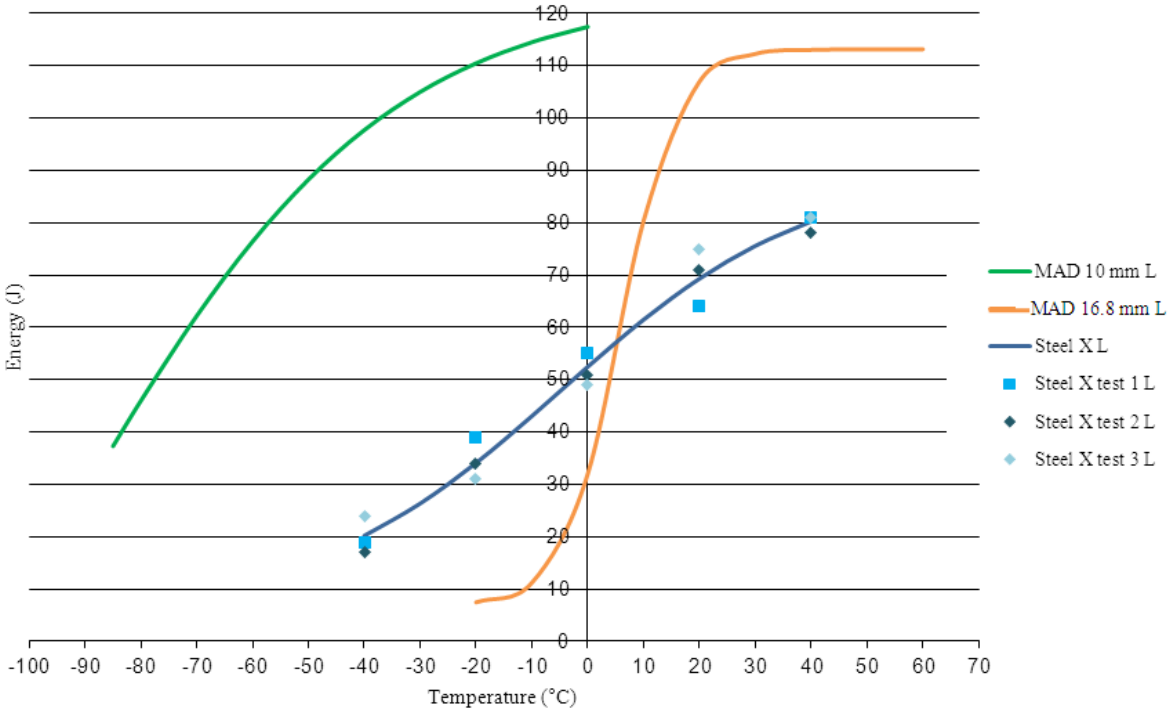

Figure 7.5. Charpy transition curves for Steel X and MAD 16.8 mm thick strip in the longitudinal orientation (data from Tata Steel U.K. Limited).

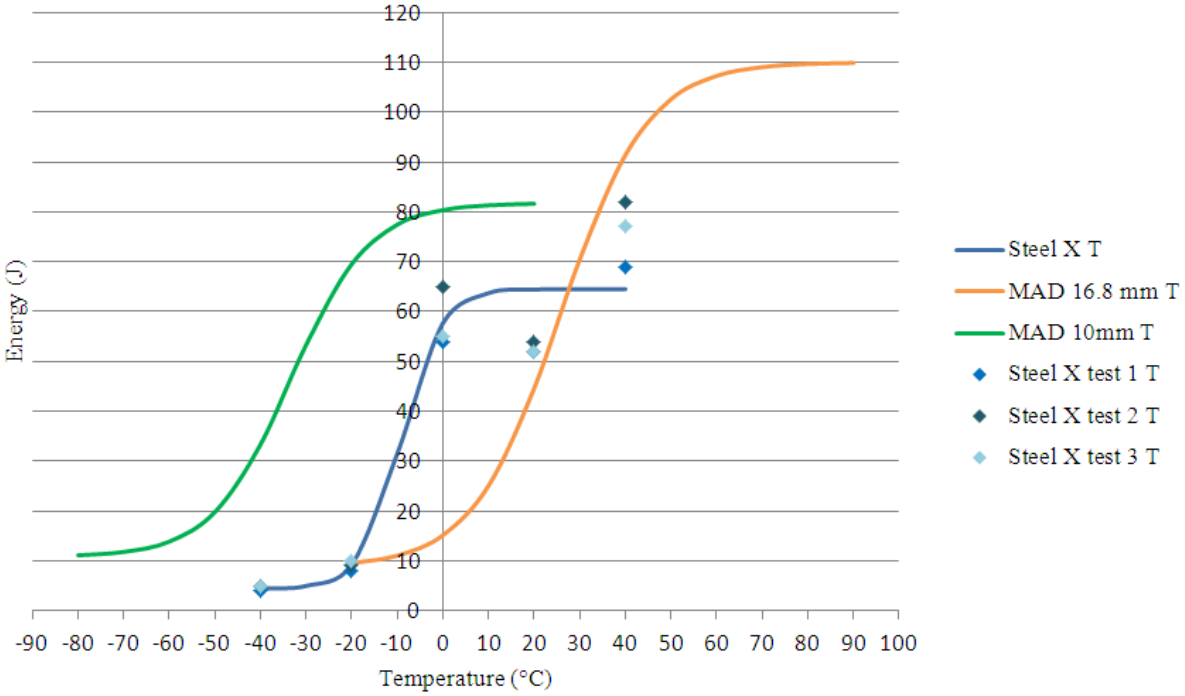

Figure 7.6. Charpy transition curves for Steel X and MAD 16.8 mm thick strip both in the transverse orientation (data from Tata Steel U.K. Limited).

Table 7.4. Summary of ITT values and upper shelf energies for Steel X, the 10 mm and 16.8 mm MAD strip steels.

Strip composition, thickness (mm) and orientation	**40 J ITT (^{0}C)**	**Upper shelf energy (J)**
Steel X 15 long	-13	n/a
Steel X 15 trans	-8	77
MAD 10 long	-80	120
MAD 10 trans	-34	86
MAD 16.8 long	3	113
MAD 16.8 trans	18	111

Images of the fracture surfaces for Steel X are shown in Figure 7.7 for the longitudinal orientation. Splits become obvious on the fracture surfaces at a Charpy test temperature of 0 °C in the upper transition region. A small split crack can also be seen on the fracture surface of the sample tested at -20 °C (lower transition region). This behaviour is consistent with the observations made for the 10 mm and 16.8 mm thick MAD strip samples and that reported in the literature where splits are most commonly observed in the upper transition region and upper shelf (77). The fracture surfaces for the 10 and 16.8 mm thick MAD strip steels showed three splits around the upper transition and upper shelf (section 6.2). Steel X seems to show around 4- 5 splits on the fracture surface in the same region of the Charpy curve, Figure 7.7.

Figure 7.7. Charpy impact fracture surfaces of Steel X in the longitudinal orientation.

7.4. **Fracture Analysis**

Figure 7.8 shows the Charpy impact fracture surface of Steel X tested at 40 ºC, indicating the presence of coarse TiN inclusions in ductile voids. Coarse TiN inclusions were not observed to initiate cleavage fracture in any of the Charpy samples analysed (covering the transition and lower shelf region). This is consistent with the observations made for the 10 mm and 16.8 mm thick MAD strip samples.

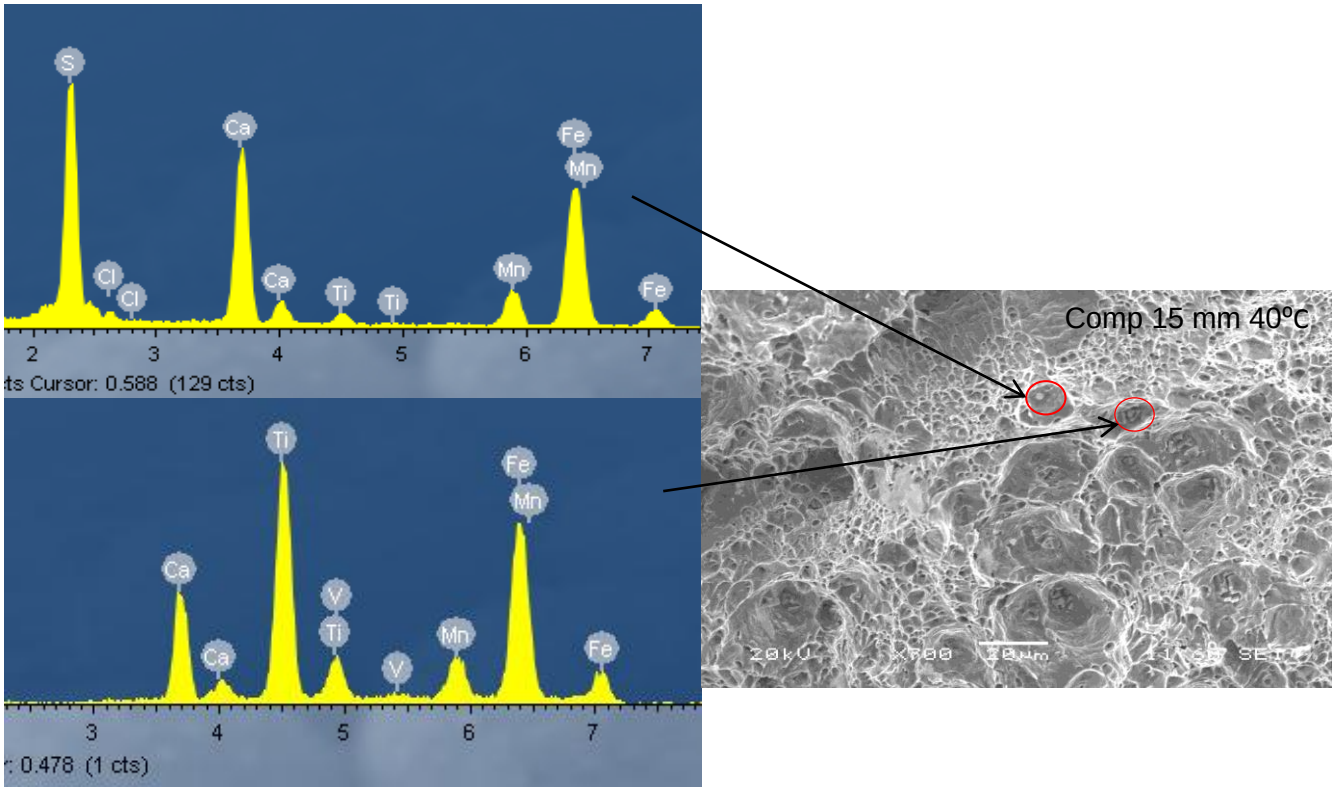

Figure 7.8. EDX spectra for the particles observed on the Charpy impact fracture surface of Steel X tested at 40 °C. Peaks for Mn, S, Ti and Ca are observed indicating that the inclusions are complex, probably consisting of TiN and (Mn,Ca)S.

4.1 **Steel X - Texture / Mis-orientation**

The texture of Steel X was measured, Figure 7.9, and it can be seen that no strong texture is present in the strip, consistent with the observations for the 10 mm and 16.8 mm thick MAD strip steels (section 5.3.1). Any difference in texture between the coarse and fine patches was

also analysed, Figure 7.10, with no significant difference being noted, which again matches the results obtained for the MAD composition strip steels. Figure 7.11 shows the misorientation angles for Steel X and the MAD 16.8 mm thick strip steel. No significant differences are noted between the two graphs, indicating that any difference in properties between the steels is not due to differences in misorientation angles.

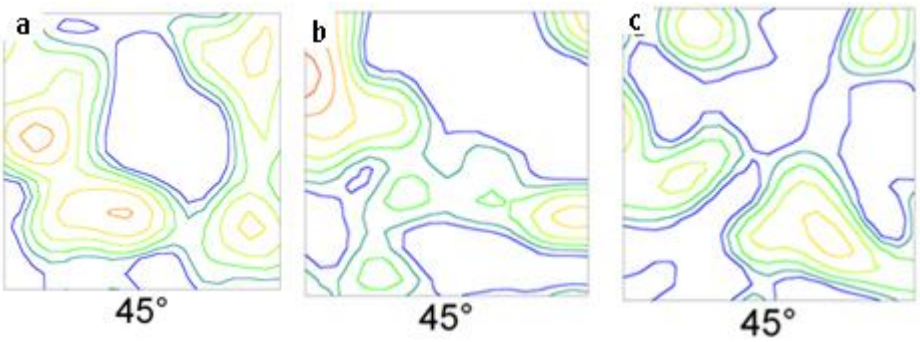

Figure 7.9. ODF graphs for a) Steel X 15 mm strip, b) MAD 10 mm strip and c) 16.8 mm strip (data from Tata Steel U.K. Limited).

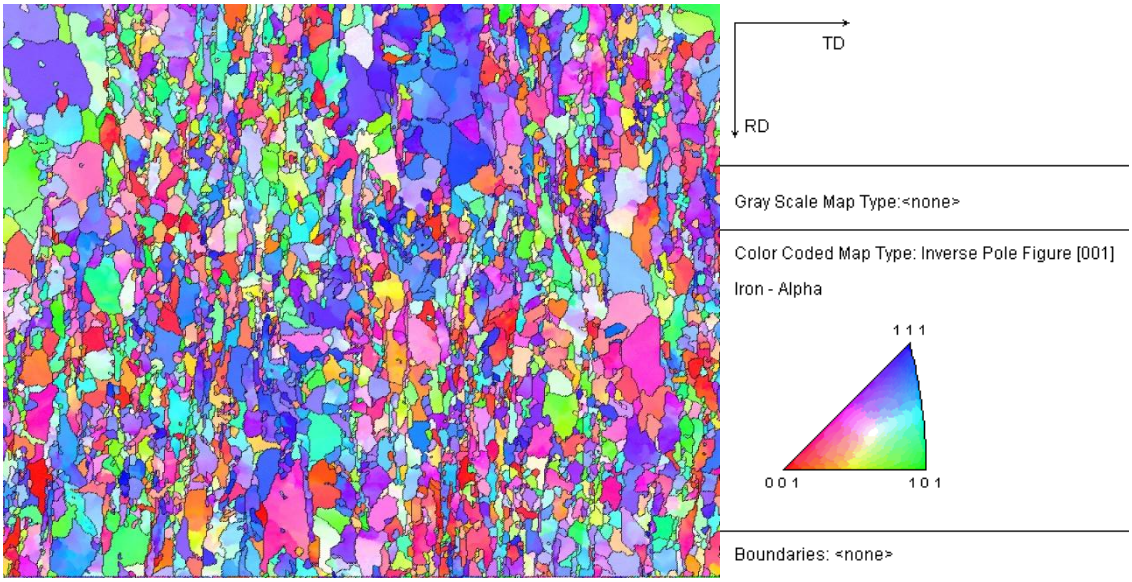

Figure 7.10. Inverse Pole Figures (IPF) analysis, carried out at the ¾ thickness position, with a 5° misorientation, for steel X taken in the longitudinal orientation (data from Tata Steel U.K. Limited).

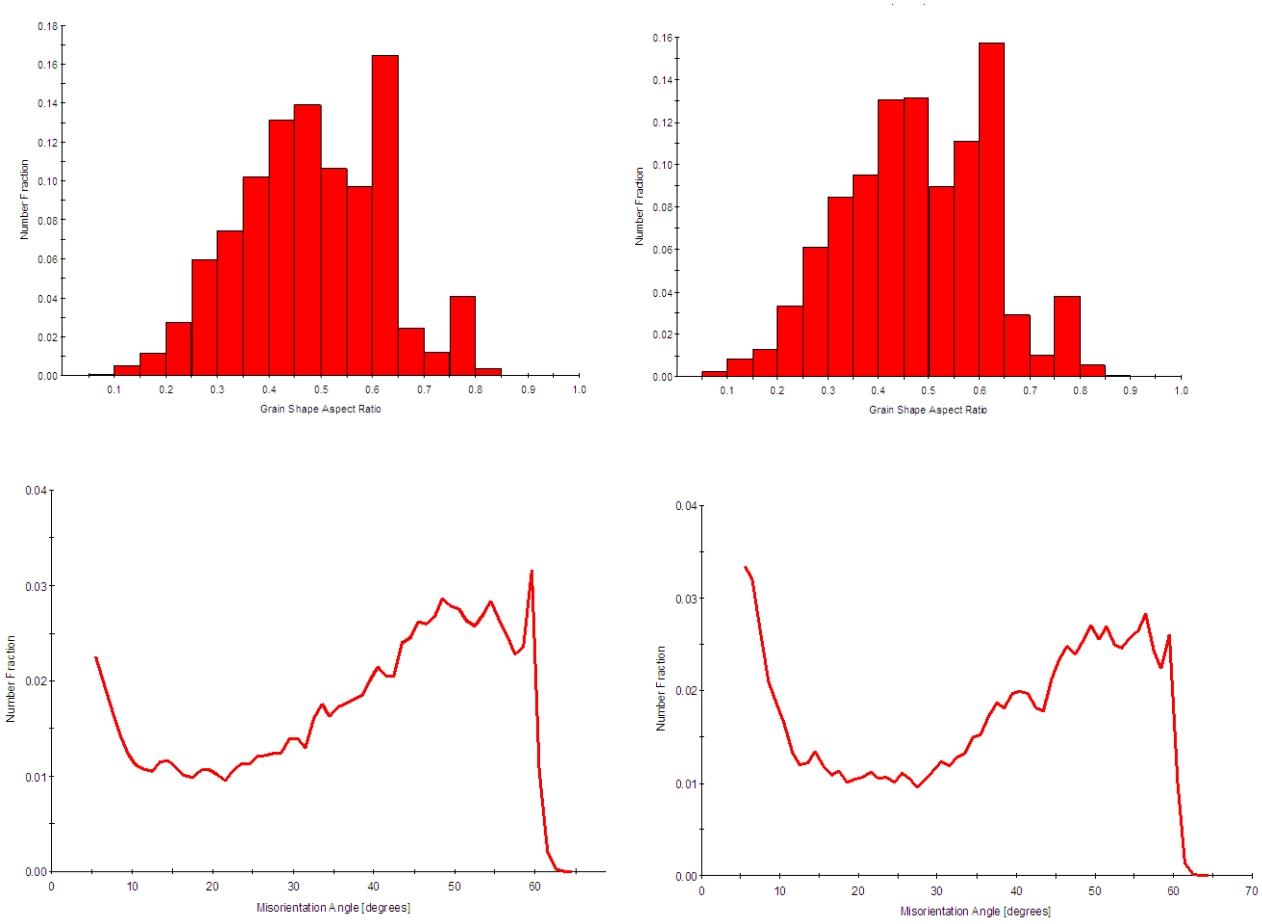

Figure 7.11. Misorientation angles for Steel X and the MAD 16.8 mm thick strip (data from Tata Steel U.K. Limited).

7.5. **Splits in Steel X**

X-ray tomography was carried out on the broken Charpy specimens tested in the longitudinal orientation corresponding to the upper shelf, Figure 7.12. Table 7.5 summarises the length and depth values of the splits observed for the Steel X, 10 mm MAD and 16.8 mm MAD thick strip samples, all tested in the upper shelf region (fully broken 300 J impact tests), and shows that similar split lengths and depths were seen for the 10 mm and 16.8 mm thick MAD strip specimens. Steel X, however, showed the longest and deepest split cracks. Steel X showed the presence of four well-developed splits, whilst the other samples only contained three splits cracks.

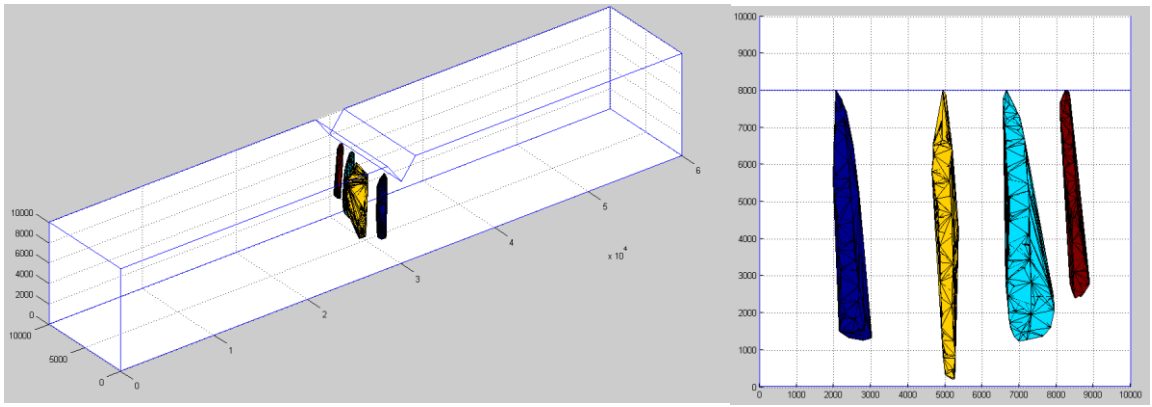

Figure 7.12. 3-D image of the split crack generated using a MATLAB model for a Charpy tested Steel X longitudinal orientation sample (tested at 40 °C).

Table 7.5. Comparison table of length and depth of splits measured by X-ray tomography on a fully fractured 300 J hit specimens tested in the upper shelf region for MAD 16.8 and 10 mm thick longitudinal strip samples and Steel X.

Sample composition and thickness (mm)	**Split length from X-ray tomography (mm)**	**Split depth from X-ray tomography (mm)**
MAD 16.8	5.0, 6.0, 4.0	4.2, 5.4, 3.2
MAD 10	5.4, 7.1, 4.1	3.4, 5.4, 3.0
Steel X 15	6.8, 5.6, 7.8, 6.8	4, 3, 6.2, 4.0

7.6. **Summary of section 7**

The microstructure of Steel X (15 mm strip thickness) is similar to that seen for the 10 mm and 16.8 mm thick MAD strip steels, comprising of ferrite with fine and coarse grain patches. Steel X contains an area % of coarse grain patches between that observed for the 10 mm and 16.8 mm thick MAD strip steels and these patches were more elongated then the 16.8 mm strip (24 % and an aspect ratio of 3.1). The strength and hardness values of Steel X were similar to those of the 10 mm and 16.8 mm thick MAD steels. Steel X contained a higher

number density of coarser TiN particles than the 10 mm and 16.8 mm thick MAD strip steels consistent with its higher Ti content. However, no evidence of TiN particles initiating cleavage fracture was observed. No significant difference was noted for Steel X compared to the 10 mm or 16.8 mm thick MAD strips in terms of texture or grain misorientation.

The Charpy 40 J ITT of Steel X values (-13 °C in the longitudinal orientation and -8 °C in the transverse orientation) are higher than those for the 10 mm thick MAD strip (-80 °C in the longitudinal orientation and -34 °C in the transverse orientation) but lower than those for the 16.8 mm thick MAD strip (3 °C in the longitudinal orientation and 18 °C in the transverse orientation). The fracture surfaces of the upper shelf samples of Steel X contained 4 - 5 well-developed splits compared to only three splits being observed for the upper shelf fracture surfaces of the MAD 16.8 and 10 mm thick samples. The splits seen for Steel X appear to be a little deeper than those observed for the 16.8 and 10 mm thick MAD strip samples.

The observations for Steel X are consistent with those for the MAD 10 mm and 16.8 mm thick strip steels, with splits being formed due to the presence of elongated coarse grain patch regions. The higher aspect ratio of coarse grain patches for Steel X compared with the 16.8 mm thick MAD strip steel would suggest, based on the results presented in section 8, that splits form more readily, which would explain the improved toughness of this steel. However, the higher aspect ratio of the coarse grain patches in the 10 mm thick MAD strip steel, and hence greater propensity for split crack formation, explains the significantly improved toughness of this steel.

8. **CONCLUSIONS**

Three high strength strip steels ranging from a thickness of 10 mm to 17 mm have been examined. The steels had a yield stress of ~700 MPa and contained microalloying additions of titanium, niobium, vanadium and molybdenum. The microstructure and mechanical properties (strength, hardness and toughness) have been assessed. The main conclusions from the work are as below:

- The three strip steels considered, had similar compositions (small variations in the microalloying elements of Nb, Ti and Mo were present, Nb: 0.064 - 0.068 wt%, Ti: 0.066 - 0.089 wt%, and Mo: 0.019 - 0.182 wt%), and were found to have similar microstructures and mechanical properties for the same strip thicknesses. For all the strip compositions it was found that the thinner (10 mm) strips had lower impact transition temperature (ITT) values compared to the thicker (~ 17 mm) strips and the longitudinal oriented samples had lower ITTs than the transverse oriented samples.
- The microstructure of the strip steels comprised of polygonal ferrite grains with a small amount of 2^{nd} phase (pearlite / bainite), less than 1 %, grain boundary carbides and inclusions such as MnS, TiN and Al_2O_3. Coarse and fine grained patches are present, with coarser and a higher percent of patches observed in the thicker strips. No significant difference was noted between grain boundary misorientation angles for the fine and coarse grained patches for the 10 mm and 16.8 mm thick MAD strips.
- TiN particles were found at cleavage initiation sites, although they did not have a significant effect; this was consistent with work carried out by Du et al. (64).
- The maximum difference in ITT values between the 10 mm thick strip and the 16.8 mm thick strip in the longitudinal orientation was estimated to be 80 °C. The 10

mm thick strip also had a lower 40 J ITT in the transverse orientation (by 60 °C) compared to the 16.8 mm thick strip.

- On average, three splits were observed on the broken Charpy fracture surfaces for all samples (samples tested from the different thickness strip and in different orientations) in the upper transition region. The splits were consistently deeper in the 10 mm thick strip samples in both orientations compared to the thicker (16.8 mm) strip.
- Acoustic emission monitoring along with X-ray tomography can be used to detect the formation and characterise splits, respectively, formed during room-temperature low blow Charpy impact testing, where impact energies less than those required to cause main crack propagation were used. In the longitudinal orientation for both 10 and 16.8 mm strips, splits were observed during low blow impact testing with an impact energy above 70 J (56 and 58 % of the total fracture energy for the 16.8 and 10 mm strip respectively). No splits were observed at lower impact energies for the longitudinal orientations of the 10 and 16.8 mm strip. For the transverse orientation splits were observed on testing the 10 mm thick strip with an impact energy above 80 J (93% of the total fracture energy), for the 10 mm transverse specimen. However, no splits were observed for the 16.8 mm thick strip transverse specimens during low blow impact testing before main crack propagation.
- The strip steels showed weak crystallographic texture and no alignment of carbides or elongated MnS inclusions; these features were previously reported to influence split formation by previous authors. Therefore, these factors were not responsible for the difference in toughness between the MAD 10 and 16.8 mm strips.

- In all specimens the first split to form did so in the middle of the sample at the base of the notch, which is the area of highest stress. If other splits were present they formed on either side of the first split.
- Splits were found to be brittle in nature, propagating by transgranular cleavage and preferentially following the coarse grain patches in the microstructure, with the 10 mm strip producing deeper splits. The main microstructural difference between the strip thicknesses was found to be the amount of coarse grained patches present and their aspect ratio, with the 10 mm thick longitudinal strip specimens containing the highest aspect ratio (4.0) and lowest percentage (11 %) of coarse grained patches. It was also found that a high percentage (50 %) of coarse grains with a low aspect ratio (2.2) can lead to main crack failure without significant split formation, which was seen in the 16.8 mm thick transversely oriented strip specimens, resulting in a higher impact transition temperature.
- Using the Wallin et al. equation, an approximate 45 °C shift in ITT is predicted due to the formation of three splits in a Charpy specimen. In this work it is proposed that the greater depth of splits in the 10 mm thick strip has a larger effect on reducing the plane strain constraint and, therefore, on decreasing the ITT compared to the shallower splits in the 16.8 mm thick strip.
- The 10 mm thick strip goes through an extra rolling pass (6 compared to 5 for the 16.8 mm strip) and more strain is used in the initial rolling stages. A 16 ^{0}C difference is noted for the final rolling temperature with the thicker strip having the higher temperature. Coarser grains are produced when less rolling is used, with lower strains and a higher finishing rolling temperature. To produce a high aspect ratio rolling in the non-recrystallisation regime is required.

- Overall, for a lower ITT, the formation of splits is beneficial, and these have been found to form before main crack propagation. The initiation of split cracks appears to require some plastic deformation ahead of the notch (as no splits are seen for impact energies less than approximately 70-80 J), and so will only form in the upper transition region. Splits have been found to initiate and propagate in coarse grained patches, therefore requiring a microstructure of mixed fine and coarse grains with the coarse grains occurring in patches. However, it has been found that if the percentage of coarse grains is too high and they are not elongated (for example in the 16.8 mm thick strip containing 50 % coarse grains with a patch aspect ratio of 2.2), then the splits are less deep and there is less benefit on toughness. In addition the larger average grain size is known to have a detrimental effect on overall toughness and main crack propagation.

9. **FUTURE WORK**

The requirements of industry are to produce thicker strip steels with good toughness. For the high strength strip steel grades considered in this work, comprising of a predominantly fine grained ferritic structure, it has been identified that the presence of coarse grain patches are beneficial to the toughness. Therefore, work is needed to design the rolling schedule to deliver the required amount of coarse grain patches with a high aspect ratio for thicker strip. Niobium is known to segregate during solidification and has been linked to the formation of coarse and fine grain regions in plate steels during thermo-mechanical controlled processing (TMCP), due to variations in grain boundary pinning during reheating and variations in solute / precipitate effects on recrystallisation (12,16). The effect of niobium, and other microalloying elements, in these high strength strip steels needs to be analysed further to establish how they influence the development of microstructure during processing. For example, areas within a fine and coarse grain patch could be analysed by TEM, with specimens prepared by FIB (focused ion beam) to allow targeting of the required areas of interest. The local microalloying element levels and presence of precipitates (e.g. strain induced precipitates) could then be analysed.

Within the Phase Transformation Group at Birmingham University modelling software is being developed to predict the grain size development during TMCP of steels. For example solidification segregation can be predicted and the resultant microalloying element levels used with the Dutta-Sellars equation to predict recrystallisation start and stop temperatures. Further work is required to improve the accuracy of the modelling capability for the microalloying elements seen in the high strength strip steels, and the processing parameters common with strip production. The model could then be used to predict the percentage of

recrystallisation for a given rolling schedule, enabling for the most economic rolling conditions to be carried out to achieve the specific microstructure (certain % of coarse and fine patches, aspect ratio of grains) and hence strength and toughness requirements. This model will then need to be quantified against experimental results.

Further work could also be carried out to both experimentally determine, and theoretically predict, the optimum amount of coarse grain patches, and their morphology, for improved toughness in both the longitudinal and transverse orientations. This can be done by carrying out some finite element modelling to predict the required local mechanical properties of the different regions to model the formation of splits.

Further work could be carried out on the acoustic emissions testing to define if the signal can be separated into the number of splits that form in a Charpy specimen, along with carrying out AE testing at different temperatures so comparisons can be made at the some positions on the ITT curve.

10.**APPENDIX**

10.1. **Code for Matlab programme.**

Used to build up 3D image of the splits using co-ordinates taken from the MicroCT images.

```
clear
clc

Charpy = importdata('Charpy.mat');
A = importdata('comp 20C split1.xlsx');
imagestep=20;
slicedepth=4.35;


Ax=A(1:end,1);
Ax=Ax*4;
Axmin=min(Ax);
Ax=(Ax-Axmin);

Ay=A(1:end,2);
Ay=Ay*4;
Aymin=min(Ay);
Ay=Ay-Aymin;

Az=A(1:end,3);
Az=(Az*(imagestep*slicedepth));



T=atand((max(Ay)-min(Ay))/(max(Ax)-min(Ax)));
T=-T;
Ax1=(Ax.*(cosd(T)))-(Ay.*(sind(T)));
Ay1=(Ax.*(sind(T)))+(Ay.*(cosd(T)));


disp('What Orientation are the coordinates put in?')
disp('1 = XY Orientation')
disp('2 = XZ Orientation')
disp(' ')
Or=input('');
if Or==1;
    Ax=(Ax1-(max(Ax1)/2))+30000;
    disp('XY')
end
if Or==2;
T=-90;
Ax1=(Ax1.*(cosd(T)))-(Az.*(sind(T)));
Az=(Ax.*(sind(T)))+(Az.*(cosd(T)));
Ax=Ax1-(max(Ax1)-30000);
disp('XZ')
end

T=atand((max(Ay1)-min(Ay1))/(max(Az)-min(Az)));
T=-T;
```

```
%x translation
Az=(Az.*(cosd(T)))-(Ay1.*(sind(T)));
Ay1=(Az.*(sind(T)))+(Ay1.*(cosd(T)));

% y translation
Ay=((Ay1+(max(Ax))));
Aydif=(max(Ay)+min(Ay))/2;
Ay=Ay-Aydif+5000;%change for split position

% z translation
Az=Az-max(Az)+9000;%change for split height
Atri = Delaunay3(Ax,Ay,Az);



%%%%%%%%%%%%%%%%%%%%%%%%%%%%%%%%%%%%%%%%%%%%%%%%%%%%%%%%%%%%%%%%%%%%%%%%%%%%
B = importdata('comp 20C split2.xlsx');
imagestep=20;
slicedepth=4.35;


Bx=B(1:end,1);
Bx=Bx*4;
Bxmin=min(Bx);
Bx=(Bx-Bxmin);

By=B(1:end,2);
By=By*4;
Bymin=min(By);
By=By-Bymin;

Bz=B(1:end,3);
Bz=(Bz*(imagestep*slicedepth));




T=atand((max(By)-min(By))/(max(Bx)-min(Bx)));
T=-T;
Bx1=(Bx.*(cosd(T)))-(By.*(sind(T)));
By1=(Bx.*(sind(T)))+(By.*(cosd(T)));

if Or==1;
    Bx=(Bx1-(max(Bx1)/2))+30000;
    disp('XY')
end
if Or==2;
T=-90;
Bx1=(Bx1.*(cosd(T)))-(Bz.*(sind(T)));
Bz=(Bx.*(sind(T)))+(Bz.*(cosd(T)));
Bx=Bx1-(max(Bx1)-30000);
disp('XZ')
end

T=atand((max(By1)-min(By1))/(max(Bz)-min(Bz)));
T=-T;
```

```
%x translation
Bz=(Bz.*(cosd(T)))-(By1.*(sind(T)));
By1=(Bz.*(sind(T)))+(By1.*(cosd(T)));


%y translation
By=((By1+(max(Bx))));
Bydif=(max(By)+min(By))/2;
By=By-Bydif+3000;%change for split position

%z translation
Bz=Bz-max(Bz)+8000;
Btri = Delaunay3(Bx,By,Bz);

%%%%%%%%%%%%%%%%%%%%%%%%%%%%%%%%%%%%%%%%%%%%%%%%%%%%%%%%%%%%%%%%%%%%%%%%%%%%%%%
D = importdata('comp 20C split3.xlsx');
imagestep=20;
slicedepth=4.35;


Dx=D(1:end,1);
Dx=Dx*4;
Dxmin=min(Dx);
Dx=(Dx-Dxmin);

Dy=D(1:end,2);
Dy=Dy*4;
Dymin=min(Dy);
Dy=Dy-Dymin;

Dz=D(1:end,3);
Dz=(Dz*(imagestep*slicedepth));




T=atand((max(Dy)-min(Dy))/(max(Dx)-min(Dx)));
T=-T;
Dx1=(Dx.*(cosd(T)))-(Dy.*(sind(T)));
Dy1=(Dx.*(sind(T)))+(Dy.*(cosd(T)));
if Or==1;
    Dx=(Dx1-(max(Dx1)/2))+30000;
    disp('XY')
end
if Or==2;
T=-90;
Dx1=(Dx1.*(cosd(T)))-(Dz.*(sind(T)));
Dz=(Dx.*(sind(T)))+(Dz.*(cosd(T)));
Dx=Dx1-(max(Dx1)-30000);
disp('XZ')
end

T=atand((max(Dy1)-min(Dy1))/(max(Dz)-min(Dz)));
T=-T;


%x translation
```

```
Dz=(Dz.*(cosd(T)))-(Dy1.*(sind(T)));
Dy1=(Dz.*(sind(T)))+(Dy1.*(cosd(T)));

%y translation
Dy=((Dy1+(max(Dx))));
Dydif=(max(Dy)+min(Dy))/2;
Dy=Dy-Dydif+8000;%change for split position

%z translation
Dz=Dz-max(Dz)+8000;
Dtri = Delaunay3(Dx,Dy,Dz);

%%%%%%%%%%%%%%%%%%%%%%%%%%%%%%%%%%%%%%%%%%%%%%%%
E = importdata('comp 20C split4.xlsx');
imagestep=20;
slicedepth=4.35;


Ex=E(1:end,1);
Ex=Ex*4;
Exmin=min(Ex);
Ex=(Ex-Exmin);

Ey=E(1:end,2);
Ey=Ey*4;
Eymin=min(Ey);
Ey=Ey-Eymin;

Ez=E(1:end,3);
Ez=(Ez*(imagestep*slicedepth));


T=atand((max(Ey)-min(Ey))/(max(Ex)-min(Ex)));
T=-T;
Ex1=(Ex.*(cosd(T)))-(Ey.*(sind(T)));
Ey1=(Ex.*(sind(T)))+(Ey.*(cosd(T)));

if Or==1;
    Ex=(Ex1-(max(Ex1)/2))+30000;
    disp('XY')
end
if Or==2;
T=-90;
Ex1=(Ex1.*(cosd(T)))-(Ez.*(sind(T)));
Ez=(Ex.*(sind(T)))+(Ez.*(cosd(T)));
Ex=Ex1-(max(Ex1)-30000);
disp('XZ')
end

T=atand((max(Ey1)-min(Ey1))/(max(Ez)-min(Ez)));
T=-T;
Ez=(Ez.*(cosd(T)))-(Ey1.*(sind(T)));
Ey1=(Ez.*(sind(T)))+(Ey1.*(cosd(T)));

%y translation
Ey=((Ey1+(max(Ex))));
Eydif=(max(Ey)+min(Ey))/2;
Ey=Ey-Eydif+2000;%change for split position
```

```
%z translation
Ez=Ez-max(Ez)+8000;



Etri = Delaunay3(Ex,Ey,Ez);




h = trisurf(Atri, Ax, Ay, Az, 200);
Hold on
h2=trisurf(Btri, Bx, By, Bz, 0);
h3=trisurf(Dtri, Dx, Dy, Dz, 100);
h4=trisurf(Etri, Ex, Ey, Ez, 300);

Cx=Charpy(1:end,1);
Cy=Charpy(1:end,2);
Cz=Charpy(1:end,3);
plot3(Cx,Cy,Cz)
axis equal
Hold off
```

11.**REFERENCES**

1. Gladman T. The Physical Metallurgy of Microalloyed Steels. London: The Institute of Materials; 1997.

2. Skobir DA. High-Strength Low Alloy (HSLA) Steels. Materials and technology 2011;45(4):295-301.

3. Chakrabarti D. Development of bimodal grain structures and their effect on toughness in HSLA steel. Birmingham, UK: Thesis submitted to The University of Birmingham; 2007.

4. Yi H-l, Du L-x, Wang G-d, Liu X-h. Strengthening Mechanism of a New 700 MPa Hot Rolled High Strength Steel. Journal of Iron and Steel Research, International. 2008;15(2):76-80.

5. Misra RDK, Nathani H, Hartmann JE, Siciliano F. Microstructural evolution in a new 770 MPa hot rolled Nb-Ti microalloyed steel. Materials Science and Engineering A. 2005;394(1-2):339-52.

6. Patel J, Klinkenberg C, Hulka K. Hot rolled HSLA strip steels for automotive and construction applications. International symposium, Niobium; Science & Technology; 2001: 647-674

7. Adamczyk J. Development of the microalloyed constructional steels. Journal of Achievements in Materials and Manufacturing Engineering. 2006;14(1-2):9-20.

8. Honeycombe RWK, Bhadeshia HKDH. Steels: Microstructure and Properties. second edition ed. Honeycombe PSR, Hancock PP, editors.: Edward Arnold; 1995.

9. Shirasawa H. Recent developments of cold formable high strength hot rolled steels in Japan. Symposium on High Strength Sheet Steels for the Automotive Industry, Baltimore; 1994, The Iron and Steel Society.

10. Chakrabarti D, Davis CL, Strangwood M. Development of bimodal grain structures in Nb- containing high strength low alloy steels during slab reheating. Metallurgical and Materials Transactions A. 2008;39A:1963-77.

11. Davis CL, Strangwood M. Segregation behaviour in Nb-microalloyed steels. Material Science and Engineering. 2009;25(9):1126-33.

12. Kundu A, Strangwood M, Davis CL. Grain structure development during reheating and deformation of niobium-microalloyed steels. Materials and Manufacturing Processes. 2010;25 (1-3):125-32.

13. Krauss G. Solidification, segregation and banding in carbon and alloy steels. Metallurgical and Materials Transactions B. 2003;34B:781-92.

14. Ghosh A. Segregation in cast products. Sadhana. 2001;26(n 1 & 2):5-24.

15. Priestner R, H LP, C Z, K IA. Microalloyed precipitation in HSLA steel austenite Microstructural Science. 1998;26:447-54.

16. Kundu A, Davis C, Strangwood M. Modelling of Grain Size Distributions during Single Hit Deforemation of a Nb-Containing Steel. Metallurgical and Materials Transactions A. 2010;41A(994-1002).

17. Hoogendoorm TM, Bodin A, Hekker PM. Accelerated cooling of strip: From coiling temperature control to heat treatment. Microalloying 95; 1995; Pittsburgh USA. Iron and steel society.

18. Cuddy LJ, Riley JC. Austenite Grain coarsening in microalloyed steels. Metallurgical and Materials Transactions A. 1983;14A:1989-95.

19. Muschenborn W, IMLAU K-P, Meyer L, Schriever U. Recent developments in Physical metallurgy and processing technology of microalloyed flat rolled steels. Microalloyed '95; 1995; Pittsburgh USA. Iron and Steel society; 1995. p. 35-48.

20. Sage AM. An overview of the use of Microalloys in HSLA Steels with particular reference to Vanadium and Titanium. Second International Conference on HSLA Steels; 1990; Beijing, China. The Minerals, Metals, and Materials Society.

21. Patel JK, Wilshire B. The challenge to produce consistent mechanical properties in Nb-HSLA strip steels. Journal of Materials Processing Technology. 2002;120 (1-3):316-21.

22. Tanaka T. Science and technology of hot rolling process of steel. Microalloying 95; 1995; Pittsburgh USA. Iron and steel society; 1995. p. 165-81.

23. Ssab rolling mills. [Internet] 2010 [cited 2010]: Available from: http://www.ssab.com /Global/Ssab/brochures/en/images_steelbok/rolling_mills_1.jpg.

24. Anderson TL. Fracture mechanics: fundamentals and applications. 2nd ed: CRC Press; 1994.

25. Palmiere EJ, Garcia CI, DeArdo AJ. Influence of niobium super saturation in austenite on the static recrystallization behaviour of low carbon microalloyed steels. Metallurgical and Materials Transactions A. 1996; 27A(4):951-60.

26. Kundu A. Grain Structure Development During Casting, Reheating and Deformation of Nb-Microalloyed Steel. Birmingham, PhD Thesis. The University of Birmingham; 2011.

27. le Bon A, Rofes-Vernis J, Rossard C. Recrystallization and precipitation during hot working of a Nb-Bearing HSLA steel. Metal Science. 1975;9((1)):36-40.

28. Dutta B, Sellers CM. Effect of composition and process variables on Nb(C,N) precipitation in niobium microalloyed austenite. Material Science and Technology. 1987;3 (3):197-206.

29. Everest R. Segregation and grain size development in high strength steel strip samples. Unpublished work; 2011.

30. Cuddy LJ. Effects of microalloy concentration on the recrystallization of austenite during hot deformation"; Conference on 'Thermomechanical processing of microalloyed

austenite. Thermomechanical Processing of Microalloyed Austenite; 1982; Warrendale, Pa, USA. Metallurgical Soc of AIME: 129-40.

31. Korchynsky M. Twenty years since microalloying '75. Microalloying '95; 1995; Pittsburgh USA. Iron and steel society; 1995:3-13.

32. Siwecki T. Recrystallisation controlled rolling of HSLA steels. Microalloying '95; 1995; Pittsburgh USA. Iron and steel society; 1995:197-211.

33. Yi H-l, Du L-x, Wang G-d, Liu X-h. Development of Nb-V-Ti Hot-Rolled High Strength Steel With Fine Ferrite and Precipitation Strengthening. Journal of Iron and Steel Research, International. 2009;16(4):72-7.

34. Sha Q-y, Li G-y, Qiao L-f, Yan P-y. Effect of Cooling Rate and Coiling Temperature on Precipitate in Ferrite of a Nb-V-Ti Microalloyed Strip Steel. Journal of Iron and Steel Research, International. 2007;14(5, Supplement 1):316-9.

35. Petch NJ. The influence of grain boundary carbide and grain size on the cleavage strength and impact transition temperature of steel. Acta Metallurgica. 1986;34(7):1387-93.

36. Petch NJ. The influence of some substitutional alloys on the cleavage of ferritic steels. Acta Metallurgica. 1987;35(8):2027-34.

37. Llewellyn DT, Steels: Metallurgy and Applications. second ed: Butterworth-Heinemann ; 1992.

38. Talbot D. The effects of plate processing parameters on the microstructure, mechanical properties and precipitation characteristics of niobium-containing high strength low alloy steels, Birmingham, PhD Thesis, The University of Birmingham; 2002.

39. Kostryzhev AG. Bauschinger Effect in Nb and V Microalloyed Line Pipe Steels. Birmingham; PhD Thesis, The University of Birmingham; 2009.

40. Bhattacharjee D, Davis CL, J F, Knott. Predictability of Charpy impact toughness in thermomechanically controlled (TMCR) microalloyed steels. Ironmaking and Steelmaking. 2003;30(1).

41. Bhattacharjee D, Davis CL. Influence of processing history on mesotexture and microstructure-toughness relationship in control-rolled and normalised steels. Scripta Materialia. 2002;47(12):825-31.

42. Irvine KJ. The development of high-strength steels. Iron and steel Institute. 1962;200:820-36.

43. Kuziak R, Kawalla R, Waengler S. Advanced high strength steels for automotive industry. Archives of Civil and Mechanical Engineering. 2008;8(2):103-17.

44. Kimura Y, Inoue T, Yin F, Tsuzaki K. Inverse Temperature Dependence of Toughness in an Ultrafine Grain-Structure Steel. Science. 2008;320(5879):1057-60.

45. Feng C, Fang H-s, Zheng Y-k, Bai B-z. Mn-Series Low-Carbon Air-Cooled Bainitic Steel Containing Niobium of 0.02%. Journal of Iron and Steel Research, International. 2010;17(4):53-8.

46. Bannister AC, Burns DY. Qualitative assessment of factors affecting Charpy impact properties in TMCR steels, unpublished work; 2002.

47. ASM Handbook. Properties and Selection: Irons, Steels, and High-Performance Alloys; 1, 1993.

48. Bhole SD, Nemade JB, Collins L, Liu C. Effect of nickel and molybdenum additions on weld metal toughness in a submerged arc welded HSLA line-pipe steel. Journal of Materials Processing Technology. 2006;173(1):92-100.

49. Linaza MA, Romero JL, Rodríguez-Ibabe JM, Urcola JJ. Influence of the microstructure on the fracture toughness and fracture mechanisms of forging steels

microalloyed with titanium with ferrite-pearlite structures. Scripta Metallurgica et Materialia. 1993;29(4):451-6.

50. Zhang L. Microstructure and Fracture Toughness in the HAZ of a Structural Steel Containing TiN particles, PhD Thesis, The University of Birmingham; 2000.

51. Narita K. Physical chemistry of the groups IVa (Ti, Zr), Va (V, Nb, Ta) and the rare earth elements in steel. Transactions of The Iron and Steel Institute of Japan. 1975;15 (3): 145-52.

52. Lin WJ, Jonas JJ. A stress relaxation method for the following carbonitride precipitation in austenite at hot working temperatures, Metallurgical and Materials Transactions A. 1988;19:1403-13.

53. Davis JR. Alloying: Understanding the basics. United States of America: ASM International; 2001.

54. Klassen RJ, Bassim MN, Bayoumi MR, Wilsdorf HGF. Characterization of the effect of alloying elements on the fracture toughness of high strength, low alloy steels. Materials Science and Engineering. 1986;80(1):25-35.

55. ASM Handbook. Metallography and Microstructures; 9; 2004.

56. Shanmugam P, Pathak SD. Some studies on the impact behaviour of banded microalloyed steel. Engineering Fracture Mechanics. 1996;53(6):991-1005.

57. Lin T, Evans AG, Richie RO. Stochastic Modelling of the Independent Roles of partical size and grain size in transgranular Cleavage Fracture. Metallurgical Transactions A. 1987;18A:641-51.

58. Mintz B, Morrison WB, Jones A. Influence of carbide thickness on impact transition temperature of ferritic steels. Metals technology. 1979;6:252-60.

59. Bhattacharjee D, Knott JF, Davis CL. Charpy-Impact-Toughness Prediction using an 'Effective' Grain Size for Thermomechanically Controlled Rolled Microalloyed Steels. Mettallurgical and Materials Transactions A. 2004;35A:121-30.

60. Echeverría A, Rodriguez-Ibabe JM. The role of grain size in brittle particle induced fracture of steels. Materials Science and Engineering A. 2003;346(1-2):149-58.

61. Curry DA, Knott JF. Effects of microstructure on cleavage fracture stress in steel. Metal Science. 1978;12:511-4.

62. Fairchild DP, Howden DG, Clark WAT. The Mechanism of Brittle Fracture in a Microalloyed Steel part 1: Inclusion- Induced Cleavage. Metallurgical and Materials Transactions A. 2000;31A:641- 51.

63. Linaza MA, Romero JL, Rodríguez-Ibabe JM, Urcola JJ. Cleavage fracture of microalloyed forging steels. Scripta Metallurgica et Materialia. 1995;32(3):395-400.

64. Du J, Strangwood M, Davis CL. Examination of the Effect of TiN Particles and Grain Size on the Charpy Impact Transition Temperature in Steels. Material Science and Technologies; 2012; 28; 10: 878-888

65. Yan W, Shan YY, Yang K. Effect of TiN inclusions on the impact toughness of low-carbon microalloyed steels. Metallurgical and Materials Transactions A. 2006;37A:2147-58.

66. Yan W, Shan YY, Yang K. Influence of TiN Inclusions on the Cleavage Fracture Behaviour of Low-Carbon Microalloyed Steels. Metallurgical and Materials Transactions A. 2007; 38:1211-22.

67. Zhang LP. Dependency of fracture toughness on the inhomogeneity of coarse TiN particle distribution in a low alloy steel. Metallurgical and Materials Transactions A. 2001;32A:1147-55.

68. Ju J-B, Lee J-S, Jang J-i. Fracture toughness anisotropy in a API steel line-pipe. Materials Letters. 2007;61(29):5178-80.

69. Hatherly M, Hutchinson WB. An Introduction to Textures in Metals, Monograph no 5; The Institute of Metallurgists; London; 1979.

70. Dieter GE, editor. Mechanical Metallurgy. UK: McGraw- Hill; 1988.

71. Yang M, Chao YJ, Li X, Immel D, Tan J. Splitting in dual-phase 590 high strength steel plates: Part II. Quantitative analysis and its effect on Charpy impact energy. Materials Science and Engineering: A. 2008;497(1-2):462-70.

72. Yan W, Sha W, Zhu L, Wang W, Shan Y-Y, Yang K. Delamination fracture related to tempering in a high strength low-alloy steel. Metallurgical and Materials Transactions A. 2010;41A:159-71.

73. Baldi G, Buzzichelli G. Critical stress for delamination fracture in HSLA steels. Metal Science. 1978;12(10):459-72.

74. Krishnadev MR, Dionne S, Morrisson J. Observation of splits on the surface of fracture toughness test specimens of HY-130 steel. Materials Characterization. 1990;24(2):169-78.

75. Mintz B, Maina E, Morrison WB. Origin of fissures on fracture surfaces of impact samples of HSLA steels with ferrite/ pearlite microstrucutures. Materials Science and Engineering. 2007;23(3):347- 54.

76. Mintz B, Morrison WB. Influence of fissures on tensile and fracture toughness of steels with ferrite/pearlite microstructures. Materials Science and Engineering. 2007;23(11).

77. Mintz B, Maina EM, Morrison WB. Influence of dislocation hardening, precipitation hardening, grain elongation and sulphides on fissure formation in HSLA steels having a ferrite/ pearlite microstructure. Institute of Materials, Minerals and Mining. 2008;24(2): 177-88.

78. Joo MS, Suh D-W, Bae JH, Bhadeshia HKDH. Role of delamination and crystallography on anisotropy of Charpy toughness in API-X80 steel. Material Science and Engineering A. 2012; 564; 314-322

79. Bramfitt BL, Marder AR. A Study of the Delamination Behavior of a Very Low-Carbon Steel. Metallurgical Transactions A. 1977;8a:1263.

80. Song R, Ponge D, Raabe D. Mechanical properties of an ultrafine grained C-Mn steel processed by warm deformation and annealing. Acta Materialia. 2005;53(18):4881-92.

81. World Steel Association M. Steel University 2002 [Internet]; 2002; [cited 2012 10/01]; Available from: http://steeluniversity.org/content/html/eng/default.asp?catid=1&pageid=2081271925.

82. Knott JF. Fundamentals of Fracture Mechanics. Bath, UK: The Butterworth Group; 1973.

83. Morrison WB. Influence of testing direction on the mechanical properties of wrought steel. Metals technology. 1975:33-45.

84. Bourell DL. Cleavage Delamination in impact tested warm-rolled steel. Metallurgical Transactions A. 1983;14A:2487-96.

85. Schofield R, Rowntree G, Sarma NV, Weiner RT. 'Arrowhead' fractures in controlled-rolled pipeline steels. Metals Technology. 1974:325-31.

86. Towers OL. Testing of sub size Charpy specimens Part 1- the influence of thickness on the ductile/ brittle transition. Metal Construction. 1986;18(3):171R-6R.

87. Wallin K, Planman T, Valo M, Francois D, Pineau A. Fracture mechanics based scaling criteria for miniature and sub-size Charpy-V specimens. European Structural Integrity Society: Elsevier; 2002. p. 279-86.

88. Bannister AC. Sub task 3.3 report: Final issue determination of fracture toughness from Charpy impact energy: procedure and validation. Rotherham: British Steel; Unpublished work; 1998.

89. BS 7910:2005. Guidance on methods for assessing the acceptability of flaws in metallic structures; 2005.

90. Embury JD, N.J. Petch, A.E. Wraith and E.S. Wright, Fracture behaviour of mild steel laminates; Transactions of the American Institute of Mining, Metallurgical and Petroleum Engineers; 1967; 239: 144-118.

91. Wallin K. Upper shelf energy normalisation for sub-sized Charpy-V specimens. International Journal of Pressure Vessels and Piping. 2001;78(7):463-70.

92. Curry DA. Cleavage micromechanisms of crack extension in steels; Metal Science; 1980; 14:319-26.

93. Mintz B, Morrison WB. Influence of warm working and tempering on fissure formation; Material Science and Technology. 1988;4:719-31.

94. Morrison J, Wu X. The toughness transition curve of a ship steel. European Structural Integrity Society: Elsevier; 2002. p. 385-92.

95. Ferguson BL, editor. The relationship between splitting phenomena and sample thickness in Charpy V-notch impact testing. What does the Charpy test really tell us; 1978.

96. Oldfleld W. Fitting curves to toughness data. Journal of Testing and Evaluation, JTEVA. Nov 1979; 6: 326-333.

97. Kostryzhev AG, Punch RB, Davis CL, Strangwood M. Acoustic Emission monitoring of split formation during Charpy impact testing of high strength steel. Material Science and Technology. 2012;28(2):240-2.

98. Baczynski GJ, Jonas JJ, Collins LE. The influence of rolling practice on notch toughness and texture development in high-strength line pipe; Metallurgical and Materials Transactions A. 1999; 30A:3045-54.